CONTRIBUTION FOR THE EXPLOITATION OF COHERENT AND INCOHERENT NONLINEAR PHENOMENA IN TELECOMMUNICATION

A Thesis
Presented to
The Academic Faculty

by

CHEMBO KOUOMOU Yanne

In Fulfillment
of the Requirements for the
Doctorat/PhD degree of Physics
Under the supervision of
Prof. WOAFO Paul

Laboratory of Mechanics, Department of Physics
Faculty of Science, University of Yaoundé I
November 2005

LIST OF THE PERMANENT TEACHING STAFF OF THE FACULTY OF SCIENCE, UNIVERSITY OF YAOUNDE I

Dean : Prof. Thomas NJINE
Vice-Dean (Scolarity) : Prof. Monique ESSONO
Vice-Dean (Academic Affairs) : Prof. Raphaël GHOGOMU
Vice-Dean (Research and Cooperation) : Prof. Laure Pauline FOTSO

1 - DEPARTMENT OF BIOCHEMISTRY (BC)			
N°	**Names and surnames**	**Grade**	**Observations**
1	ETOA François Xavier	Associate Professor	**Head of Dept.**
2	ATOGHO Barbara	Senior Lecturer	on duty
3	FOKOU Elie	Senior Lecturer	on duty
4	BENG born NINTCHOM P. V.	Senior Lecturer	on duty
5	BIYITI BI ESSAM born AKAM ADA L. F.	Senior Lecturer	*Chef of div. at MINHED*
6	DEMMANO Gustave	Senior Lecturer	on duty
7	DJOKAM Rosine Rachel	Senior Lecturer	on duty
8	ESSIA NGANG Jean Justin	Senior Lecturer	on duty
9	EVEHE BEBANDOUE M.-S.	Senior Lecturer	on duty
10	FEKAM BOYOM Fabrice	Senior Lecturer	*Fulbright grant*
11	KANSCI Germain	Senior Lecturer	on duty
12	MBACHAM Wilfred	Senior Lecturer	on duty
13	MINKA Samuel	Senior Lecturer	on duty
14	MOFOR born TEUGWA C.	Senior Lecturer	on duty
15	MOUNDIPA FEWOU Paul	Senior Lecturer	on duty
16	MULUH John PAYNE	Senior Lecturer	on duty
17	NGUEFACK Julienne	Senior Lecturer	on duty
18	KENFOU NGUEFEU Céline	Senior Lecturer	on duty
19	NJAYOU MOUNDJOHOU	Senior Lecturer	absent from post
20	OBEN Julius ENYONG	Senior Lecturer	on duty

21	RIWOM SARA Honorine	Senior Lecturer	on duty
22	TCHANA NKOUATCHOUA A.	Senior Lecturer	on duty
23	WAKAM born NANA Louise	Senior Lecturer	on duty
24	BELINGA born NDOYE FOE	Assistant	on duty
25	EWOANE Célestin	Assistant	absent from post
26	SHANG Judith DZELAMBONG	Assistant	on duty
27	SOUOPGUI Jacob	Assistant	on duty
2 - DEPARTMENT OF ANIMAL BIOL. AND PHYSIOL. (B.P.A.)			
28	NJIKAM NJIFUTIE	Associate Professor	**Head of Dept.**
29	NJINE Thomas	Professor	**Dean**
30	BILONG BILONG Charle F.	Associate Professor	on duty
31	FOMENA Abraham	Associate Professor	on duty
32	KAMTCHOUING Pierre	Associate Professor	on duty
33	MESSI Jean	Associate Professor	on duty
34	MONKIEDJE Adolphe	Associate Professor	on duty
35	NGASSAM Pierre	Associate Professor	on duty
36	TCHUEM TCHUENTE L.	Associate Professor	on duty
37	BAPFUBUSA Bénoît Alain	Senior Lecturer	on duty
38	CHUNGANG born NKEH B.	Senior Lecturer	on duty
39	DIMO Théophile	Senior Lecturer	on duty
40	DJIETO Lordon Champlain	Senior Lecturer	on duty
41	ENO Anna Aret	Senior Lecturer	on duty
42	ESSOMBA born NTSAMA M.	Senior Lecturer	on duty
43	FOTO MENBOHAN Samuel	Senior Lecturer	on duty
44	KAMGANG René	Senior Lecturer	on duty
45	NJAMEN Dieudonné	Senior Lecturer	on duty
46	NJIOKOU Flobert	Senior Lecturer	on duty
47	NOLA Moïse	Senior Lecturer	on duty
48	RAKOTONIRINA Vincent S.	Senior Lecturer	on duty
49	BELLET EDIMO Oscar R.	Assistant	on duty
50	MBOUDJEKA Innocent	Assistant	absent from post
3 - DEPARTMENT OF PLANT BIOL. AND PHYSIOL. (B.P.V.)			
51	AMOUGOU AKOA	Professor	**Head of Dept.**
52	NKONGMENECK Bernard A.	Associate Professor	on duty

53	AHANDA b. MBOLO M.	Senior Lecturer	on duty
54	AMBANG Zachée	Senior Lecturer	on duty
55	ATANGANA ETEME R.	Senior Lecturer	on duty
56	BELL Joseph Martin	Senior Lecturer	*ch. serv. Socopalm*
57	BONGEN OTTOKO B.	Senior Lecturer	*Chef. Serv. Fac. Sc.*
58	BOYOMO ONANA	Senior Lecturer	on duty
59	KENLA Jean Victor	Senior Lecturer	on duty
60	DJOCGOUE Pierre F.	Senior Lecturer	on duty
61	NGABA ZOGO Félix	Senior Lecturer	*Insp. at MINREST*
62	NWAGA Dieudonné M.	Senior Lecturer	on duty
63	YOUMBI Emmanuel	Senior Lecturer	on duty
64	ZAPFACK Louis	Senior Lecturer	on duty
65	MOSSEBO Dominique C.	Senior Lecturer	on duty
66	NGOUO Lucas Vincent	Senior Lecturer	on duty
67	TSOATA Esaïe	Senior Lecturer	on duty
68	ABOMO NDONGO S.	Assistant	absent from post
69	BIYE Elvire H.	Assistant	on duty
70	MBARGA BINDZI M. A.	Assistant	on duty
71	NGALLE Hermine BILLE	Assistant	on duty
4 - DEPARTMENT OF INORGANIC CHEMISTRY (C.I.)			
72	NJOPWOUO Daniel	Professor	**Head of Dept.**
73	NEMBA Robert	Professor	*C.E. in MINREST*
74	NOAH NGAMVENG J.	Professor	on duty
75	GHOGOMU Paul MINGO	Professor	on duty
76	NDIFON Peter TEKE	Associate Professor	on duty
77	NGAMENI Emmanuel	Associate Professor	on duty
78	YOUNANG Elie	Associate Professor	on duty
79	AGWARA ONDOH	Senior Lecturer	In mission to USA
80	AVOM Jérôme	Senior Lecturer	Ch. Div. UYI
81	BABALE born DJAM D.	Senior Lecturer	*In Char. of Mis. P.R.*
82	BAIZOUMI ZOUA	Senior Lecturer	*Ch. Serv. MINTOUR*
83	DJOUFAC WOUMFO E.	Senior Lecturer	on duty
84	DOUBLA AVALY	Senior Lecturer	*Nat. Sec. Islm. Educ.*
85	ELIMBI Antoine	Senior Lecturer	on duty

86	GWET Simon-Pierre	Senior Lecturer	on duty
87	KAMWA Jean Dagobert	Senior Lecturer	on duty
88	KETCHA MBADCAM J.	Senior Lecturer	on duty
89	KONG SAKEO	Senior Lecturer	*C.M. of P.M.*
90	LAMINSI Samuel	Senior Lecturer	on duty
91	LIBOUM	Senior Lecturer	on duty
92	MELO born CHINJE U. F.	Senior Lecturer	*Dir. at MINREST*
93	MOULIOM Christophe	Senior Lecturer	on duty
94	NANSEU Charles Péguy	Senior Lecturer	on duty
95	NDIKONTAR Maurice KOR	Senior Lecturer	on duty
96	NENWA Justin	Senior Lecturer	on duty
97	NGOMO Horace MANGA	Senior Lecturer	*C.T. of P.M.*
98	PAYOM Gaston	Senior Lecturer	on duty
99	SIGNING Pierre	Senior Lecturer	on duty
5 - DEPARTMENT OF ORGANIC CHEMISTRY (CO)			
100	SONDENGAM B. Lucas	Professor	**Head of Dept.**
101	FOMUM TANEE Zacharias	Professor	on duty
102	FON KIMBU Samuel	Professor	on duty
103	GHOGOMU TIH Raphäel	Professor	**Vice-Dean**
104	NGADJUI TCHALEU B.	Professor	on duty
105	LONTSI David	Professor	on duty
106	NKENFACK Augustin E.	Professor	on duty
107	NYASSE Barthélémy	Professor	on duty
108	TSAMO Etienne	Professor	on duty
109	DONGO Etienne	Associate Professor	on duty
110	KAPNANG Henriette	Associate Professor	on duty
111	MBAFOR Joseph	Associate Professor	on duty
112	WANDJI Jean	Associate Professor	on duty
113	Alex de Théodore ATCHADE	Senior lecturer	on duty
114	FOLEFOC G. NGOSONG	Senior Lecturer	on duty
115	KEUMEDJIO Félix	Senior Lecturer	on duty
116	KOUAM Jacques	Senior Lecturer	on duty
117	MBAZOA born DJAMA C.	Senior Lecturer	on duty
118	MESSANGA Bernard B.	Senior Lecturer	on duty
119	MOFO born NGOUNOU F.	Senior Lecturer	on duty

120	NGOUELA Silvère A.	Senior Lecturer	on duty
121	NOUNGOUE TCHAMO D.	Senior Lecturer	on duty
122	NTEDE NGA Hypolite	Senior Lecturer	on duty
123	NYEMBA b. ETOUNOU	Senior Lecturer	on duty
124	PEGNYEMB Dieudonné E.	Senior Lecturer	on duty
125	TCHOUANKEU J.-C.	Senior Lecturer	on duty
126	TIH b. NGO BILONG E.	Senior Lecturer	on duty
127	YANKEP Emmanuel	Senior Lecturer	on duty
6 - DEPARTMENT OF COMPUTER SCIENCE (IN)			
128	KAMGNIA Emmanuel	Senior Lecturer	**Head of Dept**
129	TCHUENTE Maurice	Professor	on duty
130	FOTSO Pauline L.	Associate Professor	*Vice-Dean*
131	BOYOM SOP Flaubert	Senior Lecturer	on duty
132	FOUDA NDODO Marcel	Senior Lecturer	*Ch. S. MINHED*
133	KAMDOUM Basile	Senior Lecturer	on duty
134	LOUKA Basile	Senior Lecturer	on duty
135	NDOUNDAM René	Senior Lecturer	on duty
136	NZALI Jean-Pierre	Senior Lecturer	on duty
137	TINDO Gilbert	Senior Lecturer	on duty
138	ATSA ETOUNDI Roger	Assistant	on duty
139	TAPOMO	Assistant	on duty
7 - LANGUAGE LABORATORY (LA)			
8 - DEPARTMENT OF MATHEMATICS (MA)			
140	BEKOLLE David	Professor	**Head of Dept.**
141	NOUTCHEGUEME Norbert	Professor	on duty
142	DOSSA COSSY Marcel	Associate Professor	on duty
143	NGUETSENG Gabriel	Associate Professor	*Head of C.C.*
144	NJOCK Georges Edward	Associate Professor	on duty
145	TAYOU SIMO	Associate Professor	on duty
146	WAMON François	Associate Professor	on duty
147	WOUAFO KAMGA Jean	Associate Professor	on duty
148	BATE EYA Hans MBI	Senior Lecturer	on duty
149	BINZOULI Etienne J.-J.	Senior Lecturer	on duty
150	EMVUDU WONO Yves S.	Senior Lecturer	*Ch. Sev. MINHED*
151	FOMEKONG Christophe	Senior Lecturer	on duty

152	KIKI Maxime A.	Senior Lecturer	on duty
153	MBAKOP Guy Merlin	Senior Lecturer	on duty
154	MBIANDA Gilbert	Senior Lecturer	on duty
155	MEWOLI Boulchard	Senior Lecturer	*Ch. Div. MINHED*
156	NDAKBO Victor	Senior Lecturer	on duty
157	NGUIMTSA Charles	Senior Lecturer	on duty
158	NKUIMI JUGNIA Célestin	Senior Lecturer	on duty
159	NOUNDJEU Pierre	Senior Lecturer	on duty
160	TCHANGANG Roger D.	Senior Lecturer	on duty
161	TCHAPNDA NJABO S. B.	Senior Lecturer	on duty
162	TIAYA TSAGUE N. A.-M.	Senior Lecturer	on duty
163	TONGA Marcel	Senior Lecturer	on duty
164	ZAME Alfred	Senior Lecturer	*Ch. Sev. MINCOM*
165	TAN AHANDA Barnabé	Assistant	*Ch. Sev. MINCOM*
166	TSEBO Alexis	Assistant	on duty
9 - DEPARTMENT OF PHYSICS (PH)			
167	MANGUELLE-DICOUM E.	Associate Professor	**Head of Dept.**
168	DOMNGANG Samuel	Professor	on duty
169	KOFANE Timoléon Crépin	Professor	*Ch. Div. UYI*
170	WOAFO Paul	Professor	on duty
171	MKANKAM KAMGA F.	Associate Professor	on duty
172	NJOMO Donatien	Associate Professor	on duty
173	OWONO ATEBA	Associate Professor	on duty
174	EKOBENA FOUDA H. P.	Senior Lecturer	on duty
175	ESSIMBI ZOBO Bernard	Senior Lecturer	on duty
176	KWENDE MBANWI Teddy	Senior Lecturer	on duty
177	MAGA Emire Mondésir	Senior Lecturer	on duty
178	MBANE BIOUELE	Senior Lecturer	on duty
179	MBONO SAMBA Yves C.	Senior Lecturer	on duty
180	MOUSSA Ildoko	Senior Lecturer	*S. Dir. MINUH*
181	NDJAKA Jean Marie B.	Senior Lecturer	on duty
182	NDOP Joseph	Senior Lecturer	on duty
183	NOUAYOU Robert	Senior Lecturer	on duty
184	PEMHA Elkana	Senior Lecturer	on duty
185	TABOD Charles TABOD	Senior Lecturer	on duty

186	TCHAWOUA Clément	Senior Lecturer	on duty
187	TCHOFFO Fidèle	Senior Lecturer	on duty
188	ZEKENG Serge Sylvain	Senior Lecturer	on duty
189	BEN-BOLIE Germain	Assistant	on duty
190	BIYA MOTTO Frédéric	Assistant	*Ch. S. UYI*
191	OBOUNOU Marcel	Assistant	on duty
10 - DEPARTMENT OF EARTH SCIENCE (ST)			
192	NDJENG Emmanuel	Associate Professor	**Head of Dept.**
193	EKODECK Georges	Professor	*V. Chancellor UD*
194	NZENTI Jean-Paul	Associate Professor	on duty
195	ABOSSOLO b. ANGUE	Senior Lecturer	on duty
196	BEKOA Etienne	Senior Lecturer	on duty
197	BITOM Dieudonné	Senior Lecturer	on duty
198	BONDJE Charles	Senior Lecturer	on duty
199	DJEUDA TCHAPNGA	Senior Lecturer	on duty
200	GHOGOMU R. TANWI	Senior Lecturer	on duty
201	KAMGANG Pierre	Senior Lecturer	on duty
202	LAMILEN BILLA D.	Senior Lecturer	on duty
203	MINYEM Dieudonné	Senior Lecturer	on duty
204	MOUAFO Lucas	Senior Lecturer	on duty
205	MOUNDI Amidou	Senior Lecturer	*Ch. Serv. UYI*
206	MVONDO ONDOA J.	Senior Lecturer	*Ch. Serv. MINTOWN*
207	NDAM NGOUPAYOU	Senior Lecturer	on duty
208	NDJIGUI Paul-Désiré	Senior Lecturer	on duty
209	NGONGE Emmanuel D.	Senior Lecturer	on duty
210	NGOS III Simon	Senior Lecturer	on duty
211	NJILAH Isaac KONFOR	Senior Lecturer	on duty
212	NJOM Bernard D.	Senior Lecturer	on duty
213	NKONGUIN BSIFA E.	Senior Lecturer	on duty
214	NKOUMBOU Charles	Senior Lecturer	on duty
215	NYECK Bruno	Senior Lecturer	on duty
216	TCHOUANKOUE J.-P.	Senior Lecturer	on duty
217	TEMDJIM Robert	Senior Lecturer	on duty
218	YENE ATANGANA J. Q.	Senior Lecturer	on duty

219	YONGUE born FOUATEU Rose	Senior Lecturer	on duty
220	BISSO Dieudonné	Assistant	on duty
221	ESSONO Jean	Assistant	on duty
222	NGO BIDJECK Louise Marie	Assistant	on duty
223	TCHAKOUNTE Jacqueline	Assistant	on duty
224	ZO'O ZAME Philémon	Assistant	on duty

SHARING OF LECTURERS IN THE FACULTY OF SCIENCE ACCORDING TO DEPARTMENTS + 1 LANGUAGE SERVICE

DEPARTMENT	**NUMBER OF LECTURERS**				
	Prof.	Ass. Prof.	Sen. Lect.	Asst.	Total
BC	0	1	22 (10)	4 (3)	27 (13)
B.P.A.	1	8	12 (3)	2 (1)	27 (4)
B.P.V.	1	1	15 (1)	4 (3)	21 (4)
C.I.	3	4	21 (2)	0	28 (2)
C.O.	9	4(1)	15 (4)	0	28 (5)
IN	1	1(1)	8	2	12 (1)
MA	2	6	17 (1)	2	27 (1)
PH	3	4	14 (1)	4	25 (1)
ST	1	2	25 (2)	5 (2)	33 (4)
LA					
Total	**21**	**31 (2)**	**149 (24)**	**23 (9)**	**224 (35)**

Total:

- Professors **21**
- Associate Professors **31** of which **1** non Cameroonian
- Senior Lecturers **149** of which **3** non Cameroonian and **1** absent from post
- Assistants **23** of which **1** non Cameroonian and **3** absent from post

( ) = Number of women

"Water no get enemy"

To the Past
and for the Future
of the Ancestry

ACKNOWLEDGEMENTS

IT is generally considered that a PhD thesis is the conventional terminus of academic studies. Some people even told me that it is the opportunity to climb up onto all that I have learned to contribute to the advancement of Knowledge (modestly, of course).

I have the weakness to believe them.

Beyond any doubt, the person that helped me the most to climb up this famous Tree of Knowledge is Prof. Paul Woafo, from the University of Yaoundé I, Cameroon. It is notorious that the upper branches in a tree (corresponding to research in the Tree of Knowledge) are always the most tricky and the most dangerous to manage. But at any time, I knew I could always rely on the solid hands and far-seeing eyes of "the Prof.". Thank you so much for all these years of learning, all these years of advises, and all these years of collaboration.

I am also grateful to Prof. Timoléon Kofané, Head of the Laboratory of Mechanics, for the pluri-disciplinary spirit and high-quality standards he has patiently imposed in the group during the last 15 years.

I wish to express my aknowledgements to the distinguished members of the Scientific Community who have accepted to discuss and appreciate the results of this thesis during its refereeing and its defense.

I would like to thank sincerely all those who have dedicated even a single second of their time to teach me a part of what they knew, from the primary school to the University, with a particular emphasis on the teaching staff of the Department of Physics, University of Yaoundé I : without all that you taught me (these solid branches at the base of the Tree of Knowledge), none of this would have been possible.

I extend my thanks to all my solitono-chaotic team mates of the Laboratory of Mechanics for the excellent atmosphere of friendship and collaboration that was sustained during these recent years. Tins, Debah, Coach, Sammy, Blaise, Rv, ϕ^6, and all my fellow co-workers: thank you.

All my friends worldwide (Keintosh *et al.* : the list is bijective to $\mathbf{N}$), may we one day gather and drink some palm wine. Thanks to all.

I am very grateful to Dr. Pere Colet, to Dr. Claudio Mirasso and to Prof. Maxi San Miguel of the *Mediterranean Institute for Advanced Studies* (Palma de Mallorca, Spain), for giving me the opportunity to work with them and learn more by their side.

I would also like to thank the *Edward Bouchet - Abdus Salam Institute*, the *Abdus Salam International Center for Theoretical Physics* of Trieste in Italy, and the *Ministry of Higher Education* of the Republic of Cameroon, for the financial support they have provided for the completion of this thesis.

In general, I express my warmest thanks to all those who have anyhow tried to open (close) me some doors in the way: you deserve all my gratitude for having willingly (unwillingly) contributed to convert me into a better physicist, and into a better man.

And I end with those who are by far the most important persons in my life: my mother (I am so proud to be your son), my father, my brother (Redig), my sisters (Simo, San and Na), my nephews (Laëtis, Edson and Ayougeth), my Venerable Ancestors beyond, and the One above. What I have to say is quite simple: without you, I am nothing.

TABLE OF CONTENTS

LIST OF TABLES

LIST OF FIGURES

LIST OF ACRONYMS

CMO	Chaos MOdulation
CMOS	Complementary Metal-Oxide Semiconductor
CMSL	Current-Modulated Semiconductor Laser
CSK	Chaos Shift-Keying
DDE	Delay Differential Equation
ECSL	External-Cavity Semiconductor Laser
GCS	Generalized Correlated State
HB	Hopf Bifurcation
ODE	Ordinary Differential Equation
UPO	Unstable Periodic Orbit
SCS	Standard Correlated State
SDE	Stochastic Differential Equation
SWDO	Single-Well Duffing Oscillator

ABSTRACT

The purpose of this thesis is to study the phenomena of synchronization and pattern formation in lattices of chaotic oscillators in view of applications to cryptography and switching in telecommunications.

This work is divided in four chapters.

In the first chapter, we perform the optimization and stability analysis for the synchronization of coupled chaotic oscillators. We use the Floquet theory to determine optimal synchronization conditions for coupled system. We also study the neighboring cases of delayed synchronization and external feedback control.

In the second chapter, the study is extended to the problem of pattern formation in one-dimensional lattices of diffusely coupled chaotic oscillators. We first focus on the case of a low dimensional ring, and then generalize the obtained results to lattices of arbitrary size.

Chapter III focuses on the dynamics and synchronization of chaotic semiconductor lasers. The two cases of current-modulated and external-cavity semiconductor lasers are considered, and the stability of their related synchronization manifolds is investigated. In both cases, the issue of parameter mismatch is also addressed.

The last chapter is devoted to the application of the observed coherent and incoherent nonlinear phenomena to cryptography and switching in optical-fiber telecommunication networks. We first ensure the secure encryption of digital messages with hyperchaotic carriers, and we secondly exploit the phenomenon of cluster synchronization in topologically shift-invariant lattices of chaotic semiconductor lasers to perform the switching in these chaos-secured networks.

RESUME

L'objet de cette thèse est d'étudier les phénomènes de synchronisation et de formation de structures dans les réseaux d'oscillateurs chaotiques, en vue de les appliquer à la cryptographie et à la commutation en télécommunications.

Ce travail est divisé en quatre chapitres.

Dans le premier chapitre, nous effectuons l'optimisation et l'étude de stabilité de la synchronisation d'oscillateurs chaotiques couplés. Nous utilisons la théorie de Floquet pour déterminer les conditions de synchronisation optimales pour le système couplé. Nous étudions aussi les cas voisins de la synchronisation retardée et du contrôle par rétro-alimentation externe.

Dans le second chapitre, l'étude est étendue au problème de la formation de structures dans les réseaux unidimensionnels d'oscillateurs chaotiques couplés diffusivement. Nous nous concentrons d'abord sur le cas d'un anneau de basse dimension, et ensuite nous généralisons les résultats obtenus à des anneaux de longueur arbitraire.

Le chapitre III se concentre sur la dynamique et la synchronisation de lasers à semiconducteurs chaotiques. Le cas des lasers à semiconducteurs modulés en courant et celui des lasers à semiconducteurs à cavité externe sont considérés, et la stabilité de leurs variétés de synchronisation est étudiée. Dans les deux cas, le problème de la desyntonie en paramètres est analysé.

Le dernier chapitre aura pour point focal l'application des phénomènes cohérents et incohérents observés à la cryptographie et à la commutation dans les réseaux de fibre optique en télécommunications. Nous réalisons dans un premier temps le cryptage de signaux digitaux avec des porteuses hyperchaotiques, et ensuite, pour assurer la commutation dans ces réseaux sécurisés grâce au chaos, nous exploitons le phénomène de synchronisation par blocs dans les systèmes de lasers à semiconducteur chaotiques couplés de manière topologiquement invariante par rotation.

GENERAL INTRODUCTION

AT the golden age of classical mechanics, determinism and predictability were assumed to be almost equivalent concepts. In a very famous citation [1], Laplace did enthusiastically express the tight relationship between both, emphasizing that determinism and predictability should be perfectly equivalent if one could afford an unlimited computing and analysis ability. However, in the early years of the twentieth century, Henri Poincaré did gather a convincing set of elements indicating that determinism and predictability do carry intrinsically different physical meanings, since the interplay between sensitivity to initial conditions and nonlinearity could lead to the emergence of a complex and apparently random dynamics [2]. Owing to the eclosion of digital computers and monitor graphics, Poincaré's intuition was confirmed sixty years later in a seminal article written by the meteorologist Edward Lorenz [3]: for the first time, a deterministic and unpredictable system was unambiguously identified. Since then, an ever growing interest has been devoted to investigate the nature and universality of this phenomenon, which has meanwhile received the name of **chaos**.

The very essence of chaos is complexity, unpredictability and sensitivity to initial conditions. Its ubiquity has yet been confirmed in various scientific fields ranging from biology to chemistry, passing through almost all the branches of physics and engineering [4, 5, 6, 7, 8]. During two decades, huge analytical, numerical and experimental efforts have sharpened our knowledge of chaos, from bifurcation scenarii to measures, characterization and routes to chaos. But today, beyond the identification and the study of isolated chaotic systems, investigation in chaos theory does particularly focus on the collective dynamics of coupled chaotic oscillators on one hand, and on innovative technological applications on the other.

It was thought for a long time that the natural extension of chaos in spatially coupled chaotic systems is **spatiotemporal chaos**, that is, a state of simultaneous chaos in the spatial and temporal domains. However, phenomena of self-organization and spatial coherence have effectively been observed in coupled chaotic oscillators, and have triggered off a tremendous interest for the study of their spatiotemporal dynamics. Applications rapidly appeared to be wide: pattern formation modeling,

coherent collective behavior in nonlinear physical, biological and ecological systems, oscillatory chemical processes, extended neuronal networks, etc.

For a number of oscillators restricted to two, emphasis is commonly laid upon the state of **synchronization**, which occurs when the two identical oscillators continuously remain in step with each other [9, 10, 11]. Several coupling schemes have been set up to achieve that purpose. Generally, in the synchronization mechanism, a "master" system drives or commands the dynamics of a "slave" system, even though other techniques with mutual coupling which ignore this hierarchy have been developed. The study of this counter-intuitive behavior of spatial coherence and temporal incoherence has turned into one of the leading topics of nonlinear dynamics, and very soon, several key-issues had emerged: the reduction of the undesirable effects of noise and parameter mismatch [12, 13], the minimization of both the synchronization time and the threshold energy input required for the process [14]. All these performance constraints can be resumed in one word: *optimization*. Theoretical analysis has shown that synchronization is generally optimized when the synchronization manifold is in the most stable configuration in the state space of the coupled system. **Consequently, one can in first approximation identify optimization to a maximal stability criterion, and the development of a general analytic approach able to define the coupling parameters leading to high-quality synchronization is still a wide-open problem**.

When the number of oscillators is increased, the dynamics of the whole coupled system becomes much more complex. Beside the well-known and intensively studied phenomena of spatiotemporal chaos [15] and complete (full) synchronization [16, 17], recent literature has reported the existence of hybrid configurations consequent to symmetry breaking and spontaneous spatial reordering, which are sometimes referred to as **cluster synchronization** [18, 19, 20, 21]. These intermediary states allow the chaotic oscillators to synchronize with one another in groups, while there is no synchronization among the groups. Clustering is mostly witnessed when the coupling is non-local [20] or non-symmetric [18]. It consequently appears as more fascinating and more unconventional when it occurs in a system with local and symmetric coupling [19, 21]. Depending on the number of chaotic oscillators, the type of coupling and the boundary conditions, the dynamical system can display a rich but limited set of different cluster patterns. In general, the stability of the various clusters is studied through the variations of the sub-Lyapunov exponents associated to their related sub-manifolds. Unfortunately, this numerical procedure is very time-consuming and moreover very repetitive, since the numerical simulation of the sub-Lyapunov

exponents has to be performed separately for each possible cluster. Therefore, this approach can no longer be applied when the number of oscillators becomes prohibitively high, as it is typically the case in the thermodynamic limit for the phase transitions theory of one-dimensional lattices. **There is consequently a necessity for a synthetic theory which would give an analytic insight into the various transitions that can occur between the possible dynamical states of the coupled system when the coupling strength or the number of oscillators is varied. Such a theory should ideally interpret within the same framework the underlying structure of both the states themselves and the various transitions between them**.

As far as technological applications are concerned, chaos has succeeded progressively in imposing itself as an interesting alternative solution for certain classes of problems. In laser science, a first decisive breakthrough was achieved in 1975 when Haken demonstrated that the dynamics of resonant single-mode ring-lasers is ruled by a Lorenz-like set of ordinary differential equations, and therefore can display a chaotic behavior [22]. Later, chaos will be identified in almost all types of lasers, such as fiber, solid-state or gas lasers. However, it has very soon been clearly assumed that technological applications are significantly more promising with semiconductor lasers, as their microchip structure, suitable wavelength and good efficiency at room temperature allow their use in the flourishing and strategic fiber telecommunications industry. The first important achievement in this domain was made in 1980 by Lang and Kobayashi, when they derived a set of delay differential equations to model the dynamics of single-mode semiconductor lasers subjected to external optical feedback [23]. It will further be demonstrated that beside the instability and hysteresis phenomena predicted in their article, the infinite dimensionality induced by the delay could give rise to an hyperchaotic dynamics [24].

Since then, the topic of chaos in semiconductor lasers has been intensively investigated. Today, several techniques are commonly used to induce chaos in semiconductor lasers, even though they can be gathered into two principal groups, namely parameter modulation [25, 26] and external feedback [27, 28, 29, 30, 31, 32, 33]. Following the mainstream trend of research in chaos theory, great attention has been paid to the collective dynamics of coupled semiconductor lasers in their chaotic regime. **Along that line, the synchronization of such chaotic lasers became a focus of strong interest, and currently, the determination of the necessary and/or sufficient conditions for their synchronization is still a difficult challenge,**

which has turned to be crucial when chaotic semiconductor lasers became potentially eligible for cryptography [34, 35].

Optical chaos cryptography is by far the most important application of laser chaos [36]. Nowadays, security in optical-fiber network is ensured by public key cryptosystems, which are softwares whose guarantee of security is computational complexity. Even though the level of security is constantly kept high by increasing the key-length (today, up to 512 bits), brute-force attacks or clever algorithmics may still be able to decipher the encrypted information. It has therefore been suggested that laser chaos could strengthen security through a complementary hardware encryption. More precisely, optical chaos cryptography relies on the synchronization of two semiconductor lasers operating in the chaotic regime. Typically, an information-bearing signal is encrypted within the noise-like output of a chaotic emitter, while a synchronous receiver recognizes the chaotic component and extracts it to reveal the originally encrypted signal. Within that framework, it can therefore be said that encryption relies on the unpredictability of chaotic oscillations, while decryption relies on their determinism. **In this context, the use of chaos cryptography will automatically impose important changes in the network architecture: effectively, hardware encryption is preferably compatible with hardware switching, as well as software encryption does fit with software switching**.

The main purpose of our work is to propose some solutions to the open points reported above, that is, to contribute to the exploitation of chaos synchronization and pattern formation for cryptography and switching applications in telecommunications. For that purpose, we will first study some fundamental aspects of synchronization and pattern formation in lattices of coupled chaotic oscillators. We further focus on the synchronization of chaotic semiconductor lasers, and on the related technological applications.

The thesis is therefore divided into four chapters.

In chapter I, we perform the optimization and stability analysis for the synchronization of unidirectionally coupled chaotic oscillators. We propose a new technique which enables a geometric interpretation of the dynamical states of the coupled system, as well as of the various bifurcations that may occur as the coupling parameter is varied. We also generalize the results to the neighboring cases of delayed synchronization and external feedback control.

Chapter II is entirely devoted to the problem of pattern formation in rings of diffusely coupled chaotic oscillators. We first focus on the case of a low dimensional

ring, for which the case of an external local injection is also analyzed. The results are generalized to a lattice of arbitrary dimension, and a scaling-law technique is used to study the dynamics of the system in the thermodynamic limit.

The dynamics and synchronization of chaotic semiconductor lasers is investigated in chapter III. We first consider the case where chaos is induced by ultra-high frequency pumping-current modulation, and secondly the case where an hyperchaotic dynamics results from external optical feedback. In both cases, the stability of the synchronization manifold is analytically investigated, and the detrimental influence of parameter mismatch on the quality of the synchronization is analyzed.

In chapter IV, the results obtained in the first three chapters are applied to cryptography and switching in optical-fiber telecommunication networks. On the one hand, we carry out the encryption of digital messages in hyperchaotic carriers, and on the other, we exploit the phenomenon of cluster synchronization in shift-invariant lattices of chaotic semiconductor lasers to perform the switching in chaos-secured networks.

We end with a general conclusion where the principal results of the thesis are summarized, and where perspectives for future investigation are sketched.

CHAPTER I

OPTIMIZATION AND STABILITY ANALYSIS OF CHAOS SYNCHRONIZATION

1.1 Introduction

This first chapter is devoted to the optimization and stability analysis of chaos synchronization. We will first briefly introduce the fundamental concepts of chaos theory, with a particular emphasis on those which will further be used throughout the thesis.

Hence, we will focus on the issue of chaos synchronization with unidirectional feedback coupling. The purpose will be to determine conditions under which a satisfying and highly stable synchronization can be achieved between two identical chaotic systems. After an overview of the existing methods, we will present a new technique based on approximated Fourier expansions and Floquet analysis. To validate our theory, we will demonstrate how it enables to stabilize and optimize the synchronization of single-well Duffing oscillators. Finally we extend the usefulness of our analytic technique to the case of external chaos control.

1.2 Chaos

1.2.1 Dynamical systems under study: ordinary and delay differential equations

In this thesis, we will focus on dynamical systems whose modeling can be achieved through *Ordinary Differential Equations* (ODEs) or through *Delay Differential Equations* (DDEs).

Let us consider a vectorial variable $\mathbf{x} = (x_1, ..., x_n)$ with $n \in \mathbf{N}^*$, a n-dimensional vectorial flow $\mathbf{F}$, and the ODE which reads

$$\dot{\mathbf{x}} = \mathbf{F}(\mathbf{x}) \text{ with } \mathbf{x}(0) = \mathbf{x}_0 \,. \tag{1}$$

The above equation may represent **dynamical system** if and only if the flow $\mathbf{F}$ fulfills the **Lipschitz condition**, which guarantees determinism in the sense that it

does not allow more than one solution for a given initial condition $\mathbf{x}_0$ [1]. In eq. (1), the initial conditions are defined by the n initial values for the components of the vector $\mathbf{x}$. Therefore, the dimensionality of the phase space corresponding to the flow $\mathbf{F}$ is n by definition. The above representation is said to be *autonomous* in the sense that no explicit dependence on time is accounted for. However, non-autonomous ODEs can easily be converted into an autonomous representation through a quite simple transformation.

In DDEs, the dynamics at each instant t depends on the value of the vector $\mathbf{x}$ at the same instant t, but also on the value of $\mathbf{x}$ at a previous instant $t-T$, with $T > 0$. If we introduce the delayed variable $\mathbf{x}_T \equiv \mathbf{x}(t-T)$ and the n-dimensional lipschitzian vectorial flow $\mathbf{G}$, a DDE should formally read

$$\dot{\mathbf{x}} = \mathbf{G}(\mathbf{x}, \mathbf{x}_T) \text{ with } \mathbf{x}(t) = \mathbf{g}(t) \text{ for } t \in [-T, 0]\,, \tag{2}$$

where $\mathbf{g}$ is an arbitrary n-dimensional vectorial function of time. Contrary to ODEs where the initial conditions were given by a discrete and finite set of values, initial conditions in DDEs should be indicated (by the mean of a function) for all the values contained into the continuous interval $[-T, 0]$, so that an *infinity* of values should be known to characterize the system. **That is why unlike the ODEs, DDEs are infinite-dimensional dynamical systems**. They are also referred to in the literareferred *Functional Differential Equations* because their initial condition is a function and not a discrete and finite set of values as it is the case for ODEs.

1.2.2 Definition of chaos

A continuous dynamical system is said to be **chaotic** when its temporal behavior is **deterministic**, **unpredictable** and **extremely sensitive** to initial conditions. In the state space, the corresponding attractor is an invariant manifold of *non-integer* (or *fractal*) dimension, so that it is generally referred to as a *strange attractor* [2].

Chaotic attractors are the result of a complex interplay between *stretching* and *folding* in the state space. Stretching is a linear process responsible for the sensitive dependence on initial conditions, while folding is a nonlinear phenomenon responsible for both the size limitation at macro-scale and fractal structure at micro-scale.

[1] For example, the flow $\dot{x} = \sqrt{x}$ is non-lipschitzian because it allows two distinct solutions $x(t) = 0$ and $x(t) = \frac{1}{4}t^2$ for the same initial condition $x_0 = 0$. It can therefore not modelize a deterministic dynamical system.

[2] Chaotic attractors are always strange, but strange attractors are not always chaotic [37, 38].

Two fundamental requirements are indispensable for chaos to appear in a continuous dynamical system. The first one is *nonlinearity*. Effectively, linear systems are always predictable, so that they can not be chaotic anyhow. In the state space, stretching is normally present for linear dynamical systems, but folding does never occur, as it is intrinsically related to nonlinearity. The second requirement is that the state space should mathematically be at least *three-dimensional*. Effectively, despite nonlinearity, folding is impossible in one-dimensional state spaces because of the *No-intersection theorem* while it is impossible in two-dimensional state spaces because of the *Poincaré-Bendixon theorem* [8].

When these two necessary (but not sufficient) conditions are fulfilled, chaos is likely to be observed in ODEs as well as in DDEs, and some quantifiers are needed to get a deeper insight into its various properties and characteristics.

1.2.3 Measures of chaos

Almost all the measures of chaos in dynamical systems rely on the fundamental property of sensitivity to initial conditions. This sensitivity is evaluated by calculating the divergence rate of initially nearby trajectories in the state space. In the case of ODEs, if we consider two initially nearby state variables $\mathbf{x}_0$ and $\mathbf{x}_0+\delta\mathbf{x}_0$, the deviation $\delta\mathbf{x}$ further evolves as

$$\delta\dot{\mathbf{x}} = \left[\frac{\partial \mathbf{F}}{\partial \mathbf{x}}\right]_{\mathbf{x}} \cdot \delta\mathbf{x} \;\text{ with }\; \delta\mathbf{x}(0) = \delta\mathbf{x}_0\,, \tag{3}$$

where $[\partial\mathbf{F}/\partial\mathbf{x}]$ is the *Jacobian* of the flow $\mathbf{F}$ evaluated on $\mathbf{x}$. The n eigenvalues of this Jacobian are referred to as **Lyapunov exponents**, and they can numerically be determined through

$$\lambda_k = \lim_{t\to+\infty} \frac{1}{t} \ln\left[\frac{|\delta x_k(t)|}{|\delta x_k(0)|}\right] \;\text{ with }\; k = 1, ..., n\,. \tag{4}$$

The n eigenvalues λ_k constitute the *Lyapunov spectrum* of the flow $\mathbf{F}$ for the initial condition $\mathbf{x}_0$. The *average Lyapunov spectrum* of an attractor is defined as the space average of the Lyapunov spectrum over its corresponding basin of attraction. Depending on its sign, an average Lyapunov exponent $\overline{\lambda}_k$ expresses convergence (when negative) or divergence (when positive) of nearby trajectories along the corresponding eigendirection in the attractor. Therefore, a dynamical system is said to be chaotic **if at least one average Lyapunov exponent $\overline{\lambda}_k$ is positive**. The system is said to be **hyperchaotic** if **more than one** average Lyapunov exponent is positive. Moreover, a greater number of positive $\overline{\lambda}_k$, as well as greater absolute values for each

of them when positive indicate a higher complexity in the state space and a higher unpredictability in the time domain.

Generally, if the initial value $\mathbf{x}_0$ is properly chosen, the resulting Lyapunov spectrum does not differ substantially from the average Lyapunov spectrum. Therefore, in this thesis, we will compute Lyapunov exponents without averaging. Sometimes, a unique Lyapunov exponent is defined as

$$\lambda = \lim_{t \to +\infty} \frac{1}{t} \ln \left[\frac{\|\delta \mathbf{x}(t)\|}{\|\delta \mathbf{x}(0)\|} \right] , \tag{5}$$

and its sign directly indicates chaoticity, even though it can not indicate hyperchaoticity.

For DDEs, the variational equation reads

$$\delta \dot{\mathbf{x}} = \left[\frac{\partial \mathbf{G}}{\partial \mathbf{x}} \right]_{\mathbf{x},\mathbf{x}_T} \cdot \delta \mathbf{x} + \left[\frac{\partial \mathbf{G}}{\partial \mathbf{x}_T} \right]_{\mathbf{x},\mathbf{x}_T} \cdot \delta \mathbf{x}_T \text{ with } \delta \mathbf{x}(t) = \delta \mathbf{g}(t) \text{ for } t \in [-T, 0] \tag{6}$$

and in this case, there is an *infinity* of Lyapunov exponents. That is why hyperchaos (displaying a very complex dynamics) is more likely to appear in DDEs than in ODEs.

From the Lyapunov exponents, other mathematical quantifiers can be determined to characterize the chaotic attractor [8]. Their interest principally lies on their very important physical meaning. The first one is the **Kolmogorov-Sinaï entropy**, which is inversely proportional to the time-interval over which the future evolution can be predicted. If the Lyapunov exponents are decrescently ordered, the Kolmogorov-Sinaï entropy can be expressed as

$$h_{KS} = \sum_{k=1}^{j} \lambda_k \, , \tag{7}$$

where j is the index of the last Lyapunov exponent for which the sum is positive.

The second quantifier is the **Kaplan-Yorke dimension**, which is a measure of the complexity of the attractor. Kaplan and Yorke did conjecture that this dimension is identical to the *information dimension*, which measures the difficulty to determine the instantaneous location of the system in the state space for a given precision. Using the Lyapunov exponents, the Kaplan-Yorke dimension is defined as

$$d_{KY} = j + \frac{\sum_{k=1}^{j} \lambda_k}{|\lambda_{j+1}|} = j + \frac{h_{KS}}{|\lambda_{j+1}|} \, . \tag{8}$$

As we will further see in the last chapter of the thesis for the cryptographic applications, the Kolmogorov-Sinaï entropy and the Kaplan-Yorke dimension are key parameters to evaluate the security of chaos-encrypted messages.

1.3 Chaos synchronization

The concept of **chaos synchronization** has first been introduced by Fujisaka and Yamada in 1983 [9], but the topic gained greater attention only seven years later, when Pecora and Carroll succeeded in constructing a convenient mathematical framework to analyze the phenomenon [10]. They showed that despite sensitivity to initial conditions, unpredictability and complexity of the attractors, distinct chaotic oscillators can synchronize when coupled, that is, their temporal oscillations can continuously remain in step with each other when certain requirements are met [40].

We will here define the general framework of synchronization theory on the base of unidirectionally coupled ODEs, assuming that the extension to DDEs can straightforwardly be achieved.

1.3.1 Definition

Let us consider the following set of unidirectionally coupled n-dimensional chaotic flows

$$\begin{aligned} \dot{\mathbf{x}} &= \mathbf{F}(\mathbf{x}) \\ \dot{\tilde{\mathbf{x}}} &= \tilde{\mathbf{F}}(\tilde{\mathbf{x}}, \mathbf{x}) \,, \end{aligned} \tag{9}$$

fulfilling the additional condition

$$\tilde{\mathbf{F}}(\tilde{\mathbf{x}}, \tilde{\mathbf{x}}) \equiv \mathbf{F}(\tilde{\mathbf{x}}) \,. \tag{10}$$

The first flow $\mathbf{F}$ of variable $\mathbf{x}$ is independent of the second: it is usually referred to as the *drive* or the *master* system. On the other hand, the second flow $\tilde{\mathbf{F}}$ of vector variables $\tilde{\mathbf{x}}$ and $\mathbf{x}$ is coupled to the first one: it corresponds to the *response* or *slave* system. Here, the overtilde ($\tilde{}$) has therefore been adopted to label the slave flow and the slave variables.

The slave system is said to be *identically synchronized* to the master if and only there exists a non-empty subset $\mathcal{E} \subset \mathbf{R}^n$ of the chaotic basin of attraction for which

$$\forall \, (\mathbf{x}_0, \tilde{\mathbf{x}}_0) \in \mathcal{E}^2, \;\; \lim_{t \to +\infty} \tilde{\mathbf{x}}(t) = \mathbf{x}(t) \,. \tag{11}$$

In other words, the term *identical synchronization* refers to a situation where owing to the coupling, we obtain $\tilde{\mathbf{x}}(t) = \mathbf{x}(t)$ in the asymptotic limit even though $\mathbf{x}_0 \neq \tilde{\mathbf{x}}_0$.

Various unidirectional coupling schemes can be set up to achieve synchronization. In this thesis, we will only consider **unidirectional continuous feedback** synchronization schemes, which is inspired from the continuous feedback chaos control

scheme proposed by Pyragas [41]. According to this technique, the slave vector-flow can explicitly be written as

$$\tilde{\mathbf{F}}(\tilde{\mathbf{x}}, \mathbf{x}) = \mathbf{F}(\tilde{\mathbf{x}}) - \mathbf{C}(\tilde{\mathbf{x}} - \mathbf{x}) \quad \text{with} \quad \mathbf{C}(\mathbf{0}) = \mathbf{0}\,, \tag{12}$$

where the continuous feedback vector-flow $\mathbf{C}$ is an arbitrary unidirectional coupling function. The particular case of *linear* feedback coupling is one of the most popular, and it is defined as

$$\tilde{\mathbf{F}}(\tilde{\mathbf{x}}, \mathbf{x}) = \mathbf{F}(\tilde{\mathbf{x}}) - [\mathbf{K}](\tilde{\mathbf{x}} - \mathbf{x})\,. \tag{13}$$

where $\mathbf{K}$ is a constant feedback gain matrix. It is important to note that in both eqs. (12) and (13), the requirement of condition (10) is always fulfilled. Along the same line, the original method proposed by Pecora and Carroll was a *substitution scheme*, which mathematically corresponds to the case when the elements of the feedback gain matrix $\mathbf{K}$ are either 0 or $\pm\infty$.

Even though the notion of identical synchronization is the most simple and the most intuitive, further investigation has shown that it should be integrated within the much more general context of *general synchronization*, which is supposed to occur when there exists a non-empty subset $\mathcal{E} \subset \mathbf{R}^n$ of the chaotic basin of attraction for which

$$\forall\, (\mathbf{x}_0, \tilde{\mathbf{x}}_0) \in \mathcal{E}^2,\ \lim_{t \to +\infty} \tilde{\mathbf{x}}(t) = \mathbf{h}\left[\mathbf{x}(t - T)\right]\,, \tag{14}$$

where $\mathbf{h}$ is a given vectorial function, and T a real value referred to as the *time lag*.

From the above definition, some important particular cases do arise. When $T = 0$, the synchronization is said to be *isochronous*, while it is said to be *achronous* when $T \neq 0$. More precisely, the term *delayed synchronization* is used when $T > 0$ because in that case, the slave tracks a past state of the master, while the term *anticipated synchronization* is used when $T < 0$ because this situation paradoxically indicates that the slave system forecasts the chaotic dynamics of the master. Also, generalized synchronization naturally degenerates into identical synchronization when $\mathbf{h}$ turns to be the identity vectorial function.

More complete mathematical formalisms have been proposed to define a unifying framework for the synchronization theory [42, 43, 44], and they intended to include highly correlated (but not exactly synchronized) states such as the *phase synchronization* state.

1.3.2 Conditions for synchronization

An important matter is to define the condition(s) under which synchronization occurs in coupled chaotic systems. This problem mathematically requires to define the synchronization basin $\mathcal{E}$ as a function of the coupling. Unfortunately, this problem is extremely complex and probably does not have any analytical solution. However, it is possible for the general case to derive numerically a *necessary* (but not sufficient) condition for chaos synchronization.

Let us consider the *deviation vector* $\mathbf{w}$ defined as

$$\mathbf{w}(t) = \tilde{\mathbf{x}}(t) - \mathbf{x}(t)\,, \tag{15}$$

which estimates the instantaneous mutual proximity between the master and the slave systems in the state space. The Euclidian norm $\|\mathbf{w}(t)\|$ of this deviation vector is referred to as *synchronization error*, and synchronization is achieved when this norm asymptotically converges to 0. At a linear approximation, the deviation vector obeys

$$\dot{\mathbf{w}} = \left[\frac{\partial \tilde{\mathbf{F}}}{\partial \tilde{\mathbf{x}}}\right]_{\mathbf{w}=\mathbf{0}} \cdot \mathbf{w} = [\mathbf{J}(\mathbf{x})] \cdot \mathbf{w}\,, \tag{16}$$

where $\mathbf{J}(\mathbf{x})$ is the (sub-)Jacobian of the *slave* flow evaluated with the *master* vector variable. Synchronization is achieved when the sub-Jacobian $\mathbf{J}(\mathbf{x})$ asymptotically drives $\mathbf{w}(t)$ to $\mathbf{0}$. A necessary condition for this to occur is that *all the eigenvalues of the sub-Jacobian* $\mathbf{J}(\mathbf{x})$*, referred to as* **sub-Lyapunov exponents***, should be negative* [10, 11]. However, since this sub-Jacobian is evaluated with the chaotic variable $\mathbf{x}$, the sub-Lyapunov exponents Λ_k can only be evaluated numerically as

$$\Lambda_k = \lim_{t\to+\infty} \frac{1}{t} \ln\left[\frac{|w_k(t)|}{|w_k(0)|}\right] \quad \text{with} \quad k = 1, ..., n \tag{17}$$

while analogously to the definition of Lyapunov exponents, a single sub-Lyapunov exponent defined as

$$\Lambda = \lim_{t\to+\infty} \frac{1}{t} \ln\left[\frac{\|\mathbf{w}(t)\|}{\|\mathbf{w}(0)\|}\right] \tag{18}$$

can directly indicate synchronization when negative.

1.4 Analytic stability study of synchronization manifolds

1.4.1 Overview of the existing analytical stability techniques

As explained earlier, the stability analysis of identically synchronized nonlinear oscillators is commonly carried out through the study of the asymptotical behavior of the deviation vector $\mathbf{w}(t) = \tilde{\mathbf{x}}(t) - \mathbf{x}(t)$ which estimates the instantaneous mutual proximity between the master and the slave systems in the state space. In general, depending on the coupling parameter(s), three distinct situations can arise from the stability study of $\mathbf{w}(t)$ as $t \to +\infty$.

The first of them occurs when $\|\mathbf{w}(+\infty)\| = 0$. In that case, the slave trajectory progressively tracks the master one, and consequently, stable synchronization is achieved: it is the regime of *linear stability*. The second situation arises when $0 < \|\mathbf{w}(+\infty)\| < +\infty$, that is, when the synchronization error does not converge to zero and does not diverge to infinity either. Here, the synchronization is said to have failed, since the oscillations of $\mathbf{x}$ and $\tilde{\mathbf{x}}$ remain uncorrelated despite the coupling: it is the regime of *nonlinear stability*. The third and last situation corresponds to $\|\mathbf{w}(+\infty)\| = +\infty$, *i. e.*, the coupling induces a sustained growth to infinity for the slave system variable: it is the regime of *instability*. This situation is obviously worst than the second, as it can lead to catastrophic consequences in real systems.

The aim of the stability study is therefore to determine under which conditions each of these three scenarii are encountered, and particularly important is to find the conditions under which the synchronized state is linearly stable. In fact, linear stability is not sufficient for applications of chaos synchronization: for example, parameter mismatch and noise, which are both unavoidable in real systems, can easily destroy a weakly stable synchronized state. Therefore, a key-issue is to look for the conditions under which a *maximal* stability is achieved for the synchronization manifold: it is said that the coupling has been *optimized*. As we will further see, chaotic systems have the best performance when this optimization criterium of maximal stability is fulfilled.

One of the most challenging task in synchronization theory is to derive *analytically* the necessary and/or sufficient conditions under which the coupling efficiently completes a robust and high-quality synchronization. Starting from now, we will use the non-autonomous vectorial representation which is mathematically less synthetic, but physically more expressive. In that representation, the master and slave vector-flows

can be rewritten as

$$\begin{aligned} \dot{\mathbf{x}} &= \mathbf{F}(\mathbf{x}, t) \\ \dot{\tilde{\mathbf{x}}} &= \mathbf{F}(\tilde{\mathbf{x}}, t) - \mathbf{C}(\tilde{\mathbf{x}} - \mathbf{x}) \quad \text{with} \quad \mathbf{C}(\mathbf{0}) = \mathbf{0}\,. \end{aligned} \tag{19}$$

At a linear approximation, the deviation related vector $\mathbf{w}$ obeys

$$\dot{\mathbf{w}} = \left[\left(\frac{\partial \mathbf{F}}{\partial \tilde{\mathbf{x}}} \right)_{\mathbf{w}=\mathbf{0}} - \left(\frac{\partial \mathbf{C}}{\partial \tilde{\mathbf{x}}} \right)_{\mathbf{w}=\mathbf{0}} \right] \cdot \mathbf{w} = [\mathbf{J}(\mathbf{x}, t)] \cdot \mathbf{w}\,, \tag{20}$$

and as we have earlier noted, synchronization is achieved when the Jacobian matrix $\mathbf{J}(\mathbf{x}, t)$ drives $\mathbf{w}$ to $\mathbf{0}$ at long term: for this situation to occur, it is known that the sub-Lyapunov exponents should necessarily be negative. However, that negativity condition has further been proved to be insufficient because these exponents describe the attractor as a whole whereas the stability of the synchronization manifold also depends on localized invariant sets embedded within that attractor [45]. Moreover, the sub-Lyapunov exponents can only be derived numerically, and thus do not give any analytic insight into the stability analysis problem. Therefore, several propositions have been made to overcome that deficiency.

The most straightforward is the "Ubiquitous Local Stability" method, which supposes that synchronization is stable when the *instantaneous* eingenvalues of the Jacobian $\mathbf{J}(\mathbf{x}, t)$ always have negative real parts everywhere within the chaotic attractor. The main advantage of his method is its simplicity. However, it is not a rigorous method and counter-examples can easily be found [46]. In fact, this ubiquitous local stability criterium is exclusively relevant for the long term behavior, and it fails to state about the stability of the transient motion, as the continuously changing eigenvalues and eigenvectors can induce parametric resonance.

Another interesting technique has been introduced by Gauthier and Bienfang [47], and it belongs to the family of Lyapunov function methods. They proposed to analyze the eigenvalues of the symmetric part of the Jacobian, that is $[\mathbf{J}(\mathbf{x}, t) + \mathbf{J}^T(\mathbf{x}, t)]$. This method is rigorous, but yields overly strong mathematical constraints for stability.

Finally, a different approach has also been proposed by Brown and Rulkov [48, 49] for the stability analysis of chaos synchronization. It relies on the decomposition of the Jacobian matrix into a constant part obtained through time-averaging $\langle \mathbf{J}(\mathbf{x}, t) \rangle$, and a variable part of mean-value $\mathbf{0}$ which corresponds to the difference $[\mathbf{J}(\mathbf{x}, t) - \langle \mathbf{J}(\mathbf{x}, t) \rangle]$. It is also a rigorous method, which is far-reaching in some cases, but whose interest is more qualitative than quantitative.

1.4.2 A new approach: Fourier expansion and Floquet analysis

We now introduce a new method to investigate the stability synchronization manifolds. This new analytical technique aims to succeed where the existing methods commonly fail, that is, in the description of the complex stability patterns which are obtained numerically as well as experimentally. In fact, the variational equation (20) resists to exact analytic treatments because the Jacobian is a function of the vector $\mathbf{x}$ which is a chaotic variable. To circumvent that problem, we propose an approach consisting in the replacement of the chaotic variable $\mathbf{x}$ by one of the T-periodic UPOs (Unstable Periodic Orbits) $\overline{\mathbf{x}}$ embedded within the chaotic attractor, and which like $\mathbf{x}$ obeys

$$\dot{\overline{\mathbf{x}}} = \mathbf{F}(\overline{\mathbf{x}}, t)\,. \tag{21}$$

Since $\overline{\mathbf{x}}$ is multiperiodic, it can be expanded in Fourier series as

$$\overline{\mathbf{x}}(t) = \sum_{k=0}^{+\infty} \left[\mathbf{A}_k \cos(k\omega t) + \mathbf{B}_k \sin(k\omega t)\right] \;\text{ with }\; \omega = \frac{2\pi}{T}\,. \tag{22}$$

Therefore, the vectorial Fourier components $\mathbf{A}_k$ and $\mathbf{B}_k$ can be recovered through the Ritz-Galerkin variational criterion according to

$$\int_0^T \left[\dot{\overline{\mathbf{x}}} - \mathbf{F}(\overline{\mathbf{x}}, t)\right] e^{ik\omega t}\, dt = \mathbf{0} \;\text{ with }\; k = 0, 1, ..., +\infty \tag{23}$$

The above equation yields an infinite set of coupled nonlinear algebraic equations which must be solved to determine the components the Fourier vectors. It is also an optimization equation in the sense that in general, the Ritz-Galerkin criterium only gives an approximation of $\mathbf{A}_k$ and $\mathbf{B}_k$. Finally, the stability analysis of the synchronized state is reformulated as a generalized Floquet problem

$$\dot{\mathbf{w}} = [\mathbf{J}(\overline{\mathbf{x}}, t)] \cdot \mathbf{w}\,. \tag{24}$$

Obviously, the above equation (24) is not mathematically equivalent to the original variational equation (20). The main difference is that the asymptotic behavior of the deviation vector $\mathbf{w}$ will now be decided by the Floquet multipliers instead of the sub-Lyapunov exponents. However, as we will further see, equation (24) offers a judicious qualitative and quantitative guidance for the choice of the suitable coupling parameter(s).

1.5 Example: synchronization of chaotic single-well Duffing oscillators

1.5.1 The system

The model we use for illustration was first introduced by Duffing in 1918, while investigating the nonlinear response of springs in mechanical systems [50]. The second order ODE he thus introduced to address this issue has rapidly turned into one of the most popular model of nonlinear dynamics, and today, its validity extends from electronics to atomic vibrations in solid-state physics. Under a generic form, the Duffing equation can be written as

$$\ddot{x} + \lambda\dot{x} + \alpha x + \gamma x^3 = f(t)\,, \tag{25}$$

where λ (> 0) stands for the linear damping, α for the linear stiffness, γ for the nonlinear stiffness, and $f(t)$ is the explicit time-dependent external excitation. When $\alpha < 0$ and $\gamma < 0$, the above equation is unstable, and therefore is not of much interest. But when $\alpha < 0$ and $\gamma > 0$, the system does possess asymmetric pair of stable fixed points $x_\pm = \pm\sqrt{-\alpha/\gamma}$: this is why it is referred to as the *double-well* Duffing model in the literature. On the other hand, when $\alpha > 0$, equation (25) only has one stable fixed point $x_0 = 0$ independently of the sign of γ: in this case, the system is referred to as the *single-well* Duffing model.

For our analysis, we have chosen to lay emphasis on the single-well model because it allows a wider diversity of chaotic attractors, since the nonlinear coefficient γ can be either positive or negative. The linear stiffness parameter α will be normalized to 1 for the sake of mathematical commodity and the external excitation $f(t)$ is chosen to be a sinusoidal function of amplitude F and frequency ω, so that our model now explicitly reads

$$\ddot{x} + \lambda\dot{x} + x + \gamma x^3 = F\cos(\omega t)\,. \tag{26}$$

We therefore have two distinct cases.

The first one corresponds to $\gamma > 0$, and it aims to describe the hardening effect of a nonlinear spring (the stiffness increases with the elongation). Depending on the chosen parameters, the system can display a chaotic behavior [51, 52]. Effectively, the system presents the classical jump phenomenon and nonlinear resonance for low forcing amplitude, but high external forcing gives rise to chaotic oscillations owing to the *pseudo*-two-wells potential configuration, as it can be seen in figure 1a.

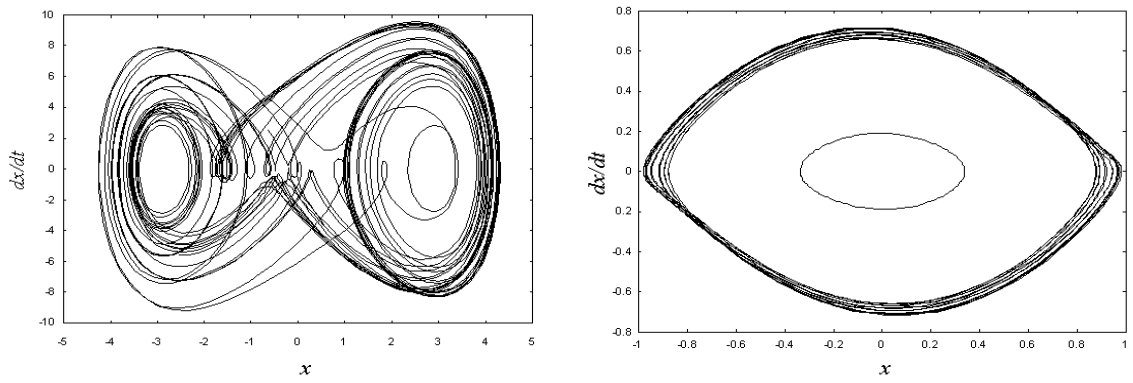

Figure 1: *Chaotic attractors for Single-Well Duffing Oscillators. a)* $\gamma > 0$ *case:* $\lambda = 0.2$*,* $\gamma = 1.0$*,* $F = 28.5$*,* $\omega = 0.86$*, with initial conditions* $(0, 0)$*; b)* $\gamma < 0$ *case:* $\lambda = 0.4$*,* $\gamma = -1.0$*,* $F = 0.23$*,* $\omega = 0.5255$ *with initial condition* $(0, 0)$ *for the inner limit-cycle, and* $(-0.3, 0.7)$ *for the outer chaotic trajectory.*

The second case corresponds to $\gamma < 0$, and it accurately describes the softening effect (the stiffness decreases with the elongation). Here, chaos is much more difficult to spot [53]. For example, the set of parameters in figure 1b can induce two different stable orbits depending on the initial conditions. We have an inner limit cycle, which has a relatively large basin of attraction including the trivial center point in the state space, and also an outer trajectory whose basin of attraction is a thin band separating the inner limit cycle and the unbounded solutions basins.

Throughout the thesis, the same sets of parameters will be used for these two cases, which will respectively be referred to as "**the** $\gamma > 0$ **case**" and "**the** $\gamma < 0$ **case**". Also, the numerical simulations will be performed with the fourth-order Runge-Kutta algorithm, while all nonlinear algebraic equations will be solved with the Newton-Raphson algorithm.

1.5.2 Stability analysis

To illustrate the validity of our approach, we aim to study the stability of synchronized single-well Duffing oscillators when the coupling is ensured through a linear feedback term. The corresponding set of coupled ODEs can be written as so that our model now explicitly reads

$$\begin{aligned} \ddot{x} + \lambda\dot{x} + x + \gamma x^3 &= F\cos(\omega t) \\ \ddot{\tilde{x}} + \lambda\dot{\tilde{x}} + \tilde{x} + \gamma\tilde{x}^3 &= F\cos(\omega t) - K(\tilde{x} - x)\,, \end{aligned} \tag{27}$$

where the scalar parameter K stands for the feedback unidirectional coupling term between the master oscillator x and the slave $\tilde{x}$.

The deviation variable can here be chosen as a scalar according to $\xi = \tilde{x} - x$, and it obeys at the first order to the following linear differential equation

$$\ddot{\xi} + \lambda\dot{\xi} + (1 + K + 3\gamma x^2)\xi = 0\,. \tag{28}$$

This variational equation is the equivalent of equation (20) in the vectorial formalism. As we earlier noted, synchronization is therefore achieved when ξ asymptotically decays to zero. In the spirit of equation (24), we need to replace the chaotic variable $x(t)$ in equation (28) by its related UPO $\overline{x}(t)$ defined as

$$\overline{x}(t) = \sum_{k=0}^{+\infty} C_k \cos(k\omega t - \varphi_k) \;\text{ with }\; k = 0, 1, ..., +\infty\,, \tag{29}$$

and the scalar Fourier coefficients C_k and φ_k should satisfy the Ritz-Galerkin criterium following

$$\int_0^{2\pi/\omega} \left[F\cos(\omega t) - (\ddot{\overline{x}} + \lambda\dot{\overline{x}} + \overline{x} + \gamma\overline{x}^3)\right] e^{ik\omega t}\, dt = 0 \;\text{ with }\; k = 0, 1, ..., +\infty\,. \tag{30}$$

Normally, equation (30) yields an infinite set of coupled nonlinear algebraic equations whose unknowns are the C_k and φ_k coefficients. If we straightforwardly consider the multiperiodicity of $\overline{x}(t)$ in equation (28), the stability analysis would require the resolution of an ODE with multiperiodic parametric excitation. Even though the related study would logically yield the most satisfying results, it should be noted that unfortunately, the consequent stability boundaries can hardly be derived in that case, even within the framework of perturbation theory.

In fact, such a complexity can be avoided when the chaotic attractor is almost simply folded, or equivalently, when the corresponding Fourier spectrum is overly dominated by a single spectral frequency. In that case, the stability analysis can be done with *a single* pair (C_k, φ_k), instead of the infinite set (k from 0 to $+\infty$). For example, figure 2 displays the Fourier spectra related to the $\gamma > 0$ and $\gamma < 0$ cases respectively. When $\gamma > 0$, energy is mainly distributed in very sharp bands around the odd harmonics of the forcing frequency ω (figure 2a). However, the major part of the energy lies around the fundamental frequency. On the other hand, when $\gamma < 0$, both the phase portrait (figure 1b) and the Fourier spectrum (figure 2b) agree that the simple-folding hypothesis is quasi-perfectly fulfilled. Hence, in both cases, the stability analysis can satisfyingly be done with the single pair (C_1, φ_1), and the UPO may simply be approximated by

$$\overline{x}(t) = C_1 \cos(\omega t - \varphi_1)\,. \tag{31}$$

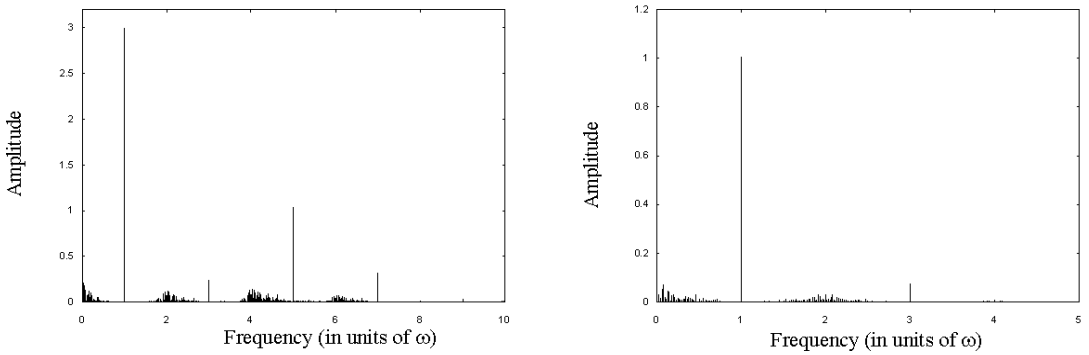

Figure 2: *Fourier spectra for Single-Well Duffing Oscillators. a) $\gamma > 0$ case; b) $\gamma < 0$ case.*

Therefore, if we replace the chaotic variable x by the approximated uniperiodic UPO $\overline{x}$ of equation (31), the variational equation (28) may be rewritten under the form of a canonical Mathieu equation

$$\frac{d^2\eta}{d\tau^2} + [\mu + 2\alpha\cos(2\tau - 2\varphi)]\ \eta = 0\,, \tag{32}$$

with the following rescalings

$$\begin{aligned} \tau &= \omega t \\ \eta(\tau) &= \xi\,\exp\left(\frac{\lambda\tau}{2\omega}\right) \\ \mu &= \frac{1}{\omega^2}\left[1 + K + \frac{3}{2}\gamma C_1^2 - \frac{\lambda^2}{4}\right] \\ \alpha &= \frac{3\gamma C_1^2}{4\omega^2}\,. \end{aligned} \tag{33}$$

Also note that the index of φ has been removed for the sake of simplicity ($\varphi \equiv \varphi_1$). It appears from equation (33) that the coupling coefficient K only influences the Mathieu parameter μ, but not the parameter α anyway.

The solution of the Mathieu equation (32) has the form [54, 55, 56]

$$\eta(\tau) = e^{\theta\tau}\,\phi(\tau)\,, \tag{34}$$

where θ is a complex number and

$$\phi(\tau) = \sum_{n=-\infty}^{+\infty} \phi_n\, e^{2in\tau} \tag{35}$$

is a π-periodic function, so that

$$\eta(\tau) = \sum_{n=-\infty}^{+\infty} \phi_n\, e^{(\theta+2in)\tau}\,. \tag{36}$$

Inserting equation (36) into equation (32) yields an infinite homogeneous set of linear algebraic equations, which may have solutions if and only if the associated determinant is equated to zero. In a symbolic form, this tridiagonal determinant can be expressed as [56]

$$\Delta(\theta,\mu,\alpha)=\left\|\frac{\left(\mu+(\theta+2in)^2\right)\delta_{m,n}+\alpha\left(e^{2i\varphi}\delta_{m,n-1}+e^{-2i\varphi}\delta_{m,n+1}\right)}{\mu-(2m)^2}\right\|=0 \tag{37}$$

where the $\delta_{m,n}$ are the Kronecker symbols, with m and n varying from $-\infty$ to $+\infty$. $\Delta(\theta,\mu,\alpha)$ is usually referred to as the **infinite Hill determinant**, and one can show that

$$\Delta(\theta,\mu,\alpha)=\Delta(0,\mu,\alpha)-\frac{\sin^2\left(\frac{1}{2}i\pi\theta\right)}{\sin^2\left(\frac{1}{2}\pi\sqrt{\mu}\right)} \tag{38}$$

where i is the unit complex number. Therefore, one can deduce that

$$\theta=\pm\frac{2i}{\pi}\arcsin\sqrt{\Delta(0,\mu,\alpha)\,\sin^2\left(\frac{1}{2}\pi\sqrt{\mu}\right)} \tag{39}$$

and since we have

$$\xi=\phi(\tau)\,\exp\left[\left(\theta-\frac{\lambda}{2\omega}\right)\tau\right] \tag{40}$$

from equation (33), it therefore results that the ξ oscillations either exponentially decay to zero (linear stability) or exponentially increase to infinity (linear instability), unless $\Re(\theta)=\lambda/2\omega$. According to Floquet theory, the transition from stability to instability (or the inverse) can only occur in two distinct cases:

- π-periodic transition: $\theta=\lambda/2\omega$

$$\Delta(0,\mu,\alpha)+\frac{\sinh^2\left(\frac{\lambda\pi}{4\omega}\right)}{\sin^2\left(\frac{1}{2}\pi\sqrt{\mu}\right)}=0 \tag{41}$$

- 2π-periodic transition: $\theta=i+\lambda/2\omega$

$$\Delta(0,\mu,\alpha)-\frac{\cosh^2\left(\frac{\lambda\pi}{4\omega}\right)}{\sin^2\left(\frac{1}{2}\pi\sqrt{\mu}\right)}=0 \tag{42}$$

Equations (41) and (42) define a set of curves in the (μ,α) parametric plane, as schematically represented in figure 3. They constitute a stability map which is commonly referred to as the *Strutt diagram*. In the case of the non-dissipative Mathieu

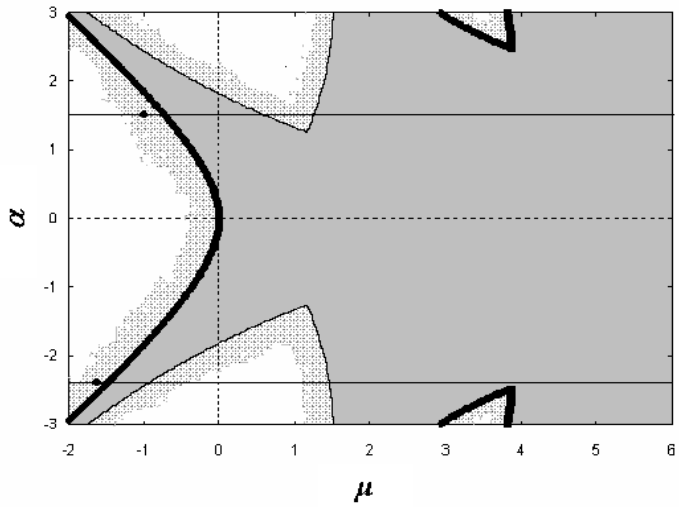

Figure 3: *The Strutt diagram. The linearly stable area is darkly shaded, the nonlinearly stable belt is lightly shaded, and the unstable area is in blank. The π-periodic boundaries are in thick lines, while the 2π-periodic boundaries are in thin lines. The figurative points of the $\gamma > 0$ case ($\alpha > 0$) and $\gamma < 0$ case ($\alpha < 0$) at $K = 0$ have been represented. The two cases have been represented in the same figure for the sake of simplicity.*

equation, the Hopf theorem states that for a given value of α, stable values of μ are those which are strictly situated between boundaries of different types [54]. In our dissipative case, it graphically implies that the stability domain is the darkly shaded area enclosed between the π- and 2π-periodic boundaries in figure 3.

If we mathematically define the new real function

$$\Gamma(\mu,\alpha) = \begin{cases} \Delta(0,\mu,\alpha)\,\sin^2\left(\frac{1}{2}\pi\sqrt{\mu}\right) & \text{if } \mu \geq 0 \\ -\Delta(0,\mu,\alpha)\,\sinh^2\left(\frac{1}{2}\pi\sqrt{-\mu}\right) & \text{if } \mu \leq 0 \end{cases}, \tag{43}$$

then the analytic condition of linear stability is the following, according to the Hopf theorem

$$-\sinh^2\left(\frac{\lambda\pi}{4\omega}\right) < \Gamma(\mu,\alpha) < \cosh^2\left(\frac{\lambda\pi}{4\omega}\right). \tag{44}$$

Therefore, from a conventional approach, the Strutt diagram is divided into two distinct areas: the area of linear stability ($\xi(t) \to 0$), and the area of linear instability ($\xi(t) \to \pm\infty$). The boundaries between these two areas can either be π-periodic if $\Gamma(\mu,\alpha) = -\sinh^2(\lambda\pi/4\omega)$ (thereby inducing $\xi(t) = \xi(t+\pi/\omega)$), or 2π-periodic if $\Gamma(\mu,\alpha) = \cosh^2(\lambda\pi/4\omega)$ (thereby yielding $\xi(t) = \xi(t+2\pi/\omega)$).

However, the Strutt diagram may be divided into two areas only at the linear approximation. When the variational equations aim to decide the stability of a nonlinear system, the variational nonlinear terms we have discarded in equation (28) play a predominant stabilizing role, thereby leading to the emergence of a third area in the Strutt diagram. Effectively, due to these nonlinear variational terms, there is a buffer zone between the linearly stable and linearly unstable areas: it is an area of *nonlinear stability* (which is however linearly unstable), where $|\xi(t)|$ does not decay to zero and does not grow to infinity either. The inner boundaries of this buffer zone are the periodic boundaries of the linearly stable area, while its outer boundaries are very irregular, sometimes fractal-like, and are shared exclusively with the unstable area. In figure 3, this domain of nonlinear stability has been represented as a lightly shaded belt surrounding the linearly stable zone, while the unstable domain remains unshaded.

Let us assume that the local width of this belt is $\Lambda(\mu^{(k\pi)}, \alpha)$, where the couple $(\mu^{(k\pi)}, \alpha)$ is the related point situated on a $k\pi$-periodic boundary of the Strutt diagram ($k = 1$ or 2). Hence, the analytical condition of nonlinear stability can be approximated by

$$\left| (\mu - \mu^{(k\pi)}) \left[\frac{\partial \Gamma(\mu, \alpha)}{\partial \mu} \right]_{(\mu = \mu^{(k\pi)})} \right| < \frac{\Lambda(\mu^{(k\pi)}, \alpha)}{|\mu^{(\pi)} - \mu^{(2\pi)}|} \cosh\left(\frac{\lambda \pi}{2\omega} \right) . \tag{45}$$

Here, $(\mu^{(k\pi)}, \alpha)$ is the nearest boundary point relatively to the representative point $M(\mu, \alpha)$ of the coupled system, while $|\mu^{(\pi)} - \mu^{(2\pi)}|$ is the length of the segment (belonging to the $\alpha = const$ horizontal line) lying within the nearest stability interval. For the geometrical reasoning, the local belt width $\Lambda(\mu^{(k\pi)}, \alpha)$ can be replaced without any inconvenience by its average value $\overline{\Lambda}$.

We can now analyze through the Strutt diagram what is happening in the master-slave system when the coupling strength K is continuously increased. We first recall that since α is independent of K, the figurative point M of the coupled system in the Strutt diagram is just moving from left to right along a straight horizontal line $\alpha = const$ when K is varied. Starting from $\mu = -\infty$ (*i.e.*, according to equation (33)), this point will alternatively pass through the various areas of the Strutt diagram. Hence, the stability pattern will consist in the general case of intermingled intervals of instability, nonlinear stability and linear stability.

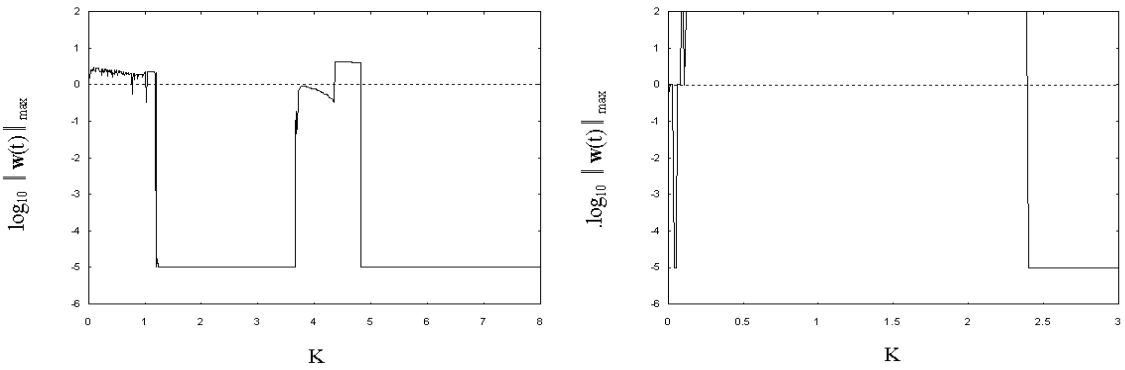

Figure 4: *Variations of the maximal synchronization error* $\|\mathbf{w}(t)\|_{max}$ *in a semi-logarithmic scale when* K *is increased. a)* $\gamma > 0$ *case; b)* $\gamma < 0$ *case.*

1.5.3 Numerical simulations

The numerical simulations we have performed completely confirm the above analysis. In figure 4, we have represented the maximal synchronization error $\|\mathbf{w}(t)\|_{max}$ as a function of the coupling parameter K, with $\mathbf{w} = (x, \dot{x})$. We have assumed that stable and robust synchronization is ensured for a given K provided that the related maximal synchronization error is smaller than 10^{-5}, so that the synchronization intervals are indicated by horizontal segments of equation $\log_{10}(\|\mathbf{w}(t)\|_{max}) = -5$.

In figure 4a, the $\gamma > 0$ case is considered. When $K = 0$, a high synchronization error is obviously noticed, since the two chaotic oscillators are independent. This means that the representative point M is initially in the nonlinear buffer zone of the Strutt diagram. For low K values, the master and the slave sub-systems remain uncorrelated, so that $\|\mathbf{w}(t)\|_{max}$ is still high. Geometrically, we are still in the vicinity of the initial position, *i.e.*, in the buffer area. A first π-periodic boundary is overstepped for $K = 1.21$, and thereby stable synchronization consequently occurs until $K = 3.66$ (first 2π-periodic Hopf boundary). From that threshold, the point $M(\mu(K), \alpha)$ re-enters into the buffer area and synchronization is lost. When K is further increased, M reaches the second 2π-periodic Hopf boundary at $K = 4.83$ and definitively remains in the linearly stable zone, so that synchronization is preserved for any higher value. Such behavior had also be numerically found for the synchronization of Duffing oscillators without linear stiffness [57], and the theory we have developed is still valid for that particular case. As in our case, the complete bifurcation sequence can be schematically recovered in figure 3 by the traveling motion of the representative point M on the upper half-plane straight horizontal line ($\alpha > 0$).

For the $\gamma < 0$ case (figure 4b), the stability pattern is quite different. We still have a high $\|\mathbf{w}(t)\|_{max}$ value for $K = 0$, but synchronization is established as soon as $K > 0.04$. This can be explained by the fact that $\overline{\Lambda}$ is very thin, and hence $M(\mu(0^+), \alpha)$ rapidly oversteps the first π-periodic boundary. However, synchronization is also very soon lost at $K = 0.08$ (first 2π-periodic Hopf bifurcation) for instability, until $K = 2.39$ (second 2π-periodic Hopf bifurcation). From there, synchronization is also indefinitely observed. Therefore, nonlinear stability is scarcely witnessed here: generally, the slave oscillator either synchronizes with the master or becomes unstable. In this case, the sub-Lyapunov exponent can straightforwardly be identified to $\Re(\theta - \lambda/2\omega)$ since $\overline{\Lambda} \approx 0$. Nevertheless, the influence of $\Lambda(\mu, \alpha)$ should not be completely neglected: it seems that for $\gamma < 0$, the belt becomes almost exclusively fractal, *i.e.*, as if it was "diluted" in the linearly unstable zone. The main consequence is that depending on the initial conditions and on the value of K, nonlinear stability can however be witnessed. The geometrical equivalence of this bifurcation sequence is also represented in figure 3 on the lower half-plane ($\alpha < 0$).

Finally, one should note that when $K \to +\infty$, instability is uniformly observed in both $\gamma > 0$ and $\gamma < 0$ cases. This is easily understandable from a Strutt diagram analysis: it would mean that the representative point of the system moves towards the semi-infinite unstable blank area.

1.5.4 Delayed synchronization

The purpose of delayed feedback synchronization is to achieve the convergence of the slave oscillator $\tilde{x}(t)$ towards a past state $x(t - \tau) \equiv x_\tau(t)$ of the master through

$$\begin{aligned} \ddot{x} + \lambda\dot{x} + x + \gamma x^3 &= F\cos(\omega t) \\ \ddot{\tilde{x}} + \lambda\dot{\tilde{x}} + \tilde{x} + \gamma\tilde{x}^3 &= F\cos(\omega t) - K(\tilde{x} - x_\tau)\,. \end{aligned} \tag{46}$$

An interesting feature of this type of synchronization is that it mathematically transforms an ODE into a DDE, that is, a low-dimensional system into an infinite-dimensional one. When this delay τ is taken into account, the deviation variable $\xi = \tilde{x} - x_\tau$ rather at a linear approximation obeys the following parametric equation

$$\ddot{\xi} + \lambda\dot{\xi} + (1 + K + 3\gamma x_\tau^2)\xi = -2F\sin\frac{\omega\tau}{2}\sin\left(\omega t - \frac{\omega\tau}{2}\right), \tag{47}$$

so that ξ is now submitted to an external excitation. When τ is a multiple of the period $T = 2\pi/\omega$ (*i.e.*, $\tau = nT$, n being a strictly positive integer), this external excitation vanishes and equation (47) is no longer different from equation (28), so that

the subsequent stability analysis is exactly identical. Hence, when $\tau = nT$, *delayed and non-delayed chaos synchronization have exactly the same stability pattern and therefore occur under exactly the same conditions.* On the other hand, when $\tau \neq nT$, synchronization can not occur: because of the external excitation in (47), the slave oscillator can be tuned to the master one only with a limited precision.

1.6 Extension of the method to chaos control

Chaos control consists in recovering a periodic dynamics from the initially chaotic one. The idea of chaos control was for the first time introduced by Ott, Grebogi and Yorke in 1990 [58], and since then, chaos control theory has arisen as a classical and thoroughly investigated topic in nonlinear dynamics [39, 59].

Investigation in the field of chaos control is generally developed along two dintinct classes of problems. The first class looks at chaos as a negative feature. For example, the unpredictability attached to chaos may generally be considered as an undesirable phenomenon in some applications where high precision or high predictability is required [60]. This point of view is prevalent in mechanical and electrical engineering where it is not uncommon to witness undesired irregular behavior in strongly excited nonlinear systems [61].

At the opposite, the second class looks at chaos as a positive feature. Effectively, quite a large number of UPOs are usually embedded within the chaotic attractors, so that the same system can *flexibly* be tuned with a chaos control scheme from a given UPO to any other one. It is well established today that brain waves and cardiac pulsations sometimes display a chaotic behavior, and it has yet been speculated that chaos control is used on purpose to flexibly switch the heart and the brain to a wide variety of different periodic biological rhythms [62, 63, 64].

Since the pioneering work of Ott, Grebogi and Yorke, a very high number of control schemes have been and are still proposed in the literature. However, only *feedback control schemes* have succeeded in gaining higher interest owing to their conceptual simplicity and to their easier practical implementation. We will here lay emphasis on *external feedback control*, which is one of the most important type of feedback chaos control [41].

1.6.1 General case

External feedback control techniques have been commonly used in automatic engineering for quite a long time. Very soon, it has been proposed as an interesting candidate to also ensure chaos control. At the difference of the time-delayed control scheme, external feedback control does not aim to reach the UPOs of the attractor, but rather to enable to tune the chaotic attractor to an arbitrary T-periodic target orbit $\hat{\mathbf{x}}(t)$ following

$$\dot{\mathbf{x}} = \mathbf{F}(\mathbf{x}) - \mathbf{C}(\mathbf{x} - \hat{\mathbf{x}}) \,, \tag{48}$$

where $\mathbf{C}$ is a feedback control vectorial function fulfilling $\mathbf{C}(\mathbf{0}) \equiv \mathbf{0}$. It is important to note that in this scheme, perfect control tuning from $\mathbf{x}$ to $\hat{\mathbf{x}}$ *cannot* be achieved because $\hat{\mathbf{x}}(t)$ *is not* a solution of the nonlinear flow $\mathbf{F}$, so that the feedback term cannot perfectly vanish. However, the principal interest of this control scheme is twofold: firstly, its extreme simplicity because the initial ODE is just converted into another ODE (at the opposite of time-delayed feedback schemes where ODEs are transformed into DDEs), and secondly, the target orbit can be chosen and defined arbitrarily, inclusively as a non-periodic orbit.

The deviation vector $\mathbf{v} = \mathbf{x} - \hat{\mathbf{x}}$ obeys the following vectorial equation in linear approximation

$$\dot{\mathbf{v}} = \left[\left(\frac{\partial \mathbf{F}}{\partial \mathbf{x}} \right)_{\mathbf{x}=\hat{\mathbf{x}}} - \left(\frac{\partial \mathbf{C}}{\partial \mathbf{x}} \right)_{\mathbf{x}=\hat{\mathbf{x}}} \right] \cdot \mathbf{v} + \left[\dot{\hat{\mathbf{x}}} - \mathbf{F}(\hat{\mathbf{x}}, t) \right] = [\mathbf{J}(\hat{\mathbf{x}}, t)] \cdot \mathbf{v} + \mathbf{R}(t) \,, \tag{49}$$

where $[\mathbf{J}(\hat{\mathbf{x}}, t)]$ is a periodic Jacobian, and $\mathbf{R}(t)$ a periodic residue function. The control in this case will be stable if the Jacobian asymptotically drives the homogeneous component $\mathbf{v}_H$ of $\mathbf{v}$ to $\mathbf{0}$. The consequent stability analysis will therefore be identical to the one we have done for the stability of synchronization manifolds. On the other hand, the residue $\mathbf{R}(t)$ (which is uniformly equal to $\mathbf{0}$ if the target orbit is an UPO) plays the role of an external excitation in equation (49), and sustains the non-homogeneous component $\mathbf{v}_I$ of $\mathbf{v}$. Here, optimization will be achieved when this residue is the smallest possible, that is, when the control is led towards an uniperiodic target orbit which is near an UPO [65].

1.6.2 The example of single-well Duffing oscillators

We can control a single-well Duffing oscillator with the following external feedback chaos control scheme

$$\ddot{x} + \lambda \dot{x} + x + \gamma x^3 = F \cos(\omega t) - K(x - \hat{x}) \cdot H(t - T_0) \,, \tag{50}$$

where K is the feedback strength parameter, H is the Heaviside function which is equal to 0 when $x < 0$ and to 1 when $x \geq 0$, so that the control is assumed to be active only when $t \geq T_0$.

In this case, the residue explicitly reads

$$R(t) = (\ddot{\hat{x}} + \lambda\dot{\hat{x}} + \hat{x} + \gamma\hat{x}^3) - F\cos(\omega t)\,, \tag{51}$$

and an optimized uniperiodic target orbit can be found through the Ritz-Galerkin criterion

$$\int_0^{2\pi/\omega} R(t)\, e^{i\omega t}\, dt = 0\,. \tag{52}$$

From the Ritz-Galerkin procedure (52), the amplitude and phase of the target orbit $\hat{x} = C_1\cos(\omega t - \varphi_1)$ can be determined through the resolution of the algebraic system

$$\begin{aligned} \left[\left((1-\omega^2) + \frac{3}{4}\gamma C_1^2\right)^2 + (\lambda\omega)^2\right] C_1^2 &= F^2 \\ \varphi_1 = \tan^{-1}\left[\frac{\lambda\omega}{(1-\omega^2) + \frac{3}{4}\gamma C_1^2}\right]&, \end{aligned} \tag{53}$$

so that the residue becomes

$$R(t) = -\beta\cos(3\omega t - 3\varphi_1) \;\text{ with }\; \beta = \frac{1}{4}\gamma C_1^3\,. \tag{54}$$

For the $\gamma > 0$ case, there is a single solution

$$(C_1, \varphi_1) = (3.323,\, 0.020) \tag{55}$$

while for the $\gamma < 0$ case, we have three mathematical solutions

$$(C_1, \varphi_1) \in \Big\{(0.343,\, 0.319),\;\; (0.864,\, 0.911),\;\; (1.031,\, -1.230)\Big\}\,. \tag{56}$$

For this later case, one can notice that the first solution corresponds to the regular inner limit cycle, the second corresponds to the chaotic attractor band, while the third corresponds to an unstable solution. Therefore, we will only study the stability of chaos control for the first two orbits.

The scalar deviation variable $\varepsilon(t) = x(t) - \hat{x}(t)$ obeys in the linear approximation to

$$\ddot{\varepsilon} + \lambda\dot{\varepsilon} + \left[\left(1 + K + \frac{3}{2}\gamma C_1^2\right) + \frac{3}{2}\gamma C_1^2\cos(2\omega t - 2\varphi_1)\right]\varepsilon = -\beta\cos(3\omega t - 3\varphi_1)\,. \tag{57}$$

The homogeneous counterpart of equation (57) exactly corresponds to the canonical Mathieu equation (32). Therefore, as the coupling K is increased, the stability pattern of our external feedback chaos control scheme can be analyzed in the Strutt diagram in the same way as in the case of chaos synchronization with feedback coupling.

Qualitatively, numerical simulations agree with the above analysis. For the $\gamma > 0$ case, we first have an interval of instability, followed by intermingled intervals of nonlinear and linear stability, and at last a semi-infinite interval of linear stability. For the $\gamma < 0$ case, as it was the case for synchronization, the control is either linearly stable or unstable, and nonlinear stability is witnessed only in exceptional cases (for example, when $K = 0$). The α values in this case lead to linear stability patterns of the kind $]K_{b1}, K_{b2}[\cup]K_{b3}, +\infty[$ with ($K_{b1} = -0.434$; $K_{b2} = 0.017$; $K_{b3} = 1.228$) for the control towards the first solution, and ($K_{b1} = -0.231$; $K_{b2} = 0.008$; $K_{b3} = 2.762$) for the control towards the first one.

If we introduce the parameter h as the *precision of the control*, the condition of control simply reads $|\varepsilon(t)| < h$ for $t > T_0 + T_{con}$, where T_0 is the onset time of the control, and T_{con} is the duration of the control, that is, the time needed to fulfill the control condition. In general, there is also a critical value K_{cr} below which control cannot be achieved. From equation (57), this critical coupling value can be evaluated with a good approximation as

$$K_{cr} = 9\omega^2 - 1 - \frac{3}{2}\gamma C_1^2 + \sqrt{\left(\frac{\gamma C_1^3}{4h}\right)^2 - 9\lambda^2\omega^2} \quad \text{assuming} \quad h < \frac{|\gamma| C_1^3}{12\lambda\omega}\,. \tag{58}$$

Figures 5a and 5b show the quasi-perfect coincidence between formula (58) and the results of the numerical simulation of equation (50). It naturally appears that K_{cr} is a decreasing function of the precision h.

The duration T_{con} of the control can also be derived from (57), and it explicitly reads

$$T_{con} = \frac{2}{\lambda}\,\ln\left[\frac{\sqrt{\dot{\varepsilon}^2(T_0) + \frac{[\dot{\varepsilon}(T_0)+\lambda\varepsilon(T_0)/2]^2}{1+K+3\gamma C_1^2/2-\lambda^2/4}}}{h - \frac{|\gamma|C_1^3/4}{\sqrt{(1+K+3\gamma C_1^2/2-9\omega^2)^2+9\lambda^2\omega^2}}}\right]. \tag{59}$$

It appears that T_{con} is a decreasing function of K, and one can find that

$$T_{con,min} = \lim_{t\to+\infty} T_{con} = \frac{2}{\lambda}\,\ln\left[\frac{|\varepsilon(T_0)|}{h}\right] \tag{60}$$

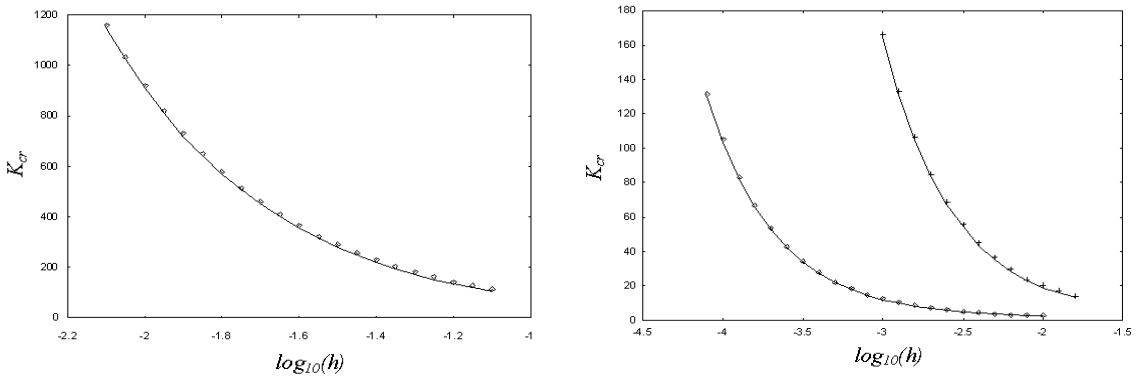

Figure 5: *Variations of K_{cr} as a function of $\log_{10}(h)$ (full lines for analytic results, squares and crosses for numerical results). a) $\gamma > 0$ case; b) $\gamma < 0$ case. The first solution corresponds to the lower curve, and the second solution to the upper one.*

is the minimum duration under which no control can be achieved. This result is of great practical interest. *A priori*, one could have naively thought that the control could have been achieved as fast as desired, just depending on K. Figure 6 does not support that assumption. For example, figure 6a shows that a feedback coefficient $K = 10$ is sufficient to ensure an optimal control (with approximately the minimum T_{con}). Hence, the above analysis enables us to avoid an unavailing waste of input energy by preventing us from a useless increase of the control parameter K.

A quite interesting phenomenon can also be observed in figure 6: the curves obtained through the numerical simulation of equation (50) are not smooth. We need to refer again to Floquet theory to explain this phenomenon. It should be first noted that K_{cr} always belongs to the last semi-infinite stability domain, and this implies that all the values beyond K_{cr} are linearly stable. The θ exponent, whose real part enables to determine the decay rate according to equation (40), can be explicitly defined as

$$\begin{aligned}
\text{For } \; -\sinh^2\left(\frac{\lambda\pi}{4\omega}\right) < \Gamma(\mu,\alpha) \leq 0, \qquad & \theta = \pm 2i \pm \frac{2}{\pi}\sinh^{-1}\sqrt{-\Gamma(\mu,\alpha)}\,, \\
\text{For } \; 0 < \Gamma(\mu,\alpha) < 1, \qquad & \theta = \pm\frac{2i}{\pi}\sin^{-1}\sqrt{\Gamma(\mu,\alpha)}\,, \\
\text{For } \; 1 \leq \Gamma(\mu,\alpha) < \cosh^2\left(\frac{\lambda\pi}{4\omega}\right), \qquad & \theta = \pm i \pm \frac{2}{\pi}\cosh^{-1}\sqrt{\Gamma(\mu,\alpha)}\,. \qquad (61)
\end{aligned}$$

It can therefore be deduced that the associated durations of control may respectively

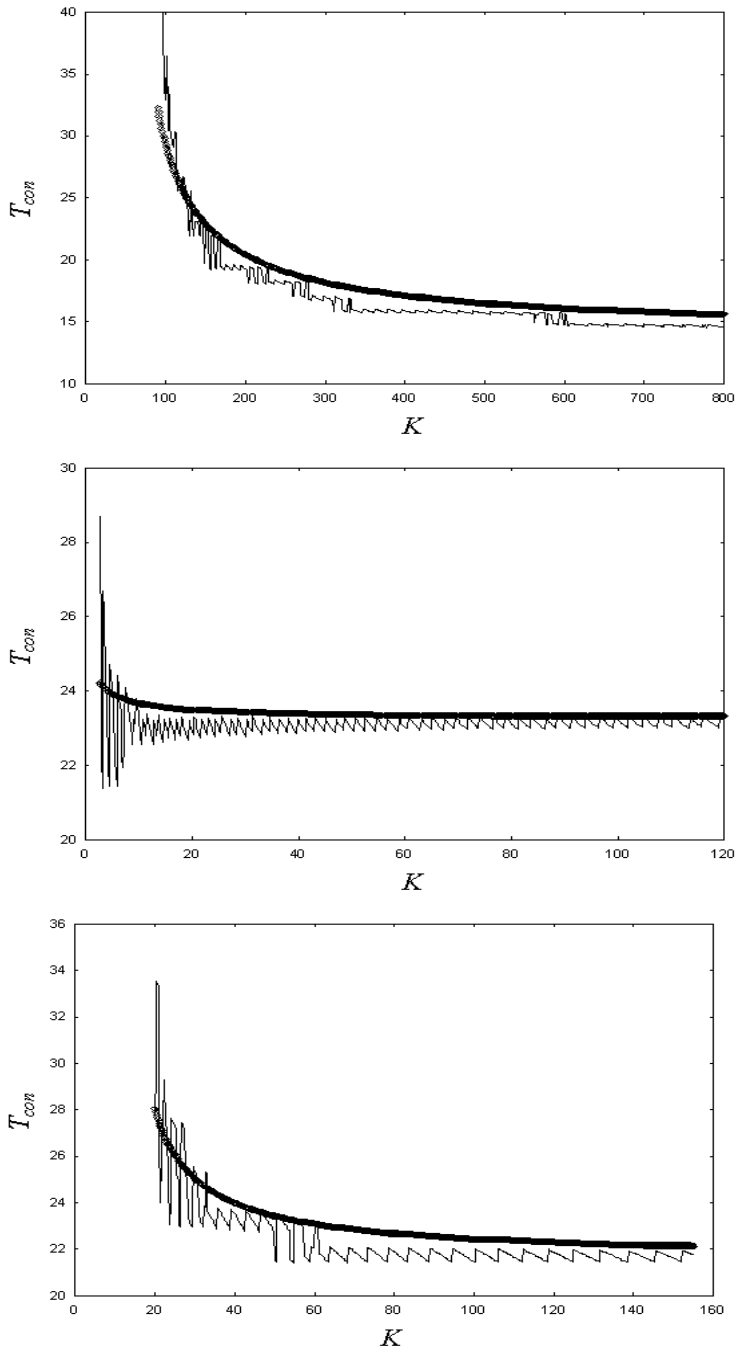

Figure 6: *Variations of T_{con} as a function of K (Thick lines for analytic results, and thin lines for numerical results). a) $\gamma > 0$ case with $T_0 = 100$ and $h = 10^{-1}$; b) $\gamma < 0$ case, first solution with $T_0 = 100$ and $h = 10^{-2}$; c) $\gamma < 0$ case, second solution with $T_0 = 100$ and $h = 10^{-2}$.*

derived as

$$\begin{aligned}
\text{For } -\sinh^2\left(\frac{\lambda\pi}{4\omega}\right) < \Gamma(\mu,\alpha) \leq 0, \qquad & T'_{con} = T_{con}\frac{1}{1-\frac{4\omega}{\lambda\pi}\sinh^{-1}\sqrt{-\Gamma(\mu,\alpha)}}\,, \\
\text{For } 0 < \Gamma(\mu,\alpha) < 1, \qquad & T'_{con} = T_{con}\,, \\
\text{For } 1 \leq \Gamma(\mu,\alpha) < \cosh^2\left(\frac{\lambda\pi}{4\omega}\right), \qquad & T'_{con} = T_{con}\frac{1}{1-\frac{4\omega}{\lambda\pi}\cosh^{-1}\sqrt{\Gamma(\mu,\alpha)}}\,, \quad (62)
\end{aligned}$$

where T'_{con} is the new duration of control, and T_{con} is the former one defined by equation (59). Here, as K is increasing, $\Gamma(\mu,\alpha)$ is varying and it induces a modulation of T_{con}, mainly when $\Gamma(\mu,\alpha)$ is not between 0 and 1.

Deeper investigations can even permit to foresee the position of the peaks of these curves, that is, the K values for which T_{con} presents a local maximum. Effectively, the Floquet theory demonstrates that in first approximation, parametric resonance in the Mathieu equation arises when $\mu = n^2$, n being a positive integer. According to equation (33), the corresponding values for K are

$$K_n = n^2\omega^2 - \left(1 + \frac{3\gamma C_1^2}{2} - \frac{\lambda^2}{4}\right). \quad (63)$$

It is quite remarkable that integer values come into play for the determination of these maxima, even though we are achieving a continuous control. Nevertheless, it is important to note that other peaks may arise because of the parametric and nonlinear resonances we have neglected. Anyway, these K_n values naturally lead to a slower control (larger value of T_{con}), and the above analysis at least enables to avoid them.

1.7 Conclusion

In this chapter, we have made a general theoretical and numerical analysis of unidirectional chaos synchronization. We have proposed a new analytical technique based on Floquet theory, which enables to investigate the bifurcation between the states of synchronization, desynchronization and instability through a Strutt diagram interpretation. The theory has also been extended to the stability analysis of external feedback chaos control.

The next chapter will generalize the present theory to the case of an arbitrary number of coupled chaotic oscillators, and will enable us to have an interesting analytic insight into the problem of pattern formation in nonlinear lattices.

CHAPTER II

CLUSTER SYNCHRONIZATION, CORRELATED STATES AND SPATIOTEMPORAL CHAOS IN LATTICES OF NONLINEAR COUPLED OSCILLATORS

2.1 Introduction

The phenomenon of pattern formation in lattices of nonlinear coupled systems is the focus of this chapter.

We will first consider a low-dimensional ring of four oscillators to show how the Strutt Diagram formalism can enable to define within a geometrical framework the concepts of complete synchronization, cluster synchronization, correlated state, or spatiotemporal chaos. A local injection scheme will also be applied to study the behavior of a coupled system when it is forced to replicate the dynamics of an external master-oscillator.

The general N-oscillators model will subsequently be considered, and important issues like the numbering of the cluster will be addressed. At last, an extension to the thermodynamic limit ($N \to +\infty$) will be made, and a scaling law will be used to investigate the dynamics of the lattice when the number of oscillators becomes significantly high.

2.2 Particular case of low-dimensional systems

2.2.1 Nonlinear dynamics and bifurcation behavior

In this sub-section, we consider a shift-invariant set of four diffusely coupled SWDOs and we aim to use the Strutt diagram technique to identify the various dynamical states of the system, as well as the various bifurcations amongst them.

The evolution equations of the ring can be written as

$$\ddot{x_k} + \lambda \dot{x_k} + x_k + \gamma x_k^3 = F\cos(\omega t) + K(x_{k+1} - 2x_k + x_{k-1}) \qquad k = 1, 2, 3, 4 \tag{64}$$

where k represents the instantaneous displacement of the k-th oscillator, and K plays the role of the diffusive coupling coefficient. The four state variables obey the shift-invariance condition $x_q \equiv x_{q+4}$, with $q \in \mathbf{N}$. Therefore, the stability of the resultant dynamical states can be studied through the linearization of the equation (64) around the states x_k according to

$$\ddot{\xi}_k + \lambda\dot{\xi}_k + (1 + 3\gamma x_k^2)\xi_k = K(\xi_{k+1} - 2\xi_k + \xi_{k-1}) \quad k = 1, 2, 3, 4\,. \tag{65}$$

Let us introduce the diagonal variables (or Fourier modes) ζ_s as

$$\begin{aligned} \zeta_0 &= \xi_1 + \xi_2 + \xi_3 + \xi_4, & \zeta_1 &= \xi_4 - \xi_2 = x_4 - x_2, \\ \zeta_2 &= \xi_4 - \xi_3 + \xi_2 = x_4 - x_3 + x_2 - x_1, & \zeta_3 &= \xi_3 + \xi_1 = x_3 - x_1. \end{aligned} \tag{66}$$

If we firstly replace the x_k variables by $\bar{x}$ (as for equations (28) and (31)) and secondly transform the ζ_s into new η_s variables (as for ξ and η in equations (33)), the coupled set (65) of variational equations can finally be rewritten under the form of independent canonical Mathieu equations similar to equation (32), that is

$$\frac{d^2\eta_s}{d\tau^2} + [\mu_s + 2\alpha\cos(2\tau - 2\varphi)]\ \eta_s = 0, \quad s = 0, 1, 2, 3\,. \tag{67}$$

with

$$\begin{aligned} \mu_0 &= \frac{1}{\omega^2}\left[1 + \frac{3}{2}\gamma C_1^2 - \frac{\lambda^2}{4}\right], \\ \mu_1 &= \mu_3 = \mu_0 + \frac{2K}{\omega^2}\,, \\ \mu_2 &= \mu_0 + \frac{4K}{\omega^2}\,. \end{aligned} \tag{68}$$

One more time, we can analyze through the Strutt the bifurcation behavior of the ring when the diffusive coupling parameter K is continuously increased from zero to infinity. For that purpose, we will focus on the $\gamma > 0$ case. When $K = 0$, the system is uncoupled and the Fourier modes , ζ_1, ζ_2 and ζ_3 degenerate into ζ_0. Therefore, the whole system is represented by a single point M_0 of coordinates (μ_0, α) in the Strutt diagram. It should be noticed that M_0 automatically belongs to the nonlinear stability area since the uncoupled system is chaotic. As K is increased, the modes ζ_1, ζ_2 and ζ_3 represented in the stability map by the related points M_s of coordinates (μ_s, α) independently begin to move from left to right along the straight horizontal line of equation $\alpha = const$ with a "velocity"

$$\nu_s = \frac{d\mu_s}{dK}\,, \qquad s = 0, 1, 2, 3\,. \tag{69}$$

It results that ζ_2 is the fastest mode with a velocity $\nu_2 = 4/\omega^2$, while the degenerated modes ζ_1 and ζ_3 are the slowest with $\nu_1 = \nu_3 = 2/\omega^2$. These "mobile" modes are called *transverse modes* because they decide the stability of perturbations transverse to the complete synchronization manifold. On the other hand, ζ_0 remains immobile in the Strutt diagram since $\nu_0 = 0$: it is the *longitudinal mode* describing the stability along the synchronization manifold.

When K is small, the three transverse modes points M_1, M_2 and M_3 remain in the vicinity of M_0, *i.e.*, in the nonlinear stability zone. Therefore, the corresponding perturbations have a non-zero finite time-average value: we are in the regime of **spatiotemporal chaos**.

When the fastest mode ζ_2 first reaches the linearly stable area, the ring satisfies the constraint

$$x_4 - x_3 + x_2 - x_1 \equiv 0\,, \tag{70}$$

while we still have

$$x_1 \not\equiv x_3, \qquad x_2 \not\equiv x_4 \tag{71}$$

since ζ_1 and ζ_3 remain in the nonlinear stability buffer zone. The ring is therefore in a **standard correlated state** (SCS). This intermediate state differs from spatiotemporal chaos because of the constraint (70), and also from complete synchronization because of equation (71).

If on the other hand M_2 re-enters the buffer zone while M_1 and M_3 have yet together penetrated into the linearly stable area, we have

$$x_4 - x_3 + x_2 - x_1 \not\equiv 0\,, \tag{72}$$

and

$$x_1 \equiv x_3, \qquad x_2 \equiv x_4\,. \tag{73}$$

This is sometimes referred to as **cluster synchronization**. Here, two clusters have emerged [eq. (73)] while there is no synchronization between them [eq. (72)].

Finally, when the three transverse modes points M_1, M_2 and M_3 are together in the linearly stable area, the ring is in the **complete synchronization state**

$$x_4 \equiv x_3 \equiv x_2 \equiv x_1\,, \tag{74}$$

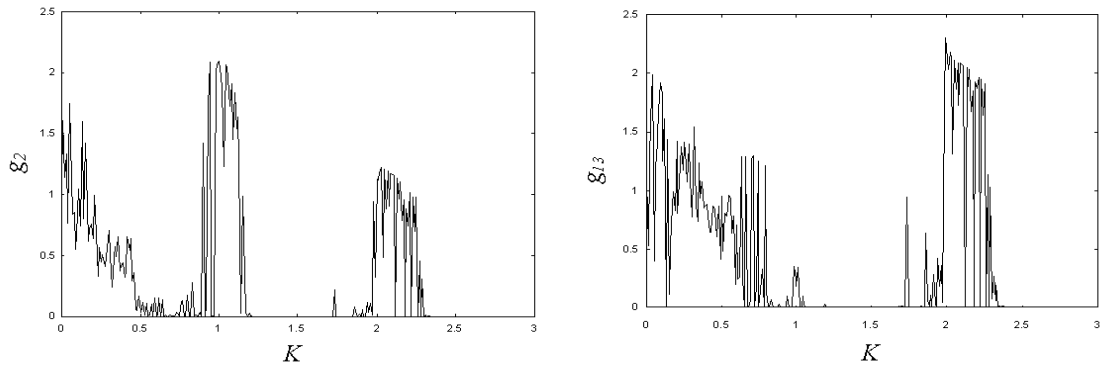

Figure 7: *Variations of g_2 and g_{13} as a function of K. a) Variations of g_2; b) Variations of g_{13}.*

corresponding to the simultaneous fulfillment of both equations (70) and (73). In that case, all the oscillators display the same dynamics.

Numerical simulations confirm the bifurcation mechanism deduced from the Strutt diagram analysis. Let us consider the following two functions of the state variables

$$g_2 = \langle |x_4 - x_3 + x_2 - x_1| \rangle, \qquad g_{13} = \langle |x_4 - x_2| + |x_3 - x_1| \rangle \,, \tag{75}$$

where the brackets $\langle\,\rangle$ stand for the time-averaging. g_2 represents ζ_2 on the one hand while g_{13} represents both ζ_1 and ζ_3 on the other. These functions will be equal to zero if the corresponding transverse modes points are in the linearly stable area of the Strutt diagram, and different to zero if they are in the buffer zone.

On figures 7a and 7b, the variations of g_2 and g_{13} are represented as a function of K. Effectively, for low K values, the ring is in the spatiotemporal chaos regime since $g_2 \neq 0$ and $g_{13} \neq 0$. When K reaches 0.70, g_2 first vanishes because the fastest mode point M_2 enters the linear stability area: it is the Standard Correlated State. This is also witnessed when K is between 2.30 and 2.35 ($g_2 = 0$ and $g_{13} \neq 0$). On the other hand, when $g_2 \neq 0$ and $g_{13} = 0$ like in the case $1.05 < K < 1.20$, we have a cluster synchronization state. Finally, complete synchronization ($g_2 = g_{13} = 0$) occurs between 1.20 and 1.70, and also when $K > 2.35$. It is important to note that the transitions between these dynamical states are never sharp. Moreover, unstable invariant sets embedded within the chaotic attractor can perturb the stability of the Fourier modes, like for $K \approx 1.00$ or $K \approx 1.75$.

2.2.2 Generalized correlated states in lattices with local injection

The modelized system or its potential utilization sometimes requires to couple a lattice to an external independent oscillator. This is commonly achieved through the local injection technique consisting of a unidirectional coupling between the external command oscillator and a fixed representative of the nonlinear coupled system [66]. This local injection scheme is indispensable for the description of undesirable parasite couplings or external perturbations. On the other hand, local injection can also be willingly introduced to force the nonlinear system to replicate the dynamics of the external master oscillator. For example, it is known that initially chaotic oscillators can lock into a (multi-)periodic state when they are mutually coupled [21]. The local injection method can in that case enable to recover the chaotic dynamics when the unidirectional command coupling is suitably designed. Still considering our four-oscillators ring, the evolution equations of the locally injected lattice can be obtained by modifying equation (64) following

$$\begin{aligned} &\ddot{x_k} + \lambda \dot{x_k} + x_k + \gamma x_k^3 = F\cos(\omega t) + K(x_{k+1} - 2x_k + x_{k-1}) + G(x_{inj} - x_1)\cdot\delta_{k,1}\ , \\ &\quad k = 1,2,3,4 \end{aligned} \tag{76}$$

where x_{inj} represents the dynamics of the external oscillator and plays the role of a command signal, while $\delta_{k,1}$ is the Kronecker symbol emphasizing that x_{inj} is only coupled to x_1 with the coupling strength G. Throughout our study we take x_{inj} as the chaotic oscillation of a SWDO identical to the uncoupled items of the ring, and we aim to analyze the influence of the local injection on the dynamics of the nonlinear coupled system. More precisely, our objective is first to identify the various dynamical states of the ring depending on K, and secondly to study the modifications induced by the local injection coupling.

When G is taken into account, the first order perturbation equations can be written as

$$\ddot{\xi_k} + \lambda\dot{\xi_k} + (1 + 3\gamma x_k^2)\xi_k = K(\xi_{k+1} - 2\xi_k + \xi_{k-1}) - G\xi_1\cdot\delta_{k,1}\,, \quad k = 1,2,3,4\,, \tag{77}$$

with $\xi_k = x_k - x_{inj}$. From these equations, we can determine the velocities ν_k of the corresponding figurative points in the Strutt Diagram according to

$$\Upsilon^4 + \left(\frac{G}{K}\right)\Upsilon^3 - 4\Upsilon^2 - 2\left(\frac{G}{K}\right)\Upsilon = 0 \quad \text{with} \quad \Upsilon = 2 - \omega^2\nu\,. \tag{78}$$

Figure 8 shows the numerical solutions of equation (78) obtained with the Newton-Raphson algorithm when the ratio G/K is increased. It can be noticed that when $G =$

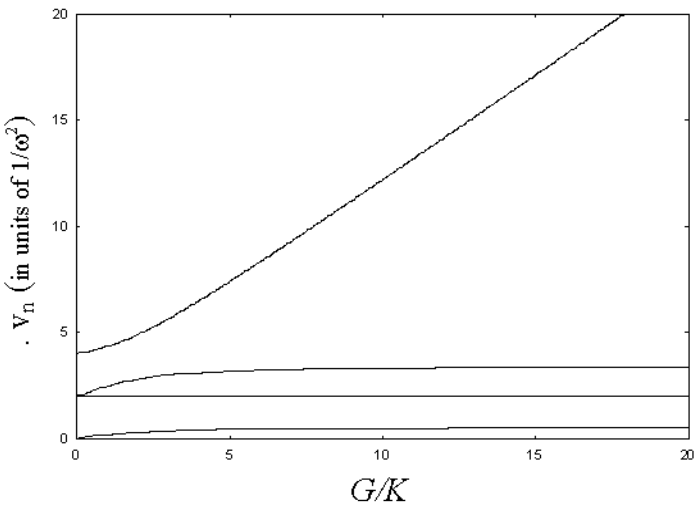

Figure 8: *Variations of the velocities v_n (in units of $1/\omega^2$) for the Fourier modes when the ratio G/K is increased. The curves are crescently ordered, v_1 being the lowest one and v_4 the highest.*

0, we have three non-degenerated modes, as we have demonstrated in the precedent sub-section. But as soon as $G \neq 0$, the degeneracy of the second mode is destroyed so that four non-degenerated modes now appear, and the slowest one discontinuously passes from $\nu_{2,3} = 2/\omega^2$ to $\nu_1 = 0^+$. Moreover, it appears that ν_4 indefinitely increases to infinity, while the second mode keeps a constant velocity . Each of these non-degenerated modes have been schematically represented in the Strutt diagram in figure 9 by crosses of coordinates (μ_k, α), with $\mu_k = \mu_0 + \nu_k K$ and

$$\begin{aligned} \nu_1 &= \frac{\epsilon_1}{\omega^2}, \qquad \nu_2 = \frac{2}{\omega^2}, \\ \nu_3 &= \frac{2+\epsilon_3}{\omega^2}, \qquad \nu_4 = \frac{4+\epsilon_4}{\omega^2}. \end{aligned} \tag{79}$$

The velocities ν_k have been explicitly written to define the detuning functions ϵ_k which are obviously equal to 0 when $G = 0$. However, ν_1 and ν_3 asymptotically converge to the limit values $\epsilon_1^\infty/\omega^2$ with $\epsilon_1^\infty = 0.585$ and $(\epsilon_3^\infty + 2)/\omega^2$ with $\epsilon_3^\infty = 1.414$, respectively when $G \to +\infty$.

The determination of the dynamical state of the ring now depends on the distribution of the four non-degenerated Fourier modes between the various areas of the Strutt diagram. Reasoning as we did for $G \equiv 0$ (no local injection), we find that spatiotemporal chaos and complete synchronization occur in the injected ring under

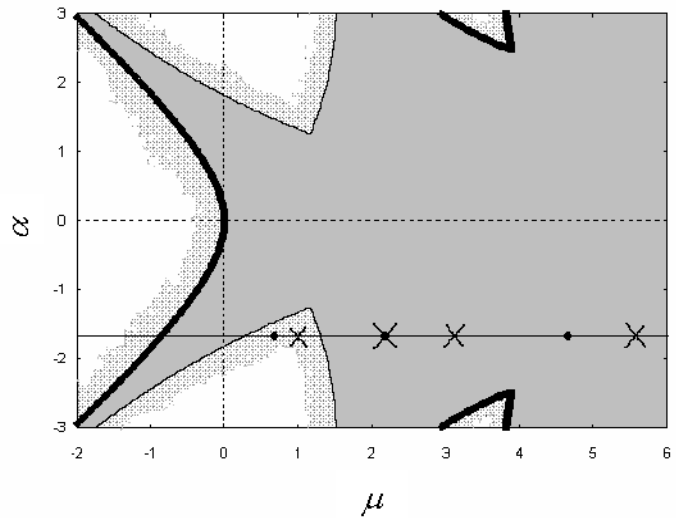

Figure 9: *Strutt diagram for dynamical states in a four-oscillators ring. An arbitrary distribution of non-degenerated spatial Fourier modes has been represented for $G = 0$ (points) and for $G \neq 0$ (crosses).*

the same topological conditions. However, cluster synchronization and standard correlation are no more possible when $G \neq 0$. Effectively, when the non-degenerated Fourier modes are simultaneously spread between the linear and nonlinear stability areas, the dynamical variables fulfill nontrivial constraints of the kind

$$\sum_{k=1}^{4} Q_k \cdot (x_k - x_{inj}) = 0\,. \tag{80}$$

Here, the coefficients Q_k are complicated functions of G and K. By opposition to the standard correlated state where the Q_k would have simply been equal to 0, 1 or -1, this new state induced by the local injection is referred to as **generalized correlated state** (GCS).

The transition boundaries between the spatiotemporal chaos, GCS, and complete synchronization states are mainly influenced both by G and K. Let us for example focus on the *first* bifurcation (from spatiotemporal chaos to GCS) and on the *last* one (from GCS to complete synchronization) as K is increased with a fixed G. The corresponding critical transition values for $G = 0$ have yet been determined numerically a former section as $K_f(0) = 0.70$ and $K_l(0) = 2.35$. They can be used to deduce analytically the transition values $K_f(G)$ and $K_l(G)$ for any non-zero G value. Note that for $G \neq 0$ we should have spatiotemporal chaos for $K < K_f(G)$, complete synchronization for $K > K_l(G)$ and GCS when $K_f(G) < K < K_l(G)$.

In fact, the first GCS emerges when the fastest mode point M_4 enters into the linear stability area of the Strutt diagram. From equation (79), we can deduce than

$$\int_{\mu_0}^{\mu_{cr,f}} d\mu_4 = \int_0^{K_f(0)} \frac{4}{\omega^2}\, dK = \int_{0^+}^{K_f(G)} \frac{1}{\omega^2} \left[4 + \epsilon_4 \left(\frac{G}{K}\right)\right] dK\,, \tag{81}$$

that is

$$\int_{0^+}^{K_f(G)} \epsilon_4 \left(\frac{G}{K}\right) dK = 4\left[K_f(0) - K_f(G)\right], \tag{82}$$

where $\mu_{cr,f}$ is the first critical Hopf boundary value encountered as μ is increased. Since the integrand function is positive, one can straightforwardly deduce that $K_f(G) \leq K_f(0)$. Hence, the ring emerges more rapidly from spatiotemporal chaos when G is greater. However, $K_f(G)$ can not be expressed explicitly because ϵ_4 has not been determined analytically.

On the other hand, if we consider the boundary transition from the last GCS to the complete chaotic synchronization state, we obtain

$$\int_{\mu_0}^{\mu_{cr,l}} d\mu_1 = \int_0^{K_l(0)} \frac{2}{\omega^2}\, dK = \int_{0^+}^{K_l(G)} \frac{1}{\omega^2} \epsilon_1 \left(\frac{G}{K}\right) dK\,, \tag{83}$$

so that

$$\int_{0^+}^{K_l(G)} \epsilon_1 \left(\frac{G}{K}\right) dK = 2K_l(0)\,, \tag{84}$$

where $\mu_{cr,l}$ is the last critical Hopf boundary value encountered as μ is increased. It consequently appears that $K_l(G \to +\infty) \approx 2K_l(0)/\epsilon_1^{\infty}$.

The critical boundary curves $K_f(G)$ and $K_l(G)$ have been plotted in figure 10. They divide the parametric plane into three areas: the lower zone corresponds to spatiotemporal chaos, the intermediate one to the GCS and the uppermost to the complete synchronization. However, the curve $K_f(G)$ remains difficult to distinguish in the figure, since it rapidly vanishes to 0. Therefore, the lower zone of spatiotemporal chaos does almost not appear on the map. On the same figure, the results of the numerical simulation for $K_l(G)$ has also been represented. They show a qualitative concordance with the analytic results of equation (84). One can note the discontinuity at $G = 0$ for the curve, due to the drop to 0^+ of the slowest velocity when the local injection is set on. This implies that small G values (case corresponding to undesirable external perturbations) irreversibly destroy the complete synchronization state since the threshold value jumps from a finite value to infinity. However, it appears that the boundary curves rapidly converge to their asymptotes, so that it is not necessary to use high G values to obtain a satisfying synchronization.

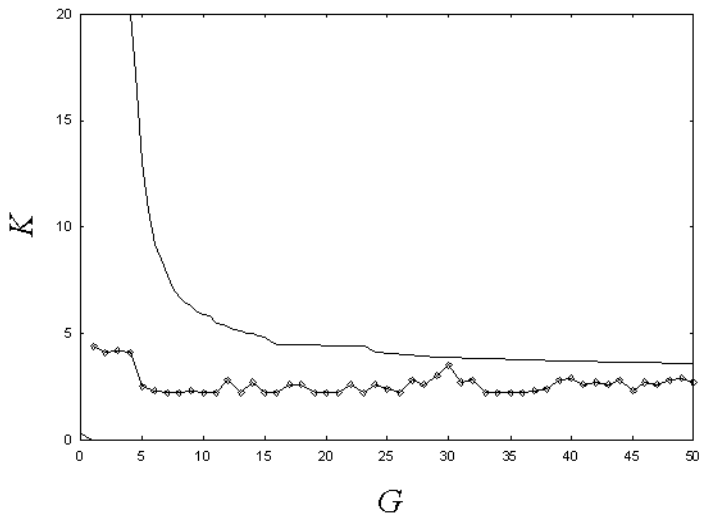

Figure 10: *Transition boundaries from GCS to complete synchronization. The analytical results are shown in full line, and the numerical results are represented by squares linked by a continuous line.*

2.3 Generalization to the N-oscillators system

When an arbitrary number of oscillators is considered (with the same type of nearest-neighbor diffusive coupling), the dynamics of the lattice is described by a set of equations similar to equation (64), with k varying from 1 to N. Accordingly, the shift-invariance condition and the perturbation equations remain the same, the number of oscillators being however set to N instead of 4. To perform the stability analysis, the linear perturbation equations (in ξ_k) have to be uncoupled through a Fourier transform diagonalization to the ζ_s variables [16, 17], whose η_s counterpart in the Mathieu equations also obey to equation (67) with the following eigenfrequency spectrum

$$\mu_s = \frac{1}{\omega^2}\left[1 + \frac{3}{2}\gamma C_1^2 - \frac{\lambda^2}{4} + 4K\sin^2\left(\frac{\pi s}{N}\right)\right] = \mu_0 + \frac{4K}{\omega^2}\sin^2\left(\frac{\pi s}{N}\right), \quad s = 0, ..., N-1\,. \tag{85}$$

Once again, μ_s is still independent of s, N and K at the contrary of α. From Floquet theory, it therefore results that each mode s is linearly stable if $\Gamma(\mu, \alpha)$ fulfills the double-inequality (44), nonlinearly stable is it rather fulfills the inequality (45), and naturally unstable if it does not satisfy any of these stability conditions.

The bifurcation mechanism of this N-oscillators lattice is qualitatively the same as the one of the case $N = 4$, which has yet been studied. As K is increased, the $N-1$ transverse Fourier modes points M_s independently spread along the $\alpha = const$

straight horizontal line with a velocity

$$\nu_s = \frac{4}{\omega^2} \sin^2 \left(\frac{\pi s}{N} \right), \quad s = 0, ..., N-1 \,. \tag{86}$$

Hence, depending on N and K, the points M_s are distributed between the three different areas of the Strutt diagram. Therefore, four distinct sets of mode distributions, which are unambiguously equivalent to the four different dynamical states of the ring can be distinguished. In the first case, at least one transverse mode is in the instability area, and consequently the whole coupled system is *unstable*, that is, the state variables x_k indefinitely grow to infinity. For the second case, all the transverse modes are within the area of nonlinear stability: it corresponds to the regime of *spatiotemporal chaos*. For the third case, certain transverse modes are in the area of linear stability while all the others are in the zone of nonlinear stability: it is the regime of *cluster synchronization* or of *standard correlation* (these eventualities are exclusive). At last, the fourth case corresponds to a situation when all the transverse modes are linearly stable, and in that case, the ring is in the *complete synchronization* state. It appears that the principal advantage of reasoning through the Strutt diagram is that increasing the number of oscillators does not require to sketch different stability maps, but just to conveniently add supplementary transverse modes on the same diagram, and to identify the related mode-distribution.

In figure 11, five non-degenerated Fourier modes have been represented on an horizontal line. The left-most point represents the longitudinal mode ($s = 0$) while the remaining four ones are transverse modes ($s \neq 0$). Consequently, the mode-distribution of the figure corresponds to a cluster synchronization state. Note that some of the inner-most points can represent two transverse Fourier modes each, *i.e.*, be double-degenerated. It appears from the above analysis that cluster synchronization and standard correlation states are the result of the distribution of the transverse modes between the linear and nonlinear stability areas of the Strutt diagram. Consequently, knowing that the number of non-degenerated transverse modes is $N/2$ if N is even and $(N-1)/2$ if N is odd, we can deduce that the number $\aleph$ of possible clusters and standard correlation states is

$$\aleph = \begin{cases} 2^{\frac{N}{2}} - 2 & \text{if } N \text{ is even} \\ 2^{\frac{N-1}{2}} - 2 & \text{if } N \text{ is odd} \end{cases}, \qquad N \geq 2 \,. \tag{87}$$

The two configurations that have been subtracted in equation (87) correspond to the spatiotemporal chaos and complete synchronization states. Nevertheless, it is

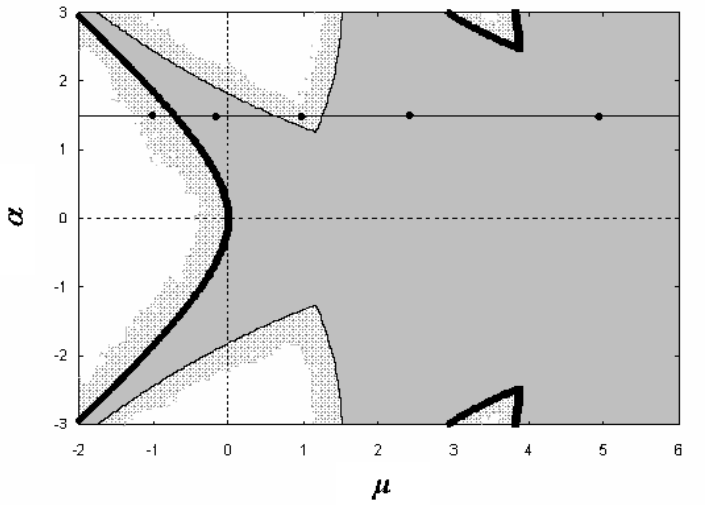

Figure 11: *Representation of a mode distribution in the Strutt diagram. The left-most mode is the longitudinal one, and all the remaining ones are transverse. This mode distribution corresponds to a cluster synchronization state or to a standard correlation state.*

important to notice that they mathematically correspond to a N-cluster and to a one-cluster respectively.

For small values of N, the following results are obtained. When $N = 2$ or $N = 3$, clustering is obviously impossible: we have either spatiotemporal chaos (*ab* and *abc* states) or a completely synchronous motion (*aa* and *aaa*). For $N = 4$, two cluster-states are foreseen by equation (87); anyway, symmetry considerations only allow the *abab* state to exist, but not *aabb*, which is replaced by a SCS. The same symmetry reasoning applies for $N = 5$ as well. The case $N = 6$ has been intensively studied by Zhang and co-workers for Rössler oscillators [19]. Five different cluster patterns have been observed (while $\aleph = 6$), since the shift-invariance symmetry does not allow the sixth state *aaabbb* to exist (also replaced by a SCS). The mode distribution of figure 11 can correspond to a ring of 8 or 9 oscillators.

When N is further increased, the number of possible clusters and SCS grows exponentially according to equation (87). Anyway, it should be stressed that some of these clusters and SCS are not or scarcely observed during numerical simulations or in practice. Two main reasons can explain that. The first reason is that some clusters are very weakly stable, so that they rapidly degenerate into compatible clusters of higher symmetry (*i.e.* less complicated and more stable patterns). This explains why for a given K, it is sometimes possible to obtain many different clusters depending on

the initial conditions [19]. The second reason is that for a fixed number of oscillators N, it may be impossible to witness a given-cluster state because the transverse modes do never fit with the related mode-distribution in the Strutt diagram, whatever the value of K is. Consequently, since equation (87) does not take into account these restrictions, $\aleph$ can just be considered as an order of magnitude. However, one can expect that this quantitative estimation may be useful for the statistical approach of the model in the thermodynamic limit.

2.4 Extension to the thermodynamic limit ($N \to +\infty$)

Let us now focus on some of the corollaries of the above theoretical stability analysis for the specific cases of a positive and of a negative nonlinear stiffness coefficient respectively when N is indefinitely increased to infinity. As we have earlier noticed, the number of clusters and SCS (which in a large sense are also clusters) is low when rings of only few oscillators are concerned. For these cases, numerical simulation can be performed to study each cluster state as well as the transitions amongst them, as we have done for the case $N = 4$. However, this approach does not hold anymore when N is significantly increased, since it becomes quite complicated to identify the various clusters. Moreover, these clusters become less interesting as individuals when N is high.

The appropriate approach in this case is to identify in the parametric plane N-K the areas corresponding to each of the four dynamical states of the ring. A scaling law is generally used for that purpose [67, 68], and we hereafter proceed in that way to derive the stability pattern of the N-oscillator system from the stability pattern of the two-oscillators model. The potential interest of such a scaling-law is high in the thermodynamic limit: it means that the dynamical states and the phase transitions of a one-dimensional lattice model can be deduced from the experimental or theoretical data obtained through the study of the two-oscillators model interactions.

Let us first consider the $\gamma > 0$ case. For $N = 2$, numerical simulations show that the coupled system is non-synchronized when $K \leq K_{b1}(2) = 0.34$, and synchronized for $K \geq K_{b2}(2) = 1.15$. One should notice that these numerical values differ from those of the first chapter were the coupling was unidirectional (and not bidirectional as it is the case here). For $K_{b1}(2) < K < K_{b2}(2)$, intervals of synchronized and

non-synchronized behavior are intermingled. This may easily be understood from the Strutt diagram interpretation. For a two-oscillator system, there is a single transverse mode moving along the $\alpha = const$ straight horizontal line. Its representative point M_1 starts from a nonlinear stability area, and then alternatively passes through linear and nonlinear stability zones. Finally, this point remains in the last semi-infinite segment laying within the linear stability region, leading to synchronous motion.

For $N > 2$, the number of transverse modes becomes greater and the fastest of them has a velocity

$$\nu_{fast} = \begin{cases} \frac{4}{\omega^2} & \text{if } N \text{ is even} \\ \frac{4}{\omega^2} \sin^2\left(\frac{N-1}{2N}\pi\right) & \text{if } N \text{ is odd} \end{cases}, \qquad N \geq 2\,, \tag{88}$$

while the slowest has a velocity

$$\nu_{slow} = \frac{4}{\omega^2} \sin^2\left(\frac{\pi}{N}\right) \qquad N \geq 2\,. \tag{89}$$

We can deduce from the stability analysis that when K is (very) low, all the transverse modes points M_s are spread within the initial nonlinear stability area, and therefore the ring displays a spatiotemporal chaotic dynamics. As soon as the fastest transverse mode point M_{fast} oversteps its first Hopf periodic boundary, the ring enters into the clustering regime and when the slowest mode M_{slow} oversteps its last Hopf periodic boundary, the coupled system becomes completely synchronized. The consequence of this transition mechanism is that it is impossible for the ring to become unstable, whatever the values of K and N are (it is assumed that $K > 0$). In fact, this may be explained by a high $\bar{\Lambda}$ value.

Mathematically, if we define

$$K_{b1}(N) = \begin{cases} K_{b1}(2) & \text{if } N \text{ is even} \\ \frac{K_{b1}(2)}{\sin^2\left(\frac{N-1}{2N}\pi\right)} & \text{if } N \text{ is odd} \end{cases}, \qquad N \geq 2\,, \tag{90}$$

and

$$K_{b2}(N) = \frac{K_{b2}(2)}{\sin^2\left(\frac{\pi}{N}\right)} \approx \frac{K_{b2}(2)}{\pi^2} N^2, \text{ when } N \gg 2\,. \tag{91}$$

It appears that the system is in the spatiotemporal regime if $K \leq K_{b1}(N)$, in the completely synchronous state if $K \geq K_{b2}(N)$, and in the clustering regime when $K_{b1}(N) < K < K_{b2}(N)$. Hence, according to the scaling laws (90) and (91), the width $[K_{b2}(N) - K_{b1}(N)]$ of the clustering interval broadens in a square power-like fashion as N tends to infinity. The parametric plane N-K is therefore divided into

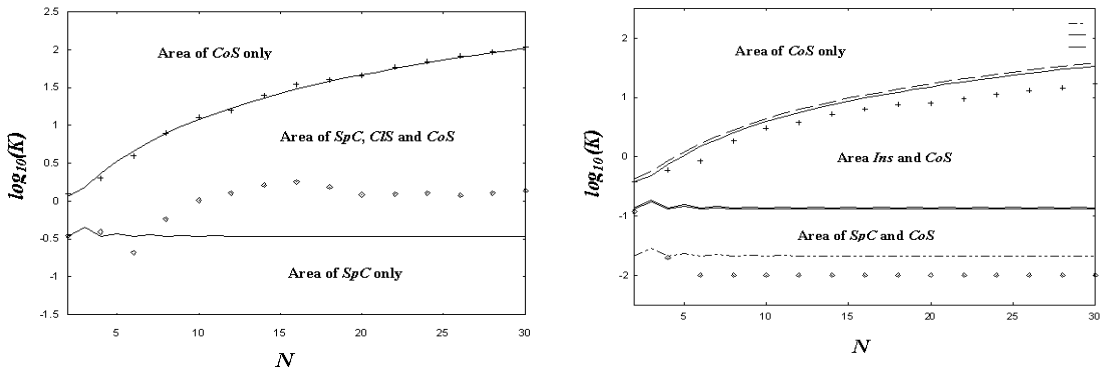

Figure 12: *Boundaries between the different dynamical states of the lattice. The analytical and semi-analytical results are denoted by solid lines, while the numerical results are represented by squares and crosses. SpC stands for* Spatiotemporal Chaos*, CoS for* Complete Synchronization*, ClS for* Cluster Synchronization*, and Ins for* Instability*. Note that for the numerical comparison, drifts and deviations are accentuated by the logarithmic scale. a)* $\gamma > 0$ *case; b)* $\gamma < 0$ *case.*

three areas, as displayed in the semi-logarithmic diagram of figure 12a. Typically, we have spatiotemporal chaos for low K, cluster synchronization for intermediate values, and finally complete synchronization when K is high enough. One should anyway note that degenerated full synchronization states can also be observed in the cluster area, depending on the initial conditions and on the number of oscillators.

The numerical simulations confirm the above analysis. If for example we focus on the transition from the cluster to the completely synchronous states, we can notice the excellent coincidence between the numerical and the semi-analytical curves on figure 12a. This good concordance is due to the fact that $K_{b2}(2)$ has been determined numerically (that is why we refer to this comparison as a semi-analytical one). A purely analytical comparison would require the analytic determination of $K_{b2}(2)$. This is difficult to achieve here because the amplitude of the corresponding UPO and its related α are so high that approximated or perturbation methods do not apply. Hence, for an analytic derivation of $K_{b2}(2)$, it would be indispensable to compute the Hill determinant $\Delta(0, \mu, \alpha)$ at a high order of truncation (≥ 18), or alternatively to use the Mathieu special functions. However, the purely analytic comparison would have presented a little discrepancy with the numerical results because the uniperiodic approximation does not qualitatively fit with the pseudo double-well configuration of the phase portrait of figure 1a. If we now focus on the transition from spatiotemporal chaos to cluster synchronization, we can notice on figure 12a the rather good qualitative concordance between semi-analytical and numerical results. In fact, since the

uniperiodic approximation in the analytic stability analysis does not dynamically take into account the complex spatial patterns of spatiotemporal chaos and cluster synchronization states, the bifurcation boundary $K_{b1}(N)$ is not as accurate as $K_{b2}(N)$, even though $K_{b1}(2)$ is also determined numerically. Nevertheless, its interest remains at least qualitative, since it however predicts that the bifurcation values leading to the emergence of ordering from spatiotemporal chaos are roughly independent of N. It is also important to notice that the good concordance of our semi-analytical comparison proves that as we have earlier postulated, the spectral properties of the coupled oscillators do not drastically differ from those of the corresponding uncoupled items.

For the $\gamma < 0$ case, numerical simulations also confirm the theoretical analysis. When $N = 2$, one can numerically observe a synchronous motion when $K \leq K_{b1}(2) \approx 0.13$, and when $K \geq K_{b2}(2) \approx 0.37$. The crucial parameters $K_{b1}(2)$ and $K_{b2}(2)$ can here be determined analytically, thereby permitting a purely analytical comparison beside a semi-analytical one. Effectively, the C_1 values in the $\gamma < 0$ case are low enough to enable an approximated analytical determination of both $K_{b1}(2)$ and $K_{b2}(2)$. At the first order approximation, the two branches of the 2π-periodic boundaries around $\mu = 1$ can be derived as $\mu = 1 \pm \alpha$, so that so that for the outer chaotic trajectory (corresponding to $C_1 = 0.864$ according to equation (56)), the bifurcation boundary values for $N = 2$ are

$$\begin{aligned} K_{b1}(2) &= \frac{1}{16}(\lambda^2 - 3\gamma C_1^2) = 0.138 \\ K_{b2}(2) &= \frac{1}{16}(\lambda^2 - 9\gamma C_1^2) = 0.416\,, \end{aligned} \tag{92}$$

which are in excellent concordance with the numerical values 0.13 and 0.37 respectively.

For the intermediate coupling strengths values (*i.e.*, between $K_{b1}(2)$ and $K_{b2}(2)$, intervals of instability and of complete synchronization are intermingled. Here, the transitions can not be well determined because they depend on the initial conditions. Effectively, the multistability is so predominant in the $\gamma < 0$ case that stable motion is witnessed only when the initial conditions of all the oscillators are gathered within a small region of the ring state space. From a Strutt diagram interpretation, we can say that the average width $\overline{\Lambda}$ is so thin that the nonlinear stability buffer zone is almost exclusively fractal-like. Therefore, one can straightforwardly deduce that clustering is practically impossible when $\gamma < 0$ for the chosen parameters, as well as spatiotemporal chaos independently of K and N. Consequently, the coupled system is

generally either unstable or completely synchronous, excepted for very low K values, for which spatiotemporal chaos can be observed. Anyway, the fastest and the slowest transverse modes are expressed as for the $\gamma > 0$ case, so that the same scaling-law reasoning applies. Hence, if we define $K_{b1}(N)$ and $K_{b2}(N)$ as in eqs. (90) and (91), respectively, we can also divide the N-K plane into a upper zone of synchronous motion, an intermediate zone of inextricably intermingled stable and unstable areas, and a lower zone of complete synchronization and spatiotemporal chaos. Naturally, the uncertainty on $K_{b1}(2)$ and $K_{b2}(2)$ induces an error when evaluating $K_{b1}(N)$ and $K_{b2}(N)$, but the square-power broadening behavior is preserved however, and the scaling-law remains at least of qualitative interest. On figure 12b, the uppermost double-line stands for both the analytical and semi-analytical results, and they indicate the bifurcation boundary to the completely synchronous state. These two solid lines are very near one each other because of the excellent concordance between the numerical and analytical values of $K_{b2}(2)$ which has been earlier demonstrated. However, a deviation from the numerical simulation is noticed due to the bistability of the system. Effectively, a quasi-perfect coincidence is observed until $N = 6$, but beyond, the ring locks into the inner limit-cycle so that the $K_{b2}(N)$ values should be calculated now with $C_1 = 0.343$, and probably around another resonance value $\mu = n^2$, n being an integer greater than 1. The same comment can be made for the bifurcation from spatiotemporal chaos to instability. The intermediate double-line stands for the semi-analytical and analytical boundaries corresponding to the chaotic trajectory, and the single lower solid-line stands for the bifurcation boundary related to the inner limit-cycle. Once again, the numerical comparison rapidly switches from the chaotic boundary to the periodic one. Therefore, since in the $\gamma < 0$ case the spectral invariance condition is not fulfilled, several bifurcation boundary values do coexist. Consequently, depending on the number of oscillators and on the initial conditions, the ring's state variables will bifurcate around various boundary lines related to the different spectral groups.

2.5 Conclusion

We have addressed in this chapter the issue of pattern formation in a ring of coupled chaotic oscillators. A general theory has been developed for the understanding of the collective dynamics and bifurcation behavior of the system, and numerical simulations have been performed to confirm the analytic predictions.

The following chapter will enable us to use the results we have obtained to optimize and stabilize the synchronized dynamics of coupled semiconductor lasers in their chaotic regime.

CHAPTER III

DYNAMICS AND SYNCHRONIZATION OF CHAOTIC SEMICONDUCTOR LASERS

3.1 Introduction

In this chapter, we aim to analyze the dynamics and synchronization behavior of coupled semiconductor lasers operating in a chaotic regime.

We will first introduce the fundamental concepts of semiconductor lasers, and the semi-classical rate equations ruling their dynamics will be derived both in the complex field and intensity representations.

Then, we will focus on the dynamics and synchronization of these lasers in the chaotic regime. Two distinct methods will be used to induce chaos: The first one will rely on the ultra-high frequency modulation of the pumping-current while the second will rely on external optical feedback. In both cases, bifurcation scenarii will be investigated, and suitable coupling schemes will be designed to ensure their synchronization.

A particular emphasis will be laid upon the optimization and stability analysis of the related synchronization manifolds, and finally, the issue of detrimental effects induced by parameter mismatch will be addressed.

3.2 Semiconductor lasers

3.2.1 Laser operation in semiconductor junctions

Semiconductors are solids whose electrical and optical properties can be significantly modified by changing their temperature or their impurity content.

The energy levels in semiconductors are gathered into energy-bands, namely the *valence* and *conduction* bands, which are separated by a "forbidden" energy-gap of width E_g called the *bandgap energy*. It is known from statistical physics that the probability for an electron to occupy a given state of energy E in a semiconductor is

given by the *Fermi-Dirac distribution*

$$f(E) = \frac{1}{\exp[(E - E_f)/kT] + 1}\,, \tag{93}$$

where E_f is the *Fermi level*, which lies more or less in the middle of the bandgap between the valence and conduction bands. An electron can quantum-mechanically change its energy through an interaction with the lattice (electron-phonon interaction) or through an interaction with light (electron-photon interaction).

Light-matter interactions in semiconductors have a fundamentally quantum nature, and are intimately related to the three basic concepts of *absorption*, *spontaneous emission* and *stimulated emission*. The term *absorption* is used when a photon creates an electron-hole pair in the material, the term *spontaneous emission* is used when a photon is emitted after the spontaneous recombination of an electron and a hole, while the term *stimulated emission* is reserved for the case where an incoming photon forces the recombination of an electron-hole pair, thereby emitting a new photon perfectly correlated (in phase, direction and polarization) with the incoming one. Since they are both triggered by incoming photons, absorption and stimulated emission are correlated to the surrounding electromagnetic field: they are *coherent interactions*. On the other hand, spontaneous emission has a purely statistical nature and is not correlated with its environment: it is an *incoherent interaction*.

Let us now refer to the number of atoms per unit volume in some given level (band) as the *population* of that level (band), and let us consider n_{coh} as the density of coherent photons resulting from absorption and stimulated emission between some energy levels E_1 and E_2 belonging to the valence and conduction bands respectively. It can be deduced from quantum mechanics that the variation rate of n_{coh} obeys

$$\frac{dn_{coh}}{dt} = \Big\{\frac{\varrho(\nu)}{\tau_r}\frac{c^3}{8\pi\nu^2}[f(E_2) - f(E_1)]\Big\} \cdot n_{coh} = \gamma(\nu) \cdot n_{coh}\,. \tag{94}$$

Here, τ_r is the *electron-hole recombination lifetime*, that is, the average time taken by an electron of the valence conduction band before spontaneously recombine with a hole of the valence band. On the other hand, the *optical joint density of states* is

$$\varrho(\nu) = \frac{(2m_r)^{3/2}}{\pi\hbar^2}(h\nu - E_g)^{1/2} \tag{95}$$

where m_r is the *reduced mass* defined as $m_r = m_v m_c/(m_v + m_c)$, with m_v and m_c being the effective masses of holes and electrons in the valence and conduction bands respectively. The global term $\gamma(\nu)$ in eq. (94) can be considered as *the gain* of the

medium. Under the usual conditions of thermal equilibrium, this gain is negative because stimulated emission is strongly dominated by absorption: effectively, as indicated by the Fermi-Dirac distribution, there are more electrons in the valence band than in the conduction band, so that absorption of incoming photons is much more likely to happen than stimulated emission.

However, when the semiconductor is doped, the Fermi level moves downwards to the valence band (in case of a p-type doping) or upwards to the conduction band (for a n-type doping). Therefore, when a p-type and a n-type semiconductors are associated as a p-n junction, the energy-bands are "distorted" in the depletion layer because of the initial misalignment between the Fermi levels. If the junction is forward biased, or equivalently when there is a current injection in the depletion layer, the thermal equilibrium is destroyed and the Fermi level E_f splits into two "quasi-Fermi levels": the first one E_{fv} is associated to the Fermi-Dirac distribution f_v of the holes in the valence band, while the second one E_{fc} is associated with the Fermi-Dirac distribution f_c of the electrons in the conduction band. In this case, the gain in the p-n junction should be expressed as [69]

$$\gamma(\nu) = \frac{\varrho(\nu)}{\tau_r}\frac{c^3}{8\pi\nu^2}[f_c(E_2) - f_v(E_1)]\,, \tag{96}$$

where as we have earlier stated, f_v and f_c are the Fermi-Dirac distributions characterized by the quasi-Fermi levels E_{fv} and E_{fc}. When the p- and n-types doping is high enough such that E_{fv} and E_{fc} respectively lie well inside the valence and conduction bands, both the electrons and holes can have a large concentration around E_{fv} and E_{fc} in the depletion layer. As current injection is increased, the quasi-Fermi levels E_{fv} and E_{fc} (which have the same value E_f when there is no injection) begin to separate. When their mutual separation is high enough so that the double condition $E_g < h\nu < E_{fc} - E_{fv}$ is fulfilled, **the gain $\gamma(\nu)$ in the medium becomes positive** according to equation (96) as the stimulated emission becomes stronger than the absorption. Since in that case $dn_{coh}/dt > 0$, **this coherent light is continuously amplified**: in other words, we have a *"***L***ight* **A***mplification by* **S***timulated* **E***mission of* **R***adiations"*, that is, a (semiconductor) **LASER**.

Therefore, the role of the injection current, which in this context is referred to as the *pumping current*, is to create a *population inversion*, that is, an out-of-equilibrium state where there are more electrons in the conduction band than in the valence band: when such an inversion is achieved, the semiconductor laser emits a coherent radiation through stimulated electrons-hole recombination.

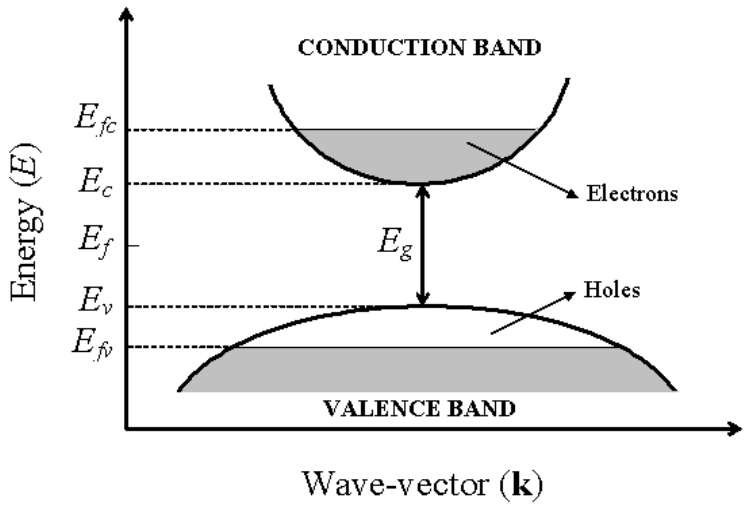

Figure 13: *E-**k** diagram of a semiconductor laser. This is a situation of sufficiently high pumping, where the double condition $E_{fc} > E_c$ and $E_{fv} < E_v$ is fulfilled. In that case, there is a high concentration of electrons in the conduction band, and a high concentration of holes in the valence band: it is the* population inversion*. Lasing with a frequency $\nu \simeq E_g/h$ therefore results from the stimulated recombination of these electrons and these holes.*

However, effective laser emission is possible only when the active medium is placed within an **optical resonator**. An optical resonator is a system that confines and stores light at certain fixed resonance frequencies. The simplest optical resonator is the Fabry-Pérot resonator, which consists of two parallel plane mirrors facing each other. In the hypothetical case of perfectly parallel and perfectly reflecting mirrors, light would repeatedly and endlessly be reflected in between. However, losses are unavoidable, and they are principally due to the attenuation of the light beam while traveling between the two mirrors, and also to the fact that the reflectance of these mirrors is never perfect. Therefore, if we consider α_r as the total loss of energy (or number of photons) per second, then

$$\tau_p = \frac{1}{\alpha_r} \tag{97}$$

would represent the *photon lifetime* in the resonator.

In semiconductor lasers, optical resonance is sometimes achieved in the most simplest way. Effectively, since the semiconductor material has a high refractive index ($n_{sem} \sim 3.5$) relatively to the air ($n_{air} \simeq 1$), external mirrors are not required since

the cleaved facets of the material can act as mirrors of reflectivity

$$R_{facet} = \left[\frac{n_{sem} - n_{air}}{n_{sem} + n_{air}}\right]^2 \sim 0.3\,. \tag{98}$$

Laser emission (or **lasing**) is therefore the consequence of the following scenario. Initially, a photon of frequency ν stimulates the emission of another identical one, and both of them trigger further stimulated emission of identical photons, and so on. As soon as they get out of the medium, they are reinjected back by the mirrors of the resonators, and they can thereby continue to stimulate the emission of more clone photons. Laser operation is therefore a kind of "avalanche" production of identical photons which fundamentally relies on the amplification in a medium where a population inversion has been achieved, and on the feedback from the mirrors of an optical resonator.

However, two fundamental conditions should be fulfilled for lasing to be effective [69, 70].

The gain condition requires that the gain of the active medium must be greater than the losses of the resonator to initiate the process, that is $\gamma(\nu) > \alpha_r$. This gain condition can enable us to determine the *threshold population inversion*, that is, the critical population inversion which overcomes the losses of the resonator and enables the lasing.

Secondly, **the phase condition** requires that the phase shift in a single round-trip must be a multiple of 2π, so that the phase of the photons in the active medium remain independent of the reflections through the mirrors of the resonator. This condition is approximately satisfied when the laser frequencies match the longitudinal and transversal eigenmodes of the resonator.

Any lasing frequency should absolutely satisfy the gain and phase conditions. If one of the mirrors of the resonator is partially transparent, a portion of the coherent light can be extracted and be used for various applications. These applications always rely on the fundamental properties of laser beams. The first of these properties is spatial and temporal **coherence**, and it is due to the fact that laser light proceeds from stimulated emission. This stimulated emission origin and the severe eigenmode selection of the optical resonator also explain the high **directionality** and **monochromaticity** of laser beams. This latter property is quantified by the *linewidth* of the laser light, that is, the narrow spectral range around the central frequency whose amplitude is significantly different from 0.

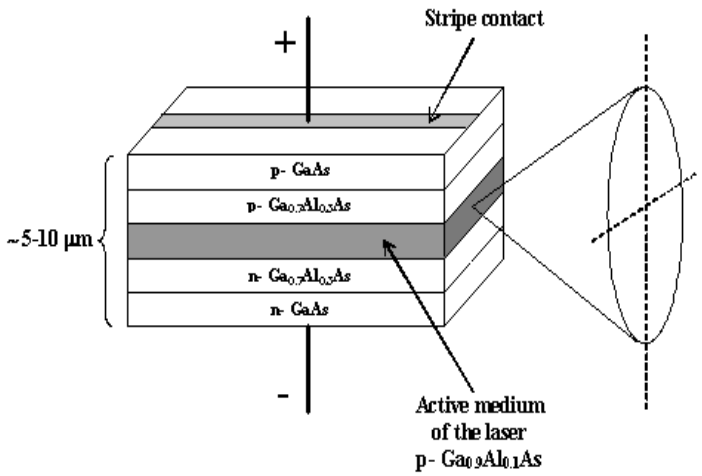

Figure 14: *Structure of an heterojunction semiconductor laser. The left and right vertical planes are the cleaved facets of the semiconductor crystal, and they serve at the same time as reflectors for optical resonance and coupler to enable the laser radiation to escape from the internal cavity.*

Figure 14 shows a simplified representation of an heterojunction semiconductor laser. One can note that it is a micrometric device (also sometimes referred to as *chip*) which can easily be incorporated within an optoelectronic integrated circuit.

3.2.2 Rate equations

Exact rate equations for semiconductor lasers should normally procede from the fundamental principles of quantum and statistical mechanics. However, this task is so inextricably complex that the laser rate equations are commonly derived in the literature on a semi-classical basis.

As we earlier pointed out, pumping is achieved in semiconductor lasers by current injection. Therefore, the *carrier density* N continuously increases with the pumping current intensity I. A first critical value N_0, referred to as the *carrier density at transparency*, is reached when the material gain in the depletion layer exactly reaches the value 0. As the pumping current is furthermore increased, the density of carriers reaches a second critical value N_{th}, which is the *carrier density at threshold*: above this value, the gain overcomes the losses and enables the lasing. If we introduce the parameter g as the *differential gain* of the laser, the following balance equation

between the material gain and the optical resonator losses should hold

$$g\,(N_{th} - N_0) = \frac{1}{\tau_p}\,. \tag{99}$$

If we consider $\mathcal{E}$ as the coherent complex electric field of amplitude $|\mathcal{E}|$ and phase ϕ resulting from the stimulated emission, then the optical power density which is proportional to the density of photons, can simply be expressed as $P = |\mathcal{E}|^2$. Logically, it is expected that P should increase or decrease accordingly to the sign and absolute value of the material gain $\gamma = g\,(N - N_{th})$ in the depletion layer. Within the approximation of a slowly-varying amplitude and a single-mode operation, the variation rate the optical power density should therefore read

$$\frac{dP}{dt} = g\,(N - N_{th})\,P = \left[g\,(N - N_0) - \frac{1}{\tau_p}\right]\,P\,. \tag{100}$$

On the other hand, the variation rate of the carrier should account for the electrons coming from the pumping, for their spontaneous decay to lower levels according to the *carrier lifetime* τ_s, and also for their stimulated decay which produces the coherent photon emission, accordingly to

$$\frac{dN}{dt} = I - \frac{N}{\tau_s} - g\,(N - N_0)\,P\,. \tag{101}$$

Hence, one can deduce from the above equation that the *threshold injection current density* necessary for laser emission is determined by $I_{th} = N_{th}/\tau_s$. Lasing is not possible under this threshold value, while above I_{th}, the optical output power emitted by the semiconductor initially increases linearly with I: that is why by analogy to a well-known electronic component, semiconductor lasers are sometimes referred to as **laser-diodes**.

However, some other parameters should phenomenologically be introduced in the rate equations (100) and (101) to take into account for some characteristic phenomena associated with the specific properties of semiconductor materials. The first one is the *gain saturation parameter* s, which accounts for the fact that the differential gain g should decrease as the optical power density P increases. This saturation phenomenon is quite universal in all types of amplifiers, independently of their nature. Therefore, better concordance with experience is achieved when g is replaced by $g\,(1+sP)^{-1}$. One should moreover take into account in the rate equations the incoherent photons proceeding from spontaneous emission whose characteristics incidentally coincide with those of the coherent photons. They induce in the laser intensity equation an additional term proportional to N/τ_s, so that the corresponding set of coupled

rate equations finally reads

$$\begin{aligned}\frac{dP}{dt} &= \left[\frac{g\,(N-N_0)}{1+sP} - \frac{1}{\tau_p}\right] P + \beta\,\frac{N}{\tau_s}\,,\\ \frac{dN}{dt} &= I - \frac{N}{\tau_s} - \frac{g\,(N-N_0)}{1+sP}\,P\,,\end{aligned} \tag{102}$$

where the proportionality coefficient β is the *spontaneous emission coefficient*.

In some situations, particularly when the dynamics of the phase ϕ is of particular importance, it is more convenient to write the rate equations in terms of the laser output electromagnetic field $\mathcal{E}$ and carrier density N. In that case, one should take into account the fact that the phase of the electric field is generally affected by the the carrier density during the propagation in the active medium. Hence, a coupling between N and ϕ should be accounted for in the rate equations, precisely by assuming a complex value for the material gain. The coupling constant α is commonly referred to as the *linewidth enhancement factor* because it is responsible for the broadening of the laser output linewidth.

Consequently, the modified coupled rate equations in terms of $\mathcal{E}$ and N can be deduced from equation (102) as

$$\begin{aligned}\frac{d\mathcal{E}}{dt} &= \frac{1+i\alpha}{2}\left[\frac{g\,(N-N_0)}{1+s\,|\mathcal{E}|^2} - \frac{1}{\tau_p}\right]\mathcal{E}\,,\\ \frac{dN}{dt} &= I - \frac{N}{\tau_s} - \frac{g\,(N-N_0)}{1+s\,|\mathcal{E}|^2}\,|\mathcal{E}|^2\,.\end{aligned} \tag{103}$$

One can note that the spontaneous emission term is absent in the field set of rate equations (103). In fact, they are never accounted for in the deterministic field representation because a convenient modeling would in that case require the introduction of a stochastic field fluctuation of mean-value 0, and we would end up with a *Stochastic Differential Equation* (SDE) instead of an ODE.

3.3 Dynamics and synchronization of semiconductor lasers with ultra-high frequency current modulation

3.3.1 Chaotic dynamics

As we have earlier noticed, the nonlinear intensity rate equations describing semiconductor lasers usually possess only two degrees of freedom, namely, the photon and

carrier densities. Hence, additional degrees of freedom should artificially be introduced for chaos to appear. A straightforward alternative is to generate chaos through the amplitude modulation of the injection current. This procedure creates a third degree of freedom in the autonomous representation and thereby enables the formation of a chaotic attractor [71, 72, 73, 74]. Taking into account the current modulation, the intensity rate equation can be written as

$$\begin{aligned}\frac{dP}{dt} &= \left[\frac{g\,(N-N_0)}{1+sP} - \frac{1}{\tau_p}\right] P + \beta\,\frac{N}{\tau_s}\,,\\ \frac{dN}{dt} &= \left[I_b + I_m \sin(2\pi f_m t)\right] - \frac{N}{\tau_s} - \frac{g\,(N-N_0)}{1+sP}\,P\,,\end{aligned} \tag{104}$$

where f_m is the modulation frequency while I_b and I_m are the bias and modulation currents respectively. For applications to optical communications, current modulation is generally performed with frequencies higher than 1 GHz, that is, in the ultra-high frequency range of the electromagnetic spectrum. A suitable normalization of equations (104) leads to the following dimensionless form (using the balance equation (99))

$$\begin{aligned}\dot{p} &= \left[\frac{(1+2n)}{1+\sigma p} - 1\right] p + \beta(n+\Phi),\\ \dot{n} &= \varepsilon\left[i_0(1+m\sin(\omega t)) - n - \frac{(1+2n)}{1+\sigma p}\,p\right]\end{aligned} \tag{105}$$

with the following rescalings

$$\begin{aligned}&p = \left(\frac{1}{2}g\tau_s\right) P, \quad n = \frac{1}{2}gN_{th}\tau_p\left(\frac{N}{N_{th}} - 1\right),\\ &\varepsilon = \frac{\tau_p}{\tau_s}, \quad \sigma = \frac{s}{g\tau_s/2}, \quad \Phi = \frac{1}{2}gN_{th}\tau_p,\\ &i_0 = \frac{1}{2}gN_{th}\tau_p\frac{I_b - I_{th}}{I_{th}}, \quad m = \frac{I_m}{I_b - I_{th}}, \quad \omega = 2\pi f_m \tau_p.\end{aligned} \tag{106}$$

The dots over p and n in equations (105) denote the derivative relatively to the reduced time (in units of τ_p). One should note that the dimensionless injection current $i(t)$ is now characterized by its time average amplitude i_0 and its modulation index m. The above system will therefore be referred to as an ultra-high frequency **Current-Modulated Semiconductor Laser** (CMSL).

For certain parameter values, the CMSL exhibits a chaotic behavior. Figure 15a displays the chaotic oscillations of the photon density p as a function of time. They are constituted of spikes with randomly distributed amplitudes, alternatively followed

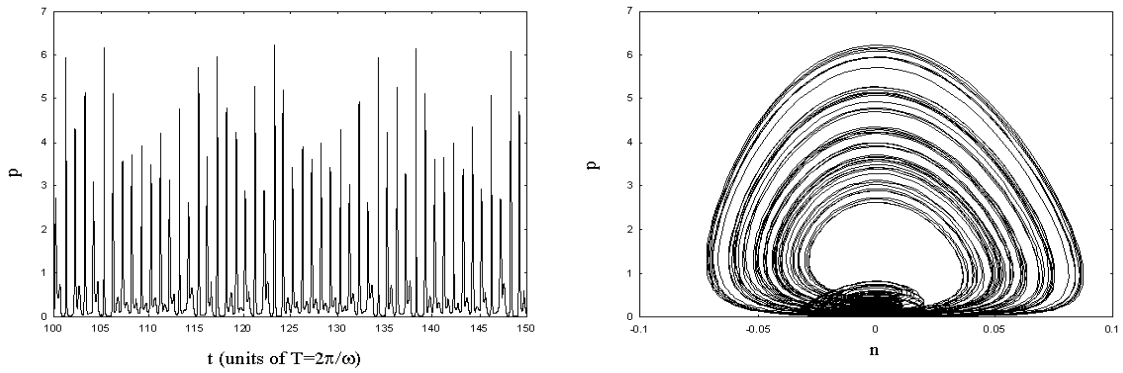

Figure 15: *Chaotic timetrace and attractor of a CMSL for $i_0 = 0.6$ and $m = 1.0$. a) Chaotic timetrace; b) Corresponding attractor.*

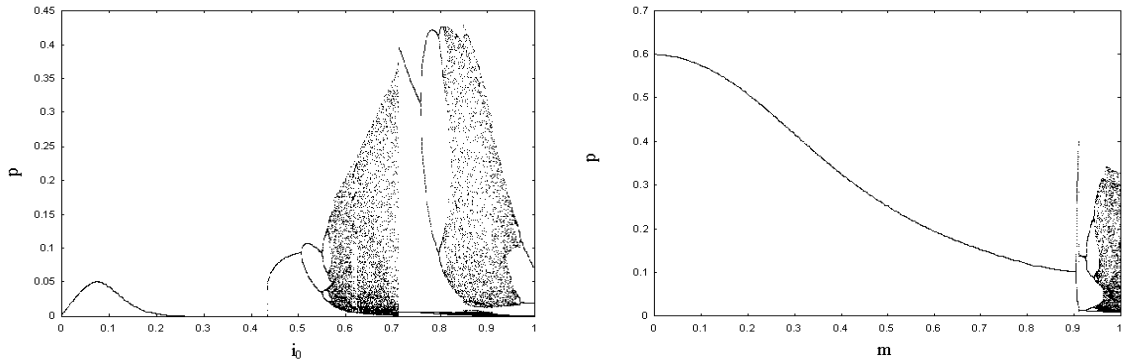

Figure 16: *Bifurcation diagrams for a CMSL. a) As a function of i_0 for $m = 1.0$; b) As a function of m for $i_0 = 0.6$.*

by irregular bursts of quite smaller amplitudes. This two-frequency structure is also foreshadowed in the phase plane of figure 15b, where one can see that the chaotic attractor intrinsically possesses the characteristic notch of double-periodic oscillations. It also appears on the bifurcation diagrams of figures 16a and 16b that chaos occurs when the CMSL is strongly excited, that is, for high i_0 or m. More precisely, chaos seems to be possible only when the modulation index approximately exceeds 0.95 . In both cases, the route to chaos is the period-doubling cascade of pitchfork bifurcations.

3.3.2 Optimization and stability analysis of chaos synchronization

The synchronization of CMSLs can be carried out with different methods. In this thesis, we will use a retroactive coupling scheme [25, 26], which can be explicitly

expressed in vectorial notation under the canonical form of equation (19). The state vector is $\mathbf{x} \equiv (p, n)$ in this case. Here, we aim to use a feedback coupling which physically corresponds to a situation where a current proportional to the difference of the slave and master output powers is electronically fed to the slave CMSL, as shown in figure 17. Accordingly, the slave rate equations may be expressed as

$$\begin{aligned}
\dot{\tilde{p}} &= \left[\frac{(1+2\tilde{n})}{1+\sigma\tilde{p}} - 1\right]\tilde{p} + \beta(\tilde{n}+\Phi)\,, \\
\dot{\tilde{n}} &= \varepsilon\left[i_0(1+m\sin(\omega t)) - K(\tilde{p}-p_{\tau_c}) - \tilde{n} - \frac{(1+2\tilde{n})}{1+\sigma\tilde{p}}\,\tilde{p}\right]\,,
\end{aligned} \tag{107}$$

where K is a scalar coupling parameter, and $\tau_c = T_c/\tau_p$ is the dimensionless coupling delay, that is, the T_c corresponds to the time needed by the master command signal to reach the slave laser. Analogously to what has been demonstrated in the first chapter for Duffing oscillators, synchronization can occur in this model only when the coupling time τ_c is an integer multiple of $2\pi/\omega$. Hence, for the sake of simplicity, we will further set $\tau_c \equiv 0$.

We now focus on the conditions under which the coupling efficiently completes a robust and high-quality synchronization. The master and slave CMSLs are described by two sets of two first-order ODEs each. For mathematical commodity, we will transform them into a single set of two second-order ODEs. Therefore, if we discard σ and β because of their very small order of magnitude ($\sim 10^{-5}$), the rate equations can now be expressed as

$$\begin{aligned}
&\ddot{p} + \varepsilon(1+2p)\dot{p} - 2\varepsilon p\left[i_0(1+m\sin(\omega t)) - p\right] - \frac{\dot{p}^2}{p} = 0\,, \\
&\ddot{\tilde{p}} + \varepsilon(1+2\tilde{p})\dot{\tilde{p}} - 2\varepsilon\tilde{p}\left[i_0(1+m\sin(\omega t)) - K(\tilde{p}-p) - \tilde{p}\right] - \frac{\dot{\tilde{p}}^2}{\tilde{p}} = 0\,.
\end{aligned} \tag{108}$$

The synchronization error $u = \tilde{p} - p$ will consequently obey in a linear approximation the following differential equation

$$\ddot{u} + \left[\varepsilon(1+2p) - \frac{2\dot{p}}{p}\right]\dot{u} + \left[2\varepsilon\left(\dot{p} + (K+2)p - i_0(1+m\sin(\omega t))\right) + \frac{\dot{p}^2}{p^2}\right]u = 0\,. \tag{109}$$

Since the chaotic attractor of the CMSL is an almost simply folded band in the phase plane (p, n), we can as explained in the first chapter replace the chaotic variable p in equation (109) by an uniperiodic Ritz-Galerkin approximation of the embedded

Table 1: Parameters and values used for the numerical simulation of CMSLs.

Parameter	**Value**
Differential gain coefficient (g)	$8.4 \times 10^{-13}\,\mathrm{m^3 s^{-1}}$
Nonlinear gain suppression factor (s)	$0.5 \times 10^{-26}\,\mathrm{m^3}$
Spontaneous emission coefficient (β)	10^{-5}
Carrier density at threshold (N_{th})	$2.018 \times 10^{24}\,\mathrm{m^{-3}}$
Carrier lifetime (τ_s)	1.025 ns
Photon lifetime (τ_p)	2.041 ps
Frequency of the modulation current (f_m)	2 GHz

UPO accordingly to

$$\overline{p}(t) = A_0 + A_1 \cos(\omega t) + B_1 \sin(\omega t)\,. \tag{110}$$

In equation (109), $\dot{p}$ and $\dot{p}^2$ can be neglected in the parametric excitation terms, since they are respectively proportional to ω (of order ε) and ω^2 (of order ε^2). Moreover, the parametric damping is of order ε, while the stiffness term is proportional to $\varepsilon^{1/2}$. Hence, the parametric damping can be replaced by its time average value

$$\lambda = \langle \varepsilon(1+2p) \rangle = \varepsilon(1+2A_0)\,. \tag{111}$$

According to the Ritz variational criterion, A_0, A_1 and B_1 obey the following set of nonlinear algebraic equations

$$\begin{aligned}
&-\omega^2 A_1 + \lambda B_1 \omega + 4\varepsilon A_0 A_1 - 2\varepsilon i_0 A_1 = 0 \\
&-\omega^2 B_1 - \lambda A_1 \omega + 4\varepsilon A_0 B_1 - 2\varepsilon i_0 B_1 - 2\varepsilon m i_0 A_0 = 0 \\
&2A_0^2 + A_1^2 + B_1^2 - 2 i_0 A_0 - m i_0 B_1 = 0\,,
\end{aligned} \tag{112}$$

while the variational equation (109) can be rewritten under the form of a canonical Mathieu equation

$$\frac{d^2\eta}{d\tau^2} + \left[\mu + 2\alpha\cos(2\tau - 2\varphi)\right]\,\eta = 0 \tag{113}$$

with the following rescalings

$$\begin{aligned}
&\tau = \frac{\omega t}{2}, \quad \eta(\tau) = u\,\exp\left(\frac{\lambda\tau}{\omega}\right), \quad \varphi = \arctan\left[\frac{B_1}{A_1} - \frac{m i_0}{(K+2)A_1}\right] \\
&\mu = \frac{4}{\omega^2}\left[2\varepsilon\left((K+2)A_0 - i_0\right) - \frac{\lambda^2}{4}\right], \\
&\alpha = \frac{4\varepsilon}{\omega^2}\left[\left((K+2)A_1\right)^2 + \left((K+2)B_1 - m i_0\right)^2\right]^{1/2}\,.
\end{aligned} \tag{114}$$

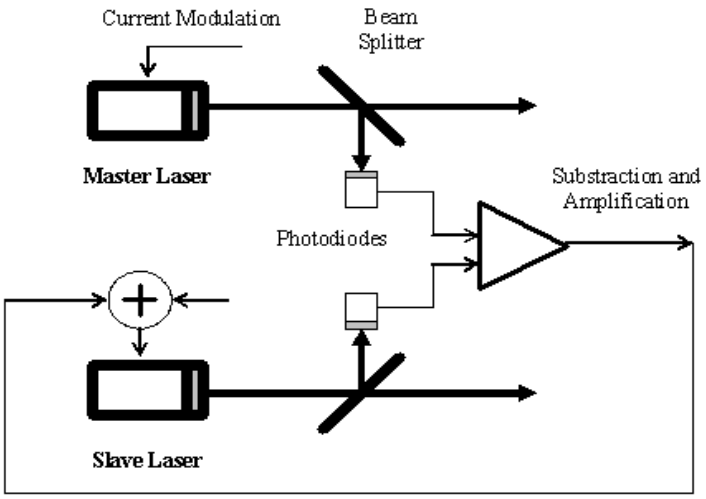

Figure 17: *Set-up for the synchronization of CMSLs. Owing to two semi-transparent mirrors or beam-splitters (BS), a fraction of the laser radiation of each CMSL is extracted, and transformed by two distinct photodiodes in electric currents. These currents are used to build the feedback loop necessary for synchronization.*

From the theory we have developed in chapter I, we can therefore conclude that ultra-high frequency current modulated semiconductor lasers do synchronize in the chaotic regime when the figurative point in the Strutt Diagram is in the linearly stable area, that is, when

$$-\sinh^2\left(\frac{\lambda\pi}{2\omega}\right) < \Gamma(\mu,\alpha) < \cosh^2\left(\frac{\lambda\pi}{2\omega}\right), \tag{115}$$

the function Γ being defined in equation (43).

On the other hand, if the local width of the buffer belt is $\overline{\Lambda}(\mu^{(k\pi)},\alpha^{(k\pi)})$, where the couple $(\mu^{(k\pi)},\alpha^{(k\pi)})$ is the related point situated on a $k\pi$-periodic boundary of the Strutt diagram ($k=1$ or 2), the synchronization fails when the figurative point in the Strutt Diagram is nonlinearly stable, satisfying

$$\begin{aligned}&\left|(\mu-\mu^{(k\pi)})\left[\frac{\partial\Gamma(\mu,\alpha)}{\partial\mu}\right]_{(\mu=\mu^{(k\pi)})}+(\alpha-\alpha^{(k\pi)})\left[\frac{\partial\Gamma(\mu,\alpha)}{\partial\alpha}\right]_{(\alpha=\alpha^{(k\pi)})}\right| \\ &<\frac{\Lambda(\mu^{(k\pi)},\alpha^{(k\pi)})}{\sqrt{(\mu^{(\pi)}-\mu^{(2\pi)})^2+(\alpha^{(\pi)}-\alpha^{(2\pi)})^2}}\cosh\left(\frac{\lambda\pi}{\omega}\right),\end{aligned} \tag{116}$$

where $(\mu^{(k\pi)},\alpha^{(k\pi)})$ is the nearest boundary point relatively to the representative point $M(\mu,\alpha)$ of the coupled system, the denominator of the right-hand side is the length

of the trajectory of $M(\mu, \alpha)$ laying within the nearest stability interval.

As we did for single-well Duffing oscillators, we can understand the effect of the scalar coupling parameter K by studying the motion of a representative point in the Strutt diagram. From equation (114), it clearly appears that when K is increased, the parameters μ and α are simultaneously varied. More specifically, the figurative point in the (μ, α) plane sketches a curve of equation

$$\alpha = \left(\frac{1}{2}\mu + \varepsilon\frac{4i_0}{\omega^2}\right)\sqrt{\frac{A_1^2+B_1^2}{A_0^2}}\left[1+\varepsilon^2\,\frac{m^2 i_0^2 - \frac{2mi_0B_1}{8\varepsilon A_0}(\mu\omega^2+8\varepsilon i_0)}{\frac{A_1^2+B_1^2}{64A_0^2}(\mu\omega^2+8\varepsilon i_0)^2}\right]^{1/2}. \qquad (117)$$

In the first approximation ($\varepsilon \to 0$), this curve can be assimilated to a straight line of slope

$$a = \frac{1}{2}\sqrt{\frac{A_1^2+B_1^2}{A_0^2}}\,. \qquad (118)$$

This slope is proportional to the ratio between the amplitude of the varying component of $\overline{p}(t)$ and the amplitude of its constant component. Therefore, a is an increasing function of the modulation index m, since a stronger parametric excitation of the CMSL leads to higher A_1 and B_1 values. As K is increased, the figurative point in the Strutt diagram moves from left to right on the curve of equation (117), and therefore alternatively passes through linearly unstable and linearly stable areas. Consequently, the synchronization intervals for K can be represented under the form $]K_{b1}, K_{b2}[,\ ]K_{b3}, K_{b4}[,...,\ ]K_{bn}, +\infty[$, where the K_{bk} are the boundary values. It appears from figure 18 that when m is small, the slope of the curve (117) is weak, and then the synchronization pattern is made of a single interval $]K_{b1}, +\infty[$. But as m is increased, this curve intersects the zones of linear instability because of its greater slope, so that the former single stability interval splits into an increasing number of different synchronization sub-intervals.

In figure 18, we have graphically represented three straight lines with distinct slopes, corresponding to different values of m. From the smallest to the largest slope, these lines respectively lead to one, two and three synchronization intervals for K. It is important to note that as we have earlier noticed, high values of m precisely correspond to the synchronization of CMSLs in their chaotic regime, so that complex stability patterns may be expected in that case. It results from the above reasoning that the period-one UPO approximation predicts the progressive occurrence of

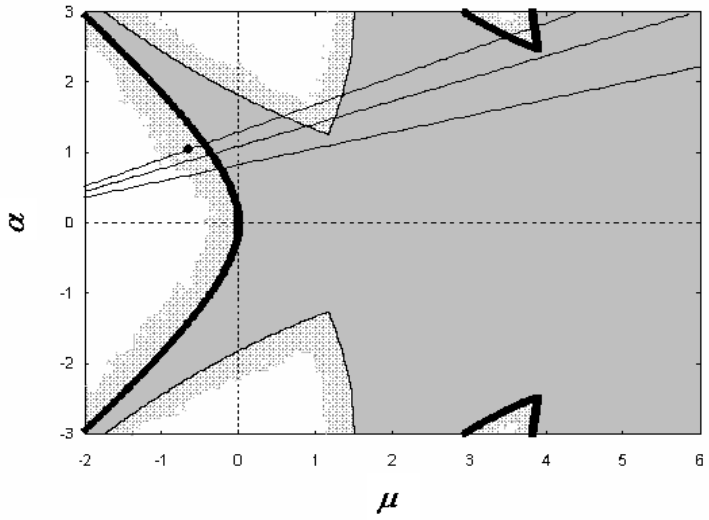

Figure 18: *Strutt diagram for the coupled CMSLs. Three straight lines with increasing slopes (*i.e.*, with an increasing modulation index m) have been sketched. On the uppermost one, which correspond to the case we are studying, the representative point of the coupled system when $K = 0$ has been represented.*

compact desynchronization intervals as the modulation index m is increased. Moreover, it synthetically provides the related geometrical explanation through the Strutt diagram interpretation. Therefore, one can expect that these compact intervals on non-synchronized behavior should emerge and widen on the K-axis as m is continuously increased.

The numerical simulations completely confirm our analytic stability analysis. In figure 19, we have represented the maximal synchronization error as a function of the coupling strength, for increasing values of the modulation index. The maximal synchronization error we have tolerated for high-quality synchronization is 10^{-5}. Therefore, synchronization intervals are indicated on figures 19 by horizontal segments of equation $\log_{10}(\|\mathbf{w}\|_{max}) = -5$.

In figure 19a, for example, m is quite small ($m = 0.1$), so that we have a single synchronization interval $]-1.00, +\infty[$. For $K < -1.00$, the slave variables indefinitely grow to infinity, while for $K > -1.00$, quasi-perfect synchronization is achieved. $K = -1.00$ is a boundary value for which a high (but not infinite) synchronization error is observed.

In figure 19b, m has been increased ($m = 0.4$), as well as the slope of the figurative curve on the Strutt diagram. This curve now intersects a nonlinear stability area,

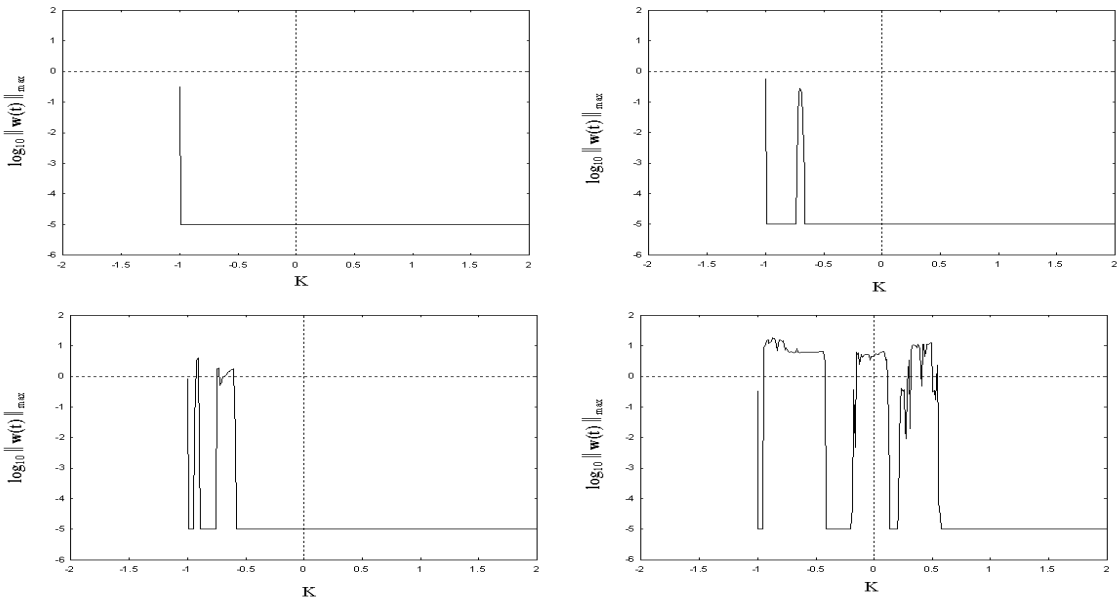

Figure 19: *Variation of the synchronization error* $\|\mathbf{w}\|_{max}$ *in coupled CMSL when* i_0 *is fixed to* 0.6. *a)* $m = 0.1$*; b)* $m = 0.4$*; c)* $m = 0.6$*; d)* $m = 1.0$. *Note the progressive occurrence and widening of compact desynchronization intervals as* m *is increased.*

thereby splitting the former semi-infinite interval of linear stability into two, which are $]-1.00, -0.73[$ and $]-0.67, +\infty[$. Nevertheless, the inner nonlinear stability interval represents a loss of synchronization, and not a growth to infinity.

When m is further increased ($m = 0.6$), the first stability interval splits into two in his turn in figure 19c, so that the stability pattern for K is now $]-1.00, -0.95[$, $]-0.90, -0.75[$ and $]-0.59, +\infty[$. According to the bifurcation diagram of figure 16b, these three m values correspond to periodic oscillations. Hence, the synchronization which occurs here (even for $K = 0$) is due to phase-locking.

We increase again m to 1.0 in figure 19d so that we are now synchronizing the CMSLs in their chaotic regime. The stability pattern is now made up of four subsets which are $]-1.00, -0.95[$, $]-0.42, -0.19[$, $]0.13, 0.21[$ and $]0.57, +\infty[$. One can note that the desynchronization intervals are larger in the chaotic state than in the periodic regime, and that obviously no synchronization occurs when $K = 0$. Moreover, synchronization is always ensured for the K values which are slightly above the π-periodic threshold value $K = -1.00$. This can easily be explained by the stability diagram of figure 18, and also from equations (108), since $K = -1.00$ is the critical value that induces the inversion of the retroactive coupling term.

The mechanism characterized by the progressive occurrence of desynchronization

intervals through the splitting into two of a synchronization interval has invariably been observed for various sets of CMSL parameters during numerical simulations. Anyway, it has been observed that the first instability interval $]-\infty, K_{b1}[$ always leads to a sustained growth to infinity for the slave variables, and should therefore be absolutely avoided. On the other hand, the inner instability intervals do not induce such a catastrophic behavior, but just fail to achieve stable and robust synchronization. This can be explained by the fact that these intervals are only weakly unstable, so that the nonlinear terms of the rate equations succeed to confine the figurative phase point within the chaotic attractor when it is repelled from the linearly unstable synchronization manifold.

3.3.3 Influence of parameter mismatch

Even though parameter mismatch is unavoidable in practice, its undesirable consequences can be limited when certain optimization requirements are met [13]. If we consider the various CMSLs parameters ψ_i and their corresponding parameter mismatches $\delta\psi_i$, the deviation vector obeys in the linear approximation to the following integral equation

$$\mathbf{w}(t) = [\mathbf{\Theta}(t)\mathbf{\Theta}^{-1}(t_0)] \cdot \mathbf{w}(t_0) + \int_{t_0}^{t} \left[[\mathbf{\Theta}(t)\mathbf{\Theta}^{-1}(\xi)] \cdot \sum_i \frac{\partial \mathbf{F}(\mathbf{x}, t, \psi)}{\partial \psi_i} \delta\psi_i \right] d\xi \,, \quad (119)$$

where $\mathbf{\Theta}(t)$ is the principal matrix function, that is, the solution of

$$\dot{\mathbf{\Theta}} = \mathbf{J}(\mathbf{x}, t) \cdot \mathbf{\Theta} \,. \quad (120)$$

The first term of equation (119) decays to $\mathbf{0}$ as $t \to +\infty$ within the stability area. The second term does never vanish and hence corresponds to the synchronization error due to the parameter mismatch. If λ_{av} is the average largest sub-Lyapunov exponent (normally negative), it can be demonstrated from equation (119) that for initially stable synchronization, $\|\mathbf{w}\|_{max}$ increases with the mismatches $|\delta\psi_i|$, but is inversely proportional to $|\lambda_{av}|$, *i.e.*, the synchronization error is minimized when $(-\lambda_{av})$ is the largest possible [13].

On figure 20, we have plotted the synchronization error as a function of the coupling strength K for different percentages of parameter mismatch in the chaotic regime. It is seen that in stable intervals, $\|\mathbf{w}\|_{max}$ effectively increases with the parameter mismatch. We also remark that the first stability interval (just at the right of the boundary value $K = -1.0$) is the least stable, since in that area, synchronization is lost for a parameter mismatch of only 1%. Anyway, above 1%, severe degradation

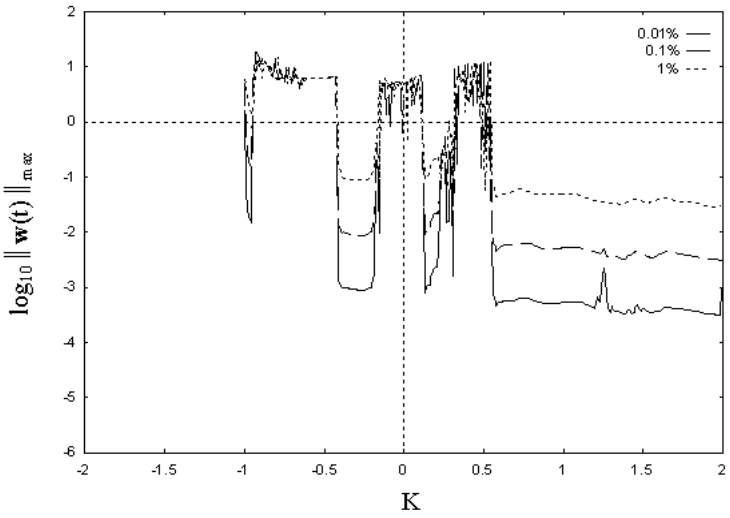

Figure 20: *Synchronization error as a function of parameter mismatch for coupled CMSLs in the chaotic regime. The global mismatches have respectively been taken to be equal to 0.01%, 0.1% and 1% .*

of synchronization has been observed. We are therefore led to the conclusion that the synchronization of chaotic CMSLs is very sensitive to parameter mismatch, because for other dynamical systems, a tolerance at up to 50% is sometimes witnessed. It is also very important to stress that no detuning has been applied between the modulation frequencies of the master and slave CMSLs. In fact, numerical simulations have indicated that even a detuning of $10^{-5}\%$ destroys the synchronized state. Therefore, a quasi-perfect stabilization of these ultra-high frequencies will be necessary for practical applications.

3.4 Dynamics and synchronization of semiconductor lasers with external optical feedback

3.4.1 Hyperchaotic dynamics and coherence collapse

Optical external feedback is another technique to increase the dimensionality of the rate equations ruling the semiconductor dynamics [23, 24]. This method consists in placing an external reflector to feed back into the active layer of the semiconductor laser a fraction of its delayed electromagnetic output. If the distance between the reflector and the output facet of the semiconductor laser is L_{ext}, then the round-trip time in the external cavity is $T = 2L_{ext}/c$. A convenient model of this configuration

should imperatively be made in the field representation, because the phase of the coherent laser radiation is strongly affected by the delayed feedback. According to Lang and Kobayashi, the rate equations corresponding to this configuration should be written in first approximation as

$$\begin{aligned}
\frac{d\mathcal{E}}{dt} &= \frac{1+i\alpha}{2}\left[\frac{g\,(N-N_0)}{1+s\,|\mathcal{E}|^2}-\frac{1}{\tau_p}\right]\mathcal{E}+\chi\mathcal{E}_T\,e^{-i\Omega T},\\
\frac{dN}{dt} &= I-\frac{N}{\tau_s}-\frac{g\,(N-N_0)}{1+s\,|\mathcal{E}|^2}\,|\mathcal{E}|^2\,.
\end{aligned} \tag{121}$$

In this equation, $\Omega = 2\pi c/\lambda$ is the angular frequency of the laser coherent radiation, so that the product ΩT can be considered as the round-trip phase shift generated by the light propagation within the external cavity. On the other hand, the parameter $\chi = r_{ext}(1-r_0^2)/\tau_{in}r_0$ is the *strength of the optical feedback*, r_0 and τ_{in} being respectively the facet amplitude reflectivity of the laser and the round-trip time within its internal cavity, while r_{ext} is the reflectivity coefficient associated with the external mirror. In equations (121), only a single reflexion has been accounted for. If we had considered multiple reflections with the external reflector, additional delays would have been introduced. Anyway, these additional delays are not relevant here because we are only concerned with weak to moderate feedbacks: under this condition, the Lang-Kobayashi model describes satisfyingly the physical system under study.

In the literature, this system constituted of a semiconductor laser with external optical feedback is commonly referred to as an **External-Cavity Semiconductor Laser** (ECSL), precisely in reference to the external reflector which plays (along with the cleaved facets of the semiconductor crystal) the role of an optical cavity.

Because of its smallness, we can neglect the gain saturation parameter s so that after a suitable normalization, the Lang-Kobayashi model can be rewritten under the synthetic form (also using equation (99))

$$\begin{aligned}
\dot{E} &= nE+\gamma E_\tau\cos(\omega\tau+\phi-\phi_\tau),\\
\dot{\phi} &= \alpha n-\gamma\frac{E_\tau}{E}\sin(\omega\tau+\phi-\phi_\tau),\\
\dot{n} &= \varepsilon\left[i_0-n-(1+2n)E^2\right]
\end{aligned} \tag{122}$$

with the following rescalings

$$\begin{aligned}
&E=\left(\frac{1}{2}g\tau_s\right)^{1/2}|\mathcal{E}|\,,\quad n=\frac{1}{2}gN_{th}\tau_p\left(\frac{N}{N_{th}}-1\right),\\
&\varepsilon=\frac{\tau_p}{\tau_s},\quad i_0=\frac{1}{2}gN_{th}\tau_p\frac{I-I_{th}}{I_{th}},\quad \gamma=\tau_p\chi=\tau_p\left(\frac{1-r_0^2}{\tau_{in}r_0}\right)r_{ext},
\end{aligned}$$

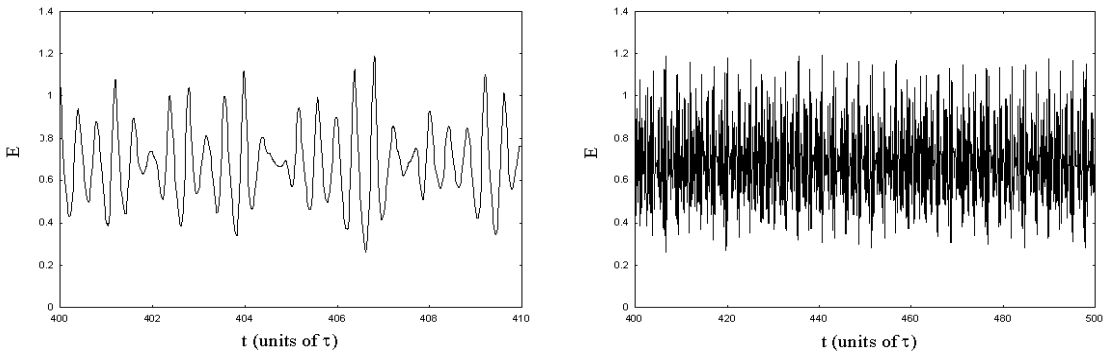

Figure 21: *Timetraces showing the hyperchaotic dynamics of an ECSL in the coherence collapse regime, with $r_{ext} = 1.35\%$ and $L_{ext} = 15$ cm. The parameters used for the numerical simulation are indicated in Table 2. a) Short scale timetrace; b) Large scale timetrace.*

Table 2: Parameters and values used for the numerical simulation of ECSLs.

Parameter	**Value**
Differential gain coefficient (g)	$8.4 \times 10^{-13}\,\mathrm{m^3 s^{-1}}$
Linewidth enhancement factor (α)	3
Facet amplitude reflectivity (r_0)	0.556
Carrier density at threshold (N_{th})	$2.018 \times 10^{24}\,\mathrm{m^{-3}}$
Injection current density (I)	$1.3 I_{th}$
Carrier lifetime (τ_s)	2.04 ns
Photon lifetime (τ_p)	1.927 ps
Round-trip time in the laser cavity (τ_{in})	8 ps

$$\tau = \frac{T}{\tau_p}, \quad \omega = \Omega \tau_p = \frac{2\pi c}{\lambda}\,. \tag{123}$$

As usual, the dots over E, ϕ and n in equations (122) denote the derivative relatively to the reduced time (in units of τ_p).

The external optical feedback radically changes the mathematical nature of the rate equations. From the low-dimensional set of *ordinary* differential equations (103), we are now led to the set of *delay* differential equations (121), that is, owing to the additional feedback term proceeding from the reflection at the external cavity, we are now in front of an *infinite-dimensional* system. Consequently, the system can display *hyperchaos*, that is, a very high-dimensional chaos with hundreds of positive Lyapunov exponents. In the context of laser physics, the resulting electromagnetic

output has a broader linewidth, so that the term **coherence collapse** is generally used to designate this phenomenon [27, 28, 29, 30, 31].

Figures 21a and 21b display the hyperchaotic dynamics of an ECSL in the coherence collapse state, respectively at a short scale and at a large scale. It is well known that the injection current i_0 strongly affects the large-scale structure of the laser's oscillations. When i_0 is very close to the threshold value $i_{0,th} = 0$, the ECSL enters into what is usually called the Low-Frequency Fluctuations (LFF) regime. In our case, i_0 is much higher, so that the hyperchaotic oscillations have a relatively constant mean value $\sqrt{i_0} \simeq 0.7$ which corresponds to the trivial steady-state regime.

3.4.2 Optimization and stability analysis of chaos synchronization

Theoretically, two fundamentally different types of chaos synchronization can occur for ECSL depending on the strengths of both the feedback and the coupling [33]. For the first type, which is referred to as *isochronous* synchronization, the slave variables synchronize (up to a constant for some of them) with those of the master at time $t - T_c$, where T_c is the coupling delay. Here, the slave is always in isochronism with its master command signal input: this kind of synchronization, which is not perfect however, is a kind of frequency-locking phenomenon. The second type of synchronization is referred to as *anticipated* synchronization because in that case, the slave laser always anticipates its master command signal input, independently of the value of T_c. Here, we will use a technique belonging to this later group, and which is based on a continuous feedback chaos control scheme.

According to Murakami and Ohtsubo [75], the synchronization of identical ECSLs can be achieved with the unidirectional coupling scheme corresponding to figure 22. Using appropriate external mirrors, the master laser-diode injects into the active region of the slave laser-diode a fraction of its electromagnetic output, which thereby plays the role of a command signal. An optical isolator guarantees the unidirectionality of the coupling. The slave ECSL is subjected to a second optical feedback which completes the retroactive control loop. However, two important physical constraints are required for the synchronization to be possible. Firstly, the coupling rate has to be equal to the feedback rate of the mirror M_{2nd}, and secondly, the round-trip phase shifts generated by the light propagation within the two external reflectors of the slave ECSL have to be π-dephased. Explicitly, this latter condition can be expressed as $\Omega T_{2nd} = \Omega T \pm (2k+1)\pi$, that is $L_{2nd} = L_{ext} \pm (2k+1)\lambda/4$, λ being the wavelength of the solitary laser and k an integer of the order of few units.

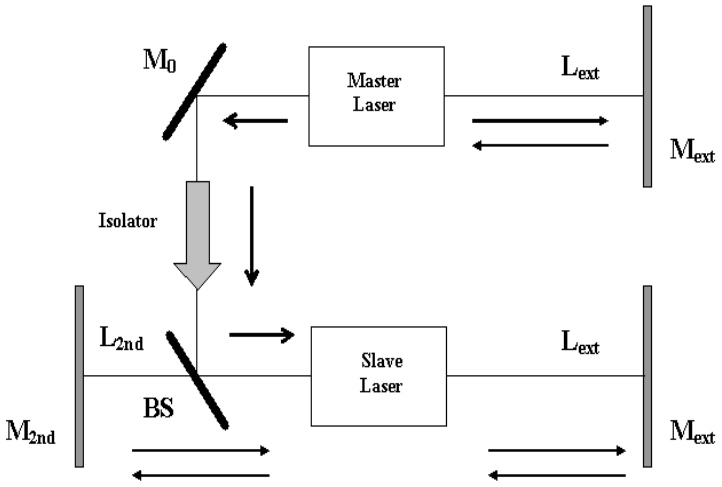

Figure 22: *Set-up for the synchronization of ECSLs. The mirrors at the right (M_{ext}) are those inducing the external optical feedback, thus creating hyperchaos. An optical isolator is introduced in the path of the command signal radiation to ensure the unidirectionality of the coupling. The mirror M_{2nd} and the semi-reflecting beam-splitter (BS) at the left of the slave laser creates the feedback loop necessary for synchronization.*

The slave rate equations corresponding to this particular coupling scheme are

$$\begin{aligned}
\dot{\tilde{E}} &= \tilde{n}\tilde{E} + \gamma\tilde{E}_\tau \cos(\omega\tau + \tilde{\phi} - \tilde{\phi}_\tau) \\
&\quad + K\left[E_{\tau_c}\cos(\omega\tau_c + \tilde{\phi} - \phi_{\tau_c}) - \tilde{E}_\tau \cos(\omega\tau + \tilde{\phi} - \tilde{\phi}_\tau)\right], \\
\dot{\tilde{\phi}} &= \alpha\tilde{n} - \gamma\frac{\tilde{E}_\tau}{\tilde{E}}\sin(\omega\tau + \tilde{\phi} - \tilde{\phi}_\tau) \\
&\quad - K\left[\frac{E_{\tau_c}}{\tilde{E}}\sin(\omega\tau_c + \tilde{\phi} - \phi_{\tau_c}) - \frac{\tilde{E}_\tau}{\tilde{E}}\sin(\omega\tau + \tilde{\phi} - \tilde{\phi}_\tau)\right], \\
\dot{\tilde{n}} &= \varepsilon\left[i_0 - \tilde{n} - (1 + 2\tilde{n})\tilde{E}^2\right], \qquad (124)
\end{aligned}$$

where the dimensionless coupling parameter K and the coupling time τ_c are respectively defined as

$$K = \tau_p\kappa = \tau_p\left(\frac{1 - r_0^2}{\tau_{in}r_0}\right)k_{cp}, \quad \tau_c = \frac{T_c}{\tau_p}, \qquad (125)$$

k_{cp} being the coupling efficiency.

In our stability analysis, we will consider $\tau \equiv \tau_c$ for the sake of exemplification on instantaneous synchronization, and therefore we will only deal with a single degenerated delay-time parameter. However, we stress that this particular case is not

restrictive, as it successfully gives a deep insight into what occurs for the general double-delay model.

To investigate the stability of the synchronization manifold, we will use an original analytical approach developed by Brown and Rulkov. The method they have proposed enables to derive rigorous stability criteria, that is, sufficient constraints which guarantee high-quality (burst-free) synchronization between identical systems with drive-response coupling [48, 49]. Moreover the Brown-Rulkov technique leads to explicit analytic stability conditions, and therefore offers a judicious guidance for the choice of the suitable system parameters.

Let us consider the master and slave vector-fields as $\mathbf{x} = (E, \phi, n)$ and $\tilde{\mathbf{x}} = (\tilde{E}, \tilde{\phi}, \tilde{n})$ respectively. Hence, the deviation vector $\mathbf{w} = \tilde{\mathbf{x}} - \mathbf{x}$ obeys in the linear approximation to the following variational equation

$$\dot{\mathbf{w}} = [\mathbf{H}(\mathbf{x}, \mathbf{x}_\tau)] \cdot \mathbf{w} + (\gamma - K)[\mathbf{G}(\mathbf{x}, \mathbf{x}_\tau)] \cdot \mathbf{w}_\tau \,, \tag{126}$$

where

$$\mathbf{H}(\mathbf{x}, \mathbf{x}_\tau) = \begin{bmatrix} n & -\gamma E_\tau \sin\varphi & E \\ \gamma \frac{E_\tau}{E^2} \sin\varphi & -\gamma \frac{E_\tau}{E} \cos\varphi & \alpha \\ -2\varepsilon(1+2n)E & 0 & -\varepsilon(1+2E^2) \end{bmatrix} \tag{127}$$

and

$$\mathbf{G}(\mathbf{x}, \mathbf{x}_\tau) = \begin{bmatrix} \cos\varphi & E_\tau \sin\varphi & 0 \\ -\frac{1}{E} \sin\varphi & \frac{E_\tau}{E} \cos\varphi & 0 \\ 0 & 0 & 0 \end{bmatrix} . \tag{128}$$

We have introduced the new variable $\varphi = \omega\tau + \phi - \phi_\tau$ as the phase delay. We now decompose the $\mathbf{H}$ matrix into its time-averaged and time-variable components, according to

$$\mathbf{H}(\mathbf{x}, \mathbf{x}_\tau) = \mathbf{A} + \mathbf{B}(t) \tag{129}$$

with

$$\begin{aligned} \mathbf{A} &= \langle \mathbf{H}(\mathbf{x}, \mathbf{x}_\tau) \rangle \\ \mathbf{B}(t) &= \mathbf{H}(\mathbf{x}, \mathbf{x}_\tau) - \langle \mathbf{H}(\mathbf{x}, \mathbf{x}_\tau) \rangle \,, \end{aligned} \tag{130}$$

where $\langle\,\rangle$ denotes the time-averaging along the master trajectory. In the first approximation, the matrix $\mathbf{B}$ can be considered as proportional to γ. This approximation

becomes more accurate as i_0 increases, since in that case, E oscillates around the mean value $\sqrt{i_0}$. Hence, $\mathbf{H}$ can finally be expressed as

$$\mathbf{H}(\mathbf{x}, \mathbf{x}_\tau) = \mathbf{A} + \gamma \mathbf{Q}(t)\,. \tag{131}$$

We emphasize that $\mathbf{Q}$ is still weakly depending on γ anyway. The matrix $\mathbf{A}$ can be diagonalized to $\mathbf{D}$ through the transfer matrix $\mathbf{P}$. Therefore the vector $\mathbf{z}$, which is the $\mathbf{w}$ counterpart in the $\mathbf{D}$ basis satisfies

$$\begin{aligned} \mathbf{z}(t) = [\mathbf{U}(t,t_0)] \cdot \mathbf{z}(t_0) \quad &+ \quad \int_{t_0}^{t} \gamma \left[\mathbf{U}(t,\xi)\,[\mathbf{P}^{-1}\mathbf{Q}(\xi)\mathbf{P}]\right] \cdot \mathbf{z}(\xi)\, d\xi \\ &+ \quad \int_{t_0}^{t} (\gamma - K) \left[\mathbf{U}(t,\xi)\,[\mathbf{P}^{-1}\mathbf{G}(\xi)\mathbf{P}]\right] \cdot \mathbf{z}_\tau(\xi)\, d\xi\,, \end{aligned} \tag{132}$$

where $\mathbf{U}(t,t_0) = \mathbf{exp}[\mathbf{D}(t-t_0)]$ is the exponential operator. Linearly stable synchronized behavior is expected if $\|\mathbf{z}(t)\| \to 0$ as $t \to +\infty$. This convergence to 0 may occur if and only if each of the three blocks in equation (132) individually vanishes at long term.

Let us now consider Λ_1, Λ_2 and Λ_3, the eigenvalues of $\mathbf{A}$ ordered as $\Re[\Lambda_1] \geq \Re[\Lambda_2] \geq \Re[\Lambda_3]$, where $\Re[\Lambda]$ is the real part of the complex eigenvalue Λ. The first block of (132) converges to $\mathbf{0}$ if

$$-\Re[\Lambda_1] > 0\,. \tag{133}$$

It is our first stability requirement. This condition is reminiscent of the negativity of transverse sub-Lyapunov exponents, but in fact, equation (133) is more constraining, because sub-Lyapunov exponents are obtained through the $\mathbf{H}$ and $\mathbf{G}$ matrices,while Λ_1 is derived through $\mathbf{A}$, which is only the time-average component of $\mathbf{H}$.

The second block uniformly tends to $\mathbf{0}$ if the exponential operator imposes to the $\mathbf{P}^{-1}\mathbf{Q}\mathbf{P}$ term its decay behavior. One can use norms to convert equation (132) into an inequality and therefore, uniform convergence is ensured if

$$-\Re[\Lambda_1] > |\gamma| \langle \|\mathbf{P}^{-1}\mathbf{Q}\mathbf{P}\| \rangle\,, \tag{134}$$

that is

$$\gamma < \frac{-\Re[\Lambda_1]}{\langle \|\mathbf{P}^{-1}\mathbf{Q}\mathbf{P}\| \rangle}\,. \tag{135}$$

It appears that the feedback coefficient has an upper limit which depends on the system's parameters. We stress again that the right-hand-side of inequality (135) depends on γ, so that this inequality is mathematically weakly implicit.

At last, the third block of (132) converges to $\mathbf{0}$ if

$$-\Re[\Lambda_1] > |\gamma - K|\langle\|\mathbf{P}^{-1}\mathbf{G}\mathbf{P}\|\rangle\,, \tag{136}$$

or more explicitly,

$$\gamma - \left(\frac{-\Re[\Lambda_1]}{\langle\|\mathbf{P}^{-1}\mathbf{G}\mathbf{P}\|\rangle}\right) < K < \gamma + \left(\frac{-\Re[\Lambda_1]}{\langle\|\mathbf{P}^{-1}\mathbf{G}\mathbf{P}\|\rangle}\right)\,. \tag{137}$$

This latter relation means that the stability basin lays within a band around the central value $K = \gamma$.

To summarize, the Brown-Rulkov technique has provided three stability constraints which are equations (133), (135) and (137). Numerical simulation qualitatively confirms these analytic results.

For this numerical comparison, two radically opposite situations will be considered: the stable and unstable bifurcation states. To understand the reason of this differentiation, one should remind the bifurcation behavior of ECSLs [75]. Their nonlinear dynamics is strongly determined by the interplay between the relaxation oscillations frequency of the solitary semiconductor laser ($f_R = \sqrt{g(I - I_{th})}/2\pi = \Omega_R/2\pi$) and the external-cavity-mode spacing frequency ($f_{ext} = 1/T = c/2L_{ext}$). As the feedback coefficient γ increases, the initially stable eigenmodes undergo a first Hopf bifurcation (1^{st} HB) to periodic oscillations. It is demonstrated [24, 29, 30] that when $\Omega_R T$ is an odd multiple of π, the competition between f_R and f_{ext} is the weakest possible and hence, the critical Hopf bifurcation value is very low: it is a *stable* bifurcation. On the other hand, when $\Omega_R T$ is an even multiple of π, this competition is the strongest possible, and the critical Hopf bifurcation value is quite high: it is here an *unstable* bifurcation. When γ is further increased, the interval of periodic oscillations is followed in the both cases by a two-frequency quasiperiodic regime after a second Hopf bifurcation (2^{nd} HB). This bifurcation sequence is universal for ECSLs, even though the critical bifurcation values are different for each eigenmode. For all the related numerical simulations, we have taken $L_{ext} = 15$ cm for the stable bifurcation and $L_{ext} = 12$ cm for the unstable one, so that we have found the Hopf bifurcation values couple of r_{ext} to be respectively $(0.34; 0.89)$ for the stable bifurcation regime, and $(1.04; 1.54)$ for the unstable case (in units of %). These Hopf bifurcations are indicated on figures 23, 24 and 25 by vertical solid lines. Also note that the maximum synchronization error we have tolerated for the stability basins is 1%.

As it can be seen in figures 23a and 23b, the boundaries of the synchronization basin qualitatively fit to our analytic study. Effectively, a maximal r_{ext} value is

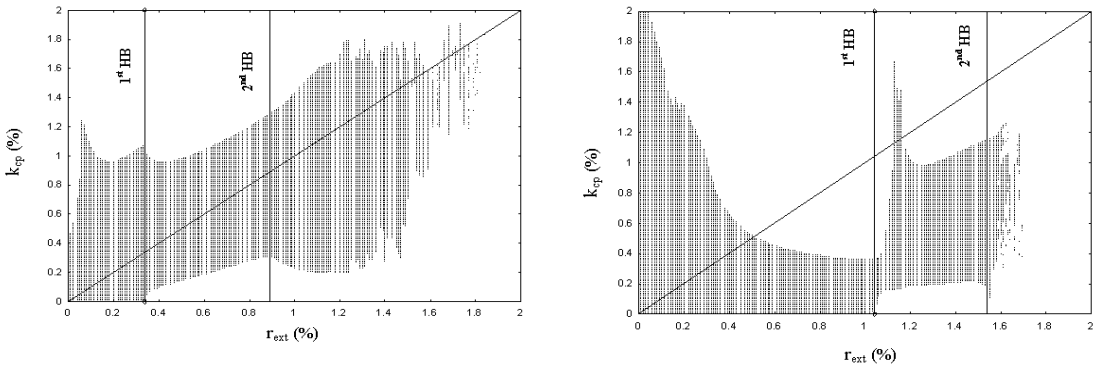

Figure 23: *Synchronization basins for ECSLs. The dark zone corresponds to the synchronization basin. a) Stable bifurcation case; b) Unstable bifurcation case.*

observed, as well as the band shape around the maximal stability diagonal $r_{ext} = k_{cp}$ (we remind that γ and K are respectively proportional to r_{ext} and k_{cp}).

The stability is mostly affected along the diagonal: therefore, we introduce a new variable

$$q_d = \sqrt{\frac{r_{ext}^2 + k_{cp}^2}{2}}\,, \tag{138}$$

which is the curvilinear coordinate along the diagonal segment $r_{ext} = k_{cp}$. Hence, since q_d is meant to be simultaneously equal to r_{ext} and k_{cp}, varying q_d implies varying the feedback rate γ and the coupling rate K at the same time.

In figures 24a and 24b, we have plotted $\Re[\Lambda_1]$ as a function of q_d. It appears that for the stable bifurcation, the Brown-Rulkov technique foresees synchronization for very weak q_d . As q_d increases, $\Re[\Lambda_1]$ becomes positive and intermittently drops below 0 for $q_d > 1.79$. Nevertheless, synchronization can not be regained in that case because the second stability requirement is no more respected: q_d (here corresponding to γ) is then too large and $(-\Re[\Lambda_1])$ too low to satisfy the inequality (135). For the unstable bifurcation, synchronization for very weak feedback is also guaranteed.

Globally, the Brown-Rulkov technique leads to interesting results, but unfortunately, it is striking that the consequent stability criteria are overly strong. For example, they fail to foresee stability within the chaotic range, which is however the most interesting. Nevertheless, we can circumvent this deficiency by diagonalizing $\mathbf{H}$ with its related sub-Lyapunov exponents $\lambda_1 \geq \lambda_2 \geq \lambda_3$, (which are obtained regardless of the delay), rather than $\mathbf{A}$ with the eigenvalues $\Re[\Lambda]$ in the Brown-Rulkov method. The resulting stability criteria thereby loose their mathematical rigor but,

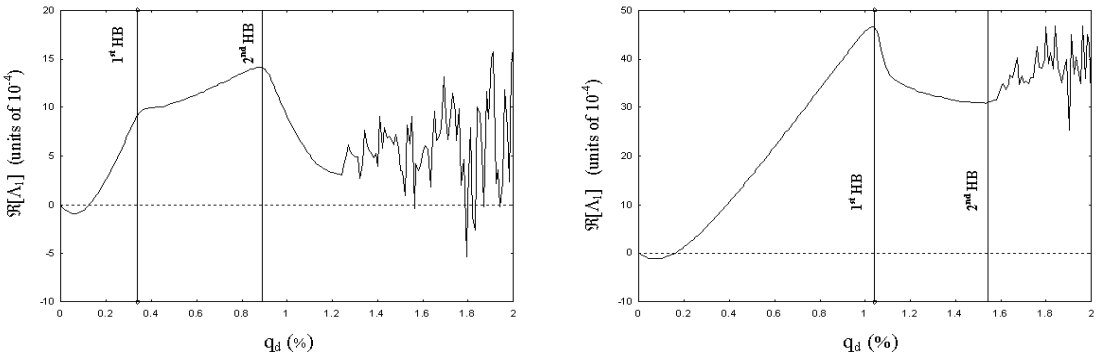

Figure 24: *Variation of* $\Re[\Lambda_1]$ *along the diagonal* $r_{ext} = k_{cp}$*. a) Stable bifurcation case; b) Unstable bifurcation case.*

and this is the most important, they still provide necessary conditions for synchronization to occur. Proceeding in that way, the three stability criteria (133), (135) and (137) degenerate into two which are

$$-\lambda_1 > 0\,, \tag{139}$$

and

$$\gamma - \left(\frac{-\lambda_1}{\langle\|\mathbf{L}^{-1}\mathbf{G}\mathbf{L}\|\rangle}\right) < K < \gamma + \left(\frac{-\lambda_1}{\langle\|\mathbf{L}^{-1}\mathbf{G}\mathbf{L}\|\rangle}\right)\,, \tag{140}$$

where $\mathbf{L}$ is the transfer matrix from $\mathbf{H}$ to its diagonal counterpart. Equation (139) replaces both equations (133) and (135), and then intrinsically contains the upper limitation of γ. Moreover, it exactly corresponds to the well-known standard stability condition. On the other hand, equation (140) stands for equation (137) with the same geometrical meaning.

Figures 25a and 25b display the variations of λ_1 as a function of q_d , and it clearly appears that the new set of stability criteria (139) and (140) more accurately fit with the numerical boundaries of the synchronization basin. Equation (139) decides the stability of the synchronization along the diagonal, while equation (140) does the same for the transverse direction. Effectively, it appears that as q_d is increased (along the diagonal), the synchronization is stable when λ_1 is negative, while in the perpendicular direction, the width of the basin varies accordingly to $|\lambda_1|$, *i.e.*, the basin is larger as $|\lambda_1|$ is greater. Therefore, one can conclude (even though it is not new) that the synchronization is optimized when λ_1 is the most negative possible.

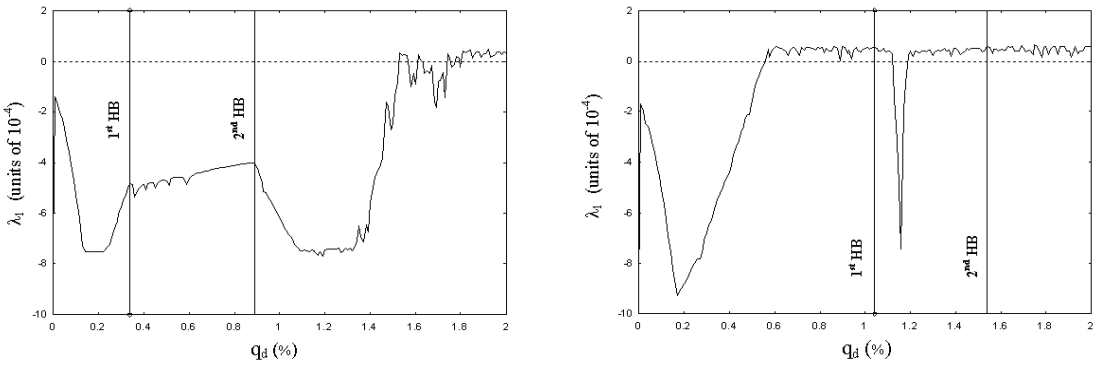

Figure 25: *Variation of λ_1 along the diagonal $r_{ext} = k_{cp}$. a) Stable bifurcation case; b) Unstable bifurcation case.*

3.4.3 Influence of parameter mismatch

If as in the case of CMSLs we consider the various CMSLs parameters ψ_i and their corresponding parameter mismatches $\delta\psi_i$, the deviation vector can be expressed at a linear approximation under the integral form

$$\mathbf{w}(t) = [\mathbf{\Theta}(t)\mathbf{\Theta}^{-1}(t_0)] \cdot \mathbf{w}(t_0) + \int_{t_0}^{t} \left[[\mathbf{\Theta}(t)\mathbf{\Theta}^{-1}(\xi)] \cdot \sum_i \frac{\partial \mathbf{F}(\mathbf{x}, \mathbf{x}_\tau, \psi)}{\partial \psi_i} \delta\psi_i \right] d\xi \,, \quad (141)$$

where the principal matrix function $\mathbf{\Theta}(t)$ obeys to

$$\dot{\mathbf{\Theta}} = \mathbf{H}(\mathbf{x}, \mathbf{x}_\tau) \cdot \mathbf{\Theta} + (\gamma - K)\mathbf{G}(\mathbf{x}, \mathbf{x}_\tau) \cdot \mathbf{\Theta}_\tau \,. \quad (142)$$

As earlier noticed, the first term in equation (141) is a transient component which asymptotically converges to $\mathbf{0}$ within the stability basin, and the second term fully defines the synchronization error due to parameter mismatch. Further analysis would lead to the conclusion that the synchronization error is roughly proportional to the mismatches and inversely proportional to the sub-Lyapunov exponents. Figures 26a and 26b confirm this argumentation, as it can be seen that the synchronization error inversely follows the variations of λ_1, and increases accordingly with the parameter mismatch. For example, in the stable bifurcation case, the variations of $\|\mathbf{w}\|_{max}$ have approximately the same qualitative variations (note the jumps around the Hopf bifurcations), so that we can conclude that owing to the high $|\lambda_1|$, the slave ECSL still follow the master even through bifurcations. On the other hand, the same remarks can be made for the unstable bifurcation case in the first stability interval. Nevertheless in that case, when the mismatch increases, the second synchronization interval which is in fact weakly stable does progressively vanish.

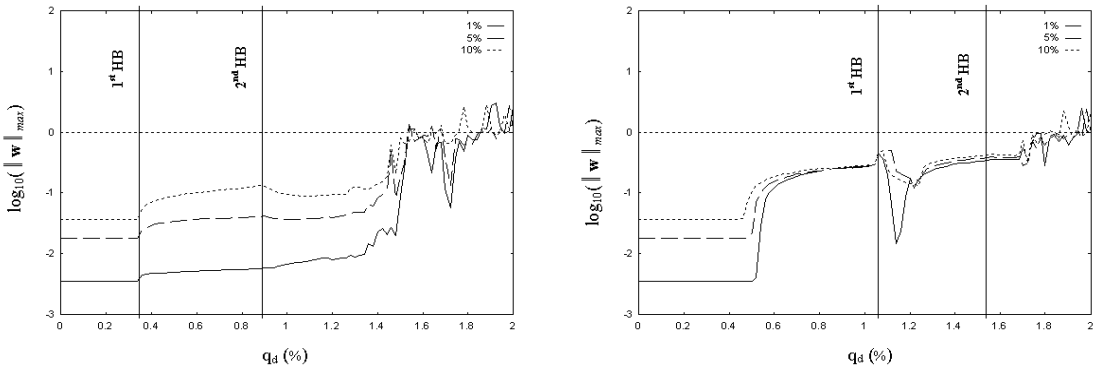

Figure 26: *Influence of parameter mismatch in ECSLs. The global mismatch between master and slave lasers has been successively set to 1%, 5% and 10%. a) Stable bifurcation case; b) Unstable bifurcation case.*

3.5 Conclusion

We have performed the stability analysis for the synchronization of chaotic semiconductor lasers, either subjected to ultra-high frequency current modulation or optical external feedback.

For CMSLs, we have used our conventional approach which has resumed the stability study to a Floquet problem. Hence, we have been able to explain the occurrence of instability intervals when the parameters and/or the coupling strength are varied. For the case of ECSLs, the Brown-Rulkov technique has provided stability constraints which have enabled us to foresee the shape of the synchronization basin.

In both cases, the influence of parameter mismatch on the quality of the synchronization has been investigated, and the underlying influence of (Hopf) bifurcations has been investigated. The next chapter will be entirely devoted to the exploitation of these results in view of cryptography and switching applications.

CHAPTER IV

APPLICATION TO CRYPTOGRAPHY AND TO SWITCHING IN OPTICAL-FIBER TELECOMMUNICATION NETWORKS

4.1 Introduction

The principal focus of this last chapter is the application of laser chaos to cryptography and switching in optical-fiber networks.

We first present a brief overview of semiconductor lasers physics, laying particular emphasis on the important role they play in optical communications systems. Then, unidirectional chaos synchronization of semiconductor lasers will be used to perform the encryption of digital signals in these optical-fiber networks. Finally, we will show that cluster synchronization of such lasers can in principle be used to switch different chaos-secured work-stations in a multi-user configuration.

4.2 Semiconductor lasers in optical telecommunication systems

In modern telecommunication systems, information is carried by electromagnetic waves whose frequencies can vary from few megahertz to hundreds of terahertz. The term *optical communications* is reserved for telecommunication systems where the electromagnetic wave (or *carrier*) has a frequency belonging to the visible or near-infrared range of the electromagnetic spectrum ($\sim$ 100 THz, or equivalently, $\lambda \sim 1\,\mu$m). It is said that optical communications systems belong to the *lightwave technology*, by opposition to the *microwave technology* which corresponds to radio-communications (carrier frequencies of $\sim$ 1 GHz). The principal advantage of light-wave technology systems is that they can easily transmit information at 10 Gbits/s (and even at up to 40 Gbits/s), while their microwave counterpart are generally 100 times slower [69, 76].

In general, independently of its initial format (voice, image, data), any information

to be transmitted should first be digitalized, that is, converted into a string of *bi*nary digi*ts*, or *bits*. After digitalization, the binary signal is encoded within the optical carrier though a process which is referred to as *shift-keying*. An optical communication system is said to be *coherent* in the case of field shift-keying (amplitude, phase, frequence), and it is said to be *incoherent* in the case of intensity shift-keying.

Transmission in lightwave technology relies on guided propagation of light in low-loss optical fibers. Therefore, the information-bearing optical carrier is launched within an optical fiber whose length can vary from few kilometers to trans-oceanic distances. To minimize the detrimental effects of power attenuation and chromatic dispersion, the transmitters in optical fibers networks should emit a high-power and quasi-monochromatic light. Owing to the inherent properties attached to their coherent output radiation, semiconductor lasers fulfill these requirements in the visible and near-infrared ranges, so that they have logically been adopted as conventional transmitters in optical communication systems.

It is notorious that the on-going *information age*, with millions of computers interconnected by telecommunication systems, has been essentially powered by the association of microelectronics and lightwave technology.

4.3 Application of complete synchronization to cryptography in optical-fiber networks

4.3.1 Chaos cryptography

The most important application of chaos synchronization is cryptography [77, 78].

A decisive breakthrough in the topic of chaos cryptography was achieved by Cuomo and Oppenheim in 1993 [79], when they demonstrated experimentally (with a couple of chaotic Lorenz electronic circuits) that the unpredictability of chaotic oscillations can be used to encrypt information-bearing signals, while their determinism –materialized by synchronization– can be used to decrypt them [80, 81, 82].

To illustrate the mathematical backbone of chaos cryptography theory, let us suppose that we aim to encrypt an information carried by the signal $m(t)$.

There are two groups of chaos-encryption techniques. On the one hand, we have the group of **internal modulation** schemes, which can be represented under the following generic form

$$\dot{\mathbf{x}} = \mathbf{F}\left[\mathbf{x}, m(t)\right]$$

$$\dot{\tilde{\mathbf{x}}} = \tilde{\mathbf{F}}\left[\tilde{\mathbf{x}}, \mathbf{x}\right] \quad \text{with} \quad \tilde{\mathbf{F}}[\tilde{\mathbf{x}}, \tilde{\mathbf{x}}] \equiv \mathbf{F}[\tilde{\mathbf{x}}, 0]\,. \tag{143}$$

Here, the message $m(t)$ is assumed to be small relatively to the norm $\|\mathbf{x}(t)\|$ of the master vector state. However, even though $\mathbf{x}$ is still chaotic, it is imperceptibly influenced by the small message $m(t)$ through a chaotic mixing ruled by the flow $\mathbf{F}$: this is why these encryption schemes are referred to as internal. Therefore, since the master system $\mathbf{x}$ carries and encrypts the information within its unpredictable and apparently random waveform, it is referred to as the **emitter** in the chaos cryptography terminology. Decryption is achieved by synchronizing an identical system $\tilde{\mathbf{x}}$, referred to as the **receiver**, to the emitter, so that the deviation vector $\mathbf{w} = \tilde{\mathbf{x}} - \mathbf{x}$ obeys

$$\dot{\mathbf{w}} = -m(t)\,\left[\frac{\partial \tilde{\mathbf{F}}}{\partial m}\right]_{m=0} + \underbrace{\left[\frac{\partial \tilde{\mathbf{F}}}{\partial \tilde{\mathbf{x}}}\right]_{\mathbf{w}=\mathbf{0}} \cdot \mathbf{w}}_{\text{decays to } \mathbf{0}}\,. \tag{144}$$

If $\mathbf{x}$ and $\tilde{\mathbf{x}}$ do synchronize when $m(t) \equiv 0$, the sub-Lyapunov exponents are negative, the second term of equation (144) decays to $\mathbf{0}$. Therefore, the deviation vector is now proportional to the message and enables its extraction. In other words, all the information contained in the signal $m(t)$ can now be obtained through $\mathbf{w}$, that is, just by making a substraction between the receiver and emitter state vectors. Under certain conditions which tightly depend on the flow $\mathbf{F}$, an appropriate processing can enable a proper extraction of the message $m(t)$ through equation (144).

On the other hand, we have **external modulation** schemes, which can be written under the form

$$\begin{aligned} \dot{\mathbf{x}} &= \mathbf{F}[\mathbf{x}] \\ \dot{\tilde{\mathbf{x}}} &= \tilde{\mathbf{F}}\left[\tilde{\mathbf{x}}, \mathbf{f}(\mathbf{x}, m(t))\right] \quad \text{with} \quad \tilde{\mathbf{F}}\left[\tilde{\mathbf{x}}, \mathbf{f}(\tilde{\mathbf{x}}, 0)\right] \equiv \tilde{\mathbf{F}}\left[\tilde{\mathbf{x}}, \tilde{\mathbf{x}}\right] \equiv \mathbf{F}[\tilde{\mathbf{x}}]\,. \end{aligned} \tag{145}$$

In this case, the emitter $\mathbf{x}$ *is not* influenced by the message, but the chaotic command (or coupling) signal is mixed with the message $m(t)$ through the vectorial function $\mathbf{f}$ before injection in the slave system $\tilde{\mathbf{x}}$. In this case, the decryption process relies on

$$\dot{\mathbf{w}} = m(t)\,\left[\frac{\partial \tilde{\mathbf{F}}}{\partial \mathbf{f}}\right]_{m=0} \cdot \left[\frac{\partial \mathbf{f}}{\partial m}\right]_{m=0} + \underbrace{\left[\frac{\partial \tilde{\mathbf{F}}}{\partial \tilde{\mathbf{x}}}\right]_{\mathbf{w}=\mathbf{0}} \cdot \mathbf{w}}_{\text{decays to } \mathbf{0}}\,. \tag{146}$$

As in the internal modulation case, the second term should vanish owing to synchronization and the first term would allow the recovering of the encrypted message.

Security in chaos cryptography relies on three important points:

• The message is contained in a small signal which is mixed within a chaotic waveform of greater size. Security is ensured by the fact that the chaotic waveforms are unpredictable and apparently random.

• Decryption is theoretically possible only if the receiver is identical, or almost identical to the emitter. If it is not the case, synchronization does not occur and the second term of equations (144) and (146) do not decay to zero: it is said that **decryption is performed by "chaos pass filtering"**, or in other words, by the process by which the receiver only recognizes the chaotic masking component of the incoming information-bearing signal and extracts it to reveal the originally transmitted message.

• The coupling between the emitter and the receiver is ensured by the information-bearing chaotic signal. Generally, this signal consists of a single component x_k of the emitter state vector $\mathbf{x}$, which is therefore called *carrier* by analogy to the telecommunication engineering technology. Consequently, an eventual eavesdropper (or spy) trying an unauthorized signal interception would difficultly succeed to decrypt it, since he would only have a single variable x_k amongst the n (or infinity in case of DDEs) other ones.

It is however impossible to built identical systems experimentally, so that *parameter mismatches* are unavoidable between the emitter and the receiver. Hence, the quality of synchronization is always degraded as highlighted in the preceeding chapter. Effectively, when there is parameter mismatch, the second terms of the right hand-side in equations (119) or (141) should be added in the right hand-side of equations (144) and (146), thereby impeding a proper recovery of the encrypted message $m(t)$. Nevertheless, this degradation plays an interesting double role: on the one hand, since an authorized receiver will anyway always suffer a small parameter mismatch, it is of extreme importance that this small imperfection does not impede an efficient decryption at the receiver. On the other hand, it is expected that the parameter mismatch suffered by the unauthorized receiver of an eventual eavesdropper should impede him to achieve a successful decryption.

4.3.2 Optical chaos cryptography

As earlier highlighted, chaos cryptography has emerged as the most efficient and the most promising emerging technology attached to chaos synchronization. In particular, since the emitters and receivers in modern optical telecommunications networks

are semiconductor lasers, the study of their synchronization in view of cryptographic applications has turned out to be a leading topic in the nonlinear dynamics literature. We aim here to achieve the encryption and decryption of digital messages with semiconductor lasers in an hyperchaotic regime.

Optical chaos communication schemes can schematically be represented as in figure 27. Initially, information proceeding from multimedia sources (telephone, internet, etc...) are processed and multiplexed in order to generate a unique binary string. This binary information is encrypted through mixing with an (hyper-)chaotic laser radiation. After propagation in the optical fiber channel, synchronization is achieved with a receiver laser enslaved to the emitter one, and the encrypted information is thereby extracted. Finally, further processing and demultiplexing operations enable to restore the the initial information which has therefore been securely transfered. To illustrate the mechanism of optical chaos communications, we will consider a non-return-to-zero (NRZ) digital message $m(t)$ which can only take the values 0 or 1, and secured transmission of this message with hyperchaotic external-cavity semiconductor lasers will be performed by two different encryption techniques.

The first technique is an internal modulation scheme referred to in the literature as **Chaos Shift-Keying** (CSK). It consists in modulating a parameter of the master laser accordingly to the digital message to encrypt. Generally, the injection current I is an easily-tuneable parameter which is perfectly suitable for such a purpose. Therefore, CSK encryption within that frame can be performed by replacing the injection current I by the modulated one $I \cdot (1 - \rho m(t))$ in the emitter laser (master equation 123). Here, ρ is a dimensionless coefficient referred to as the *modulation index of the encryption*, in the sense that it defines the amplitude $I \cdot \rho m(t)$ of the encrypted signal relatively to the amplitude I of the carrier.

The security of the encrypted message can only be guaranteed when ρ is very small (less that 0.05, or 5%). Effectively, when ρ is small, the injection current does not vary significantly (because $p \simeq p \cdot (1 - \rho)$), so that the carrier E is not visibly modified by the encrypted message. Here, decryption at the level of the receiver will rely on our study of parameter mismatch: when a 0 is encrypted at the emitter, the master and the receiver are perfectly matched and the synchronization error is 0, whereas when a 1 is encrypted at the emitter, the master and the receiver are mismatched (injection current $I \cdot (1-\rho)$ at the emitter and I at the receiver), so that the synchronization error is different from 0. Consequently, the 0/1 sequence of the initial message are recovered by a *synchronization/desynchronization* sequence at the

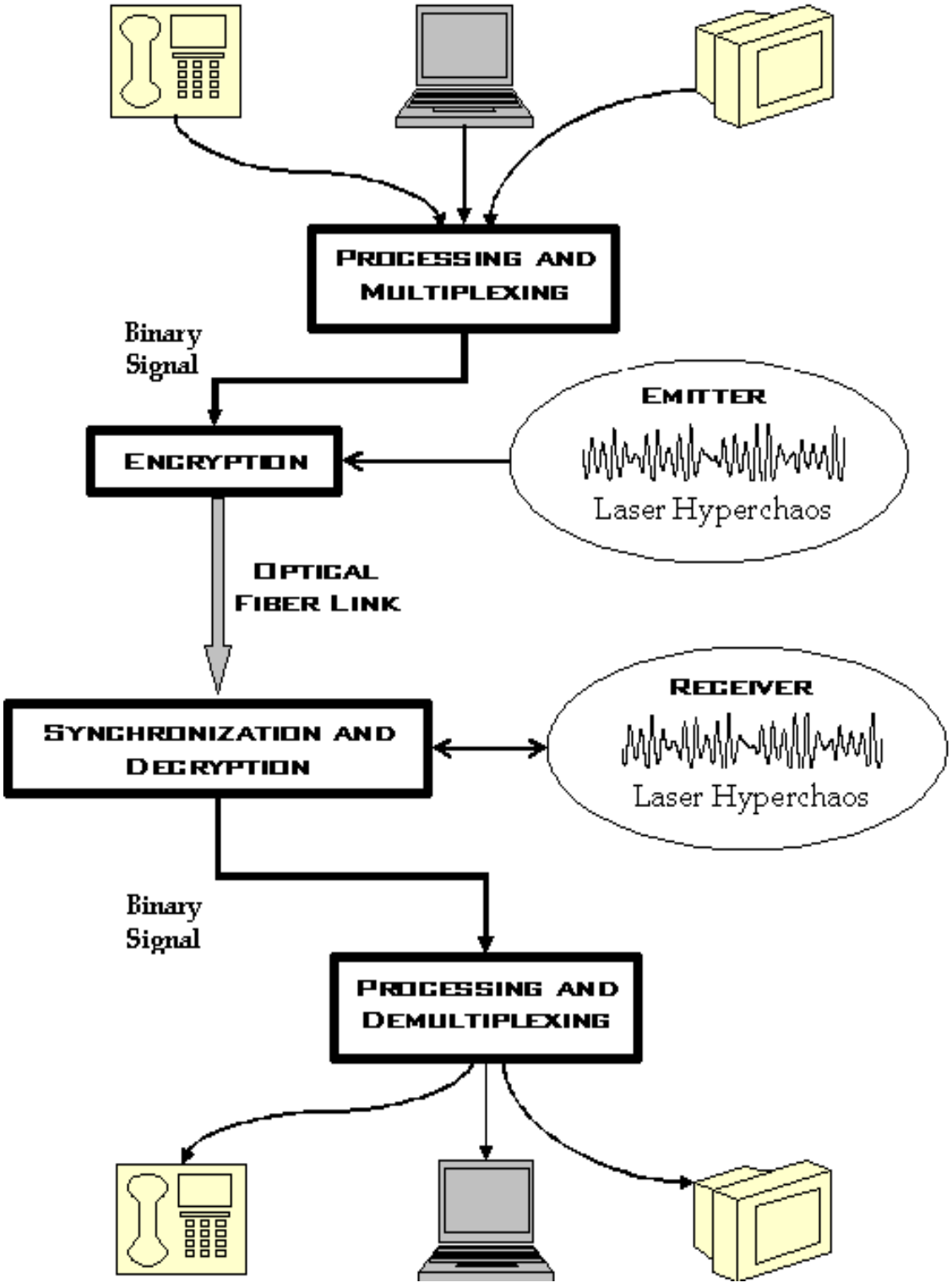

Figure 27: *Schematic representation of an optical chaos communication system.*

receiver.

The left column of figure 28 displays the numerical simulation corresponding to CSK encryption. The first figure displays the message $m(t)$ to encrypt, the second shows the emitter E containing the message, the third displays the receiver $\tilde{E}$, and the last figure shows the decrypted message $\tilde{E} - E$. It can be seen that owing to the very small modulation index of encryption (1%), the message can not be identified in the carrier E. At the decryption level, one can note that the synchronization/desynchronization sequence perfectly fits with the encrypted message and thereby enables its recovery.

The second encryption technique we consider is **Chaos Modulation** (CMO), and it is an external modulation scheme. In this case, the parameters of both master and slave lasers are still matched, but an external field modulator (a Mach-Zehnder, for example) does modify the amplitude of the emitter before it is sent and coupled to the receiver. Hence, CMO encryption is achieved by replacing $\mathcal{E}$ by $\mathcal{E} \cdot (1 - \rho m(t))$ in the slave laser equation, where ρ is still the modulation index of the encryption.

As in CSK, ρ has to be small to ensure security. When a 0 is encrypted, the slave does synchronize with the incoming field $\mathcal{E}$ and does not generate any synchronization error. On the other hand, when a 1 is encrypted, the slave can not synchronize with $\mathcal{E} \cdot (1 - \rho)$ because it does not fit with its proper dynamics: a desynchronization burst is therefore observed.

In the right column of figure 28, it is demonstrated that CMO also enables secure transmission in optical fiber networks. The figures are displayed as for CSK, and the last one presents the correspondence between the encrypted and decrypted messages.

4.3.3 Reliability and efficiency of optical chaos cryptography

The reliability and efficiency of optical cryptography depends on a certain number of key-parameters. The first and most important one is **parameter mismatch** as earlier emphasized, in the sense that the decryption at the receiver critically depends on the accuracy of tracking between the master and slave semiconductor lasers [83]. Since real lasers do not strictly obey simple rate equations as the Lang-Kobayashi model, matching is a very difficult task in practice. However, the fact that two lasers grown in different wafers can hardly synchronize is a good point for chaos cryptography.

Another important issue is the **noise** produced in the lasers or in the communication channel. Such noises deteriorate the accuracy of the synchronization, and can

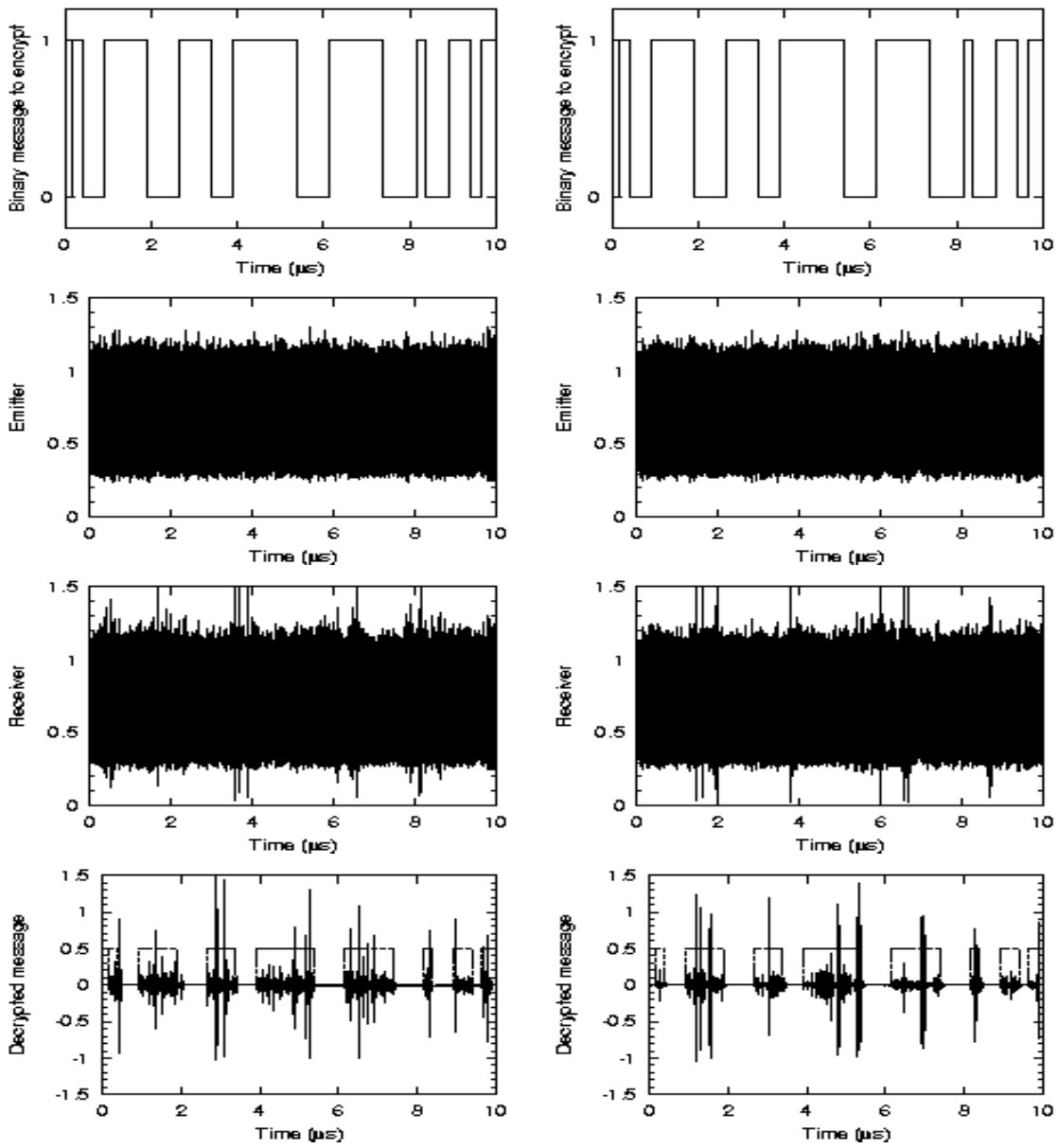

Figure 28: *The different steps of optical chaos encryption.*
The left column displays the CSK encryption scheme, and the right column the CMO. In both cases, the encryption modulation index has been taken as $\rho = 1\%$ *. The parameters correspond to those of chapter II for a stable bifurcation, with the specific feedback and coupling rates of* $r_{ext} = k_{cp} = 1.3\%$ *.*
The first row displays the binary message to be encrypted.
The second row shows the emitter timetraces.
The third shows the receiver timetraces.
The last row shows the decrypted message, along with the encrypted one in dashed line to facilitate the comparison. It can clearly be seen that the bits 1 *are decrypted as chaotic bursts, while the bits* 0 *are identified by the absence of such bursts.*

even destabilize the synchronization manifold.

Also crucial is the issue of **dispersion** during propagation in the optical-fiber communication link. The output radiation of a solitary laser has a linewidth of only few Mega-Hertz, so that it practically does not suffer dispersion while propagating in the fiber. However, a chaotic laser has a broader linewidth (few Giga-Hertz), and is therefore more sensitive to dispersion. The consequence of this linewidth broadening in (hyper-)chaotic semiconductor lasers is that fiber communication links should be significantly shorter than conventional ones [35].

Chaos cryptography may be efficient only if the **bit-rate** of the message to secure is 2 or 3 times smaller than the bandwidth of chaos. Examples of satisfying experimental encryption/decryption are numerous [36, 84, 85, 88, 89], but since modern optical communications sometimes require quite high bit-rates (> 1 Gb/s), several research groups have tried to fulfill that constraining requirement. Some of them have yet reported successful experimental encryption and decryption with chaotic semiconductor lasers at up to 2.5 Gb/s [90], and presently, experimentalists are trying to overstep the important commercial threshold of 10 Gb/s, so that current a wide-open issue is to find suitable hyperchaotic laser generators for that purpose.

Finally, a crucial issue: the **modulation index of the encryption**. Security can be ensured only when this parameter is very small. Failure to fulfill this requirement would represent a drawback and an open door for eavesdroppers attacks. Along that line, several theoretical works have yet demonstrated that in some cases, chaos cryptography may be vulnerable to unauthorized deciphering [91, 92, 93, 94, 95, 96, 97, 98]. But more than the modulation index of the encryption, security strongly relies on the high *complexity* and *unpredictability* of the chaotic carriers. As explained in the first chapter, the complexity and the unpredictability of a chaotic variable can be evaluated in terms of Kaplan-Yorke dimension and Kolmogorov-Sinaï entropy respectively, and encryption should be preferably performed with parameters for which these indicators are the highest possible.

4.3.4 Electronic and microwave chaos cryptography

Beside the possibility of optical chaos cryptography, current investigations are led worldwide to apply chaos cryptography techniques to situations where the message to encrypt is physically represented by a low-frequency electric variable or an radio-frequency microwave. Effectively, encryption of electronic signals may find a direct and interesting application for security in cupper-wire telecommunication networks, where for example voice is carried in the base-band 0-4 kHz. For that purpose, one

may directly use low dimensional chaotic oscillators with Duffing or Van der Pol nonlinearities [99]. In that context, the results we have obtained in Chapters I and II may directly be used for cryptography. Furthermore, a decisive breakthough has been achieved along the line of the application-oriented miniaturization of chaotic circuits in 1993, when a 2.4 μm CMOS prototype of the chaotic Chua's circuit was successfully built and tested. The corresponding chip only occupied a surface of 0.35 mm^2, with a power consumption of 1.6 mW under $\pm$2.5 V [100].

Investigations are also being developed for microwave applications [101], and the eventuality of using band-pass chaos to secure mobile telecommunications has yet reached the stage of experimentation.

4.4 Application of cluster synchronization to switching in chaos-secured networks

Several key-issues remain opened as far as the practical set-up of chaos-securing schemes is concerned. The main problem in chaos-secured networks is that some informations may need to be encoded (because they require privacy) while others do not (for example, signalization data, alert and emergency signals, etc...). In the same spirit, the network can be shared amongst users which may need to work in separated but secured working-groups, *i.e.*, the network configuration should allow to each user a restricted mutual visibility with only a few others. In both cases, the well-known securing scheme where all the emitters and receivers are uniformly synchronous is no more convenient as it fails to satisfy the specific needs inherent to a realistic communication network.

To take into account these various configurations, several distinct transmission channels have to be considered and therefore, switching problems arise. Obviously, the conventional automatic switching techniques are perfectly suited for algorithmic-key encryption, but unless a (potentially decipherable) buffer software system is set up on purpose, they do not fit with the chaos-securing scheme. We aim here to design a network of coupled chaotic semiconductor lasers, where the switching will be ensured through cluster synchronization. Assimilating the various cluster patterns to the different switching states of the communication system, we define how the network can be switched from one state to another depending on the type of coupling, the number of oscillators and the boundary conditions. To illustrate our approach, we will consider a network of coupled current-modulated semiconductor lasers, because

the stability of the clusters resulting from their coupling, as well as the bifurcations between them can topologically be analyzed through the Strutt Diagram.

4.4.1 Cluster synchronization in coupled chaotic semiconductor lasers

Different methods can be set up to couple the CMSLs. However, we require the coupling to be shift-invariant in the study, so that it does not induce any complicating vertical hierarchy in the switching architecture. The most common examples of shift-invariant coupling are the global (all-to-all) and the nearest-neighbor (diffusive) couplings. For the sake of generality, we will here simultaneously consider the both. This will thereby provide two control parameters (namely the two related coupling strengths) and consequently enable to profit from the specific and distinct properties of these two types of coupling. Moreover, in case of necessity, one can simply set one coefficient to zero. Physically, we assume that the couplings are carried out through the injection currents, *i.e.* we assume that currents proportional to suitable linear combinations of the output electromagnetic powers are electronically fed back in the laser diodes. The practical advantage of this coupling scheme is that it can perfectly fit with the micro-chip structure of the CMSLs. Considering a finite set of N chaotic laser diodes, the dynamics of each item is therefore subjected to

$$\begin{aligned}
\dot{p}_k &= \left[\frac{(1+2n_k)}{1+\sigma p_k} - 1\right] p_k + \beta(n_k + \Phi), \\
\dot{n}_k &= \varepsilon \left\{ i_0(1 + m\sin(\omega t)) + G\sum_{j=1}^{N} \frac{(p_j - p_k)}{N} + K(p_{k+1} - 2p_k + p_{k-1}) \right. \\
&\quad \left. -n_k - \frac{(1+2n_k)}{1+\sigma p_k}\, p_k \right\},
\end{aligned} \tag{147}$$

where G and K are the global and diffusive scalar coupling parameters respectively, while $k = 1, ..., N$. Naturally, the state variables p_k and n_k obey to the shift-invariance condition $(p_{k+N}, n_{k+N}) \equiv (p_k, n_k)$. As in the preceeding chapter, we can rewrite the coupled set of evolution equations under the following convenient form

$$\begin{aligned}
&\ddot{p}_k + \varepsilon(1+2p_k)\dot{p}_k - \frac{\dot{p_k}^2}{p_k} \\
&+2\varepsilon \left[i_0(1 + m\sin(\omega t)) + G\sum_{j=1}^{N} \frac{(p_j - p_k)}{N} + K(p_{k+1} - 2p_k + p_{k-1}) - p_k \right] p_k = 0\,.
\end{aligned} \tag{148}$$

Then, the linearization of equation (148) around the states p_k yields

$$\ddot{\xi}_k \quad + \quad \left[\varepsilon(1+2p_k) - \frac{2\dot{p}_k}{p_k}\right] \dot{\xi}_k$$

$$
\begin{aligned}
&+ \quad \left\{ 2\varepsilon \left(\dot{p}_k + 2p_k - i_0(1 + m\sin(\omega t)) \right) + \frac{\dot{p}_k^2}{p_k^2} \right. \\
&\left. + G \sum_{j=1}^{N} \frac{(p_j - p_k)}{N} + K(p_{k+1} - 2p_k + p_{k-1}) \right\} \xi_k \\
&= \quad 2\varepsilon p_k \left[G \sum_{j=1}^{N} \frac{(\xi_j - \xi_k)}{N} + K(\xi_{k+1} - 2\xi_k + \xi_{k-1}) \right] , \qquad (149)
\end{aligned}
$$

where ξ_k is the first order perturbation of p_k. In the first approximation, we can replace the distinct p_k, p_{k+1} and p_{k-1} variables by a unique variable p which represents the dynamics of an uncoupled CMSL. It should be emphasized that this mathematical short-cut is supported by the shift-invariance symmetry, which does not allow any discrimination or particularization between the coupled oscillators. Moreover, since for the chosen parameters we are in the chaotic regime, numerical simulations do not show evidence of localized (soliton-like) nonlinear coherent excitations in the system. Therefore, we can uncouple equations (149) through a Fourier transform diagonalization [16, 17], so that they can be rewritten as

$$
\begin{aligned}
&\ddot{\zeta}_s + \left[\varepsilon(1 + 2p) - \frac{2\dot{p}}{p} \right] \dot{\zeta}_s \\
&+ \left[2\varepsilon \left(\dot{p} + \left(2 + (1 - \delta_{s,0})G + 4K \sin^2 \left(\frac{\pi s}{N} \right) \right) p - i_0(1 + m\sin(\omega t)) \right) + \frac{\dot{p}^2}{p^2} \right] \zeta_s = 0
\end{aligned} \qquad (150)
$$

where the ζ_s are the Fourier modes, and $s = 0, ..., N - 1$.

At this point, the main qualitative distinction between the global and diffusive coupling appears: for the first one, all the transverse modes $s \neq 0$ are degenerated (since they are equally independent of s), while the second allows a discrete eigenfrequency spectrum. As usual, the longitudinal mode ζ_0 is independent of the coupling parameters G and K, and therefore stands for an uncoupled CMSL. The stability of the Fourier modes is also related to the Mathieu equation with the coefficients

$$
\begin{aligned}
\mu_s &= \frac{4}{\omega^2} \left[2\varepsilon \left[\left(2 + (1 - \delta_{s,0})G + 4K \sin^2 \left(\frac{\pi s}{N} \right) \right) A_0 - i_0 \right] - \frac{\lambda^2}{4} \right] \\
\alpha_s &= \frac{4\varepsilon}{\omega^2} \left\{ \left[\left(2 + (1 - \delta_{s,0})G + 4K \sin^2 \left(\frac{\pi s}{N} \right) \right) A_1 \right]^2 \right. \\
&\quad \left. + \left[\left(2 + (1 - \delta_{s,0})G + 4K \sin^2 \left(\frac{\pi s}{N} \right) \right) B_1 - m i_0 \right]^2 \right\}^{\frac{1}{2}} . \qquad (151)
\end{aligned}
$$

As for the lattice of SWDOs, the traveling motion of the independent Fourier modes induces the Hopf bifurcations between the various possible dynamical states

of the semiconductor lasers which are instability, spatiotemporal chaos, cluster synchronization and complete synchronization. The number $\aleph$ of cluster states is also determined as in equation (87), and each of these clusters can be characterized by a discrete spatial-order function Z defined as

$$Z = \frac{\sum_{k=1}^{N-1} \sum_{j>k}^{N} \delta \left[\lim_{t \to +\infty} |p_k - p_j| \right]}{\sum_{k=1}^{N-1} k} = \frac{2}{N(N-1)} \sum_{k=1}^{N-1} \sum_{j>k}^{N} \delta \left[\lim_{t \to +\infty} |p_k - p_j| \right], \quad (152)$$

where δ is the Dirac function (*i.e.*, $\delta(x) = 1$ if $x = 0$ and $\delta(x) = 0$ otherwise). Therefore, we should have $Z = 0$ in the regime of spatiotemporal chaos (complete spatial disorder), $Z = 1$ in case of full synchronization (complete spatial order), and $0 < Z < 1$ for all the cluster synchronization states (partial spatial order). Note that the spatial order function is a ratio, and can always be expressed as an integer multiple of $2/N(N-1)$.

When G and K tend to $+\infty$, the system is unstable and Z is indefinite. From equation (150), one can deduce that the stability (either linear or nonlinear) is in the first approximation ensured around the first π-periodic boundary provided that

$$\begin{cases} G + 4K > -1 & \text{if } N \text{ is even} \\ G + 4K \sin^2 \left(\frac{N-1}{2N} \pi \right) > -1 & \text{if } N \text{ is odd} \end{cases}, \qquad N \geq 2 \,. \quad (153)$$

The above equation is obviously fulfilled when G and K are supposed to be positive. However, that boundary equation may be useful in the case of negative couplings (which still fit with our optoelectronic coupling scheme).

Starting from that threshold, the Z function is definite. The regime of spatiotemporal chaos is first observed ($Z = 0$), and then Z begins to vary between 0 and 1, thereby indicating the cluster synchronization which can be witnessed until the smallest Fourier mode ($s = 1$) oversteps its last Hopf bifurcation. This means that cluster synchronization can occur only if the subsequent inequality is fulfilled

$$G + 4K \sin^2 \left(\frac{\pi}{N} \right) < \Psi \,, \quad (154)$$

where Ψ is a constant numerical value which depends on the chosen system parameters. Above that last threshold value, complete synchronization (with $Z = 1$) is observed. Numerical simulations performed with a varying number of chaotic laser diodes have proven the boundary conditions (153) and (154) to be valid, and they have also enabled to derive that $\Psi \approx 2.3$. Therefore, we can conclude that the absolute values of G and K have to be upper-limited if one wants the cluster synchronization states to emerge.

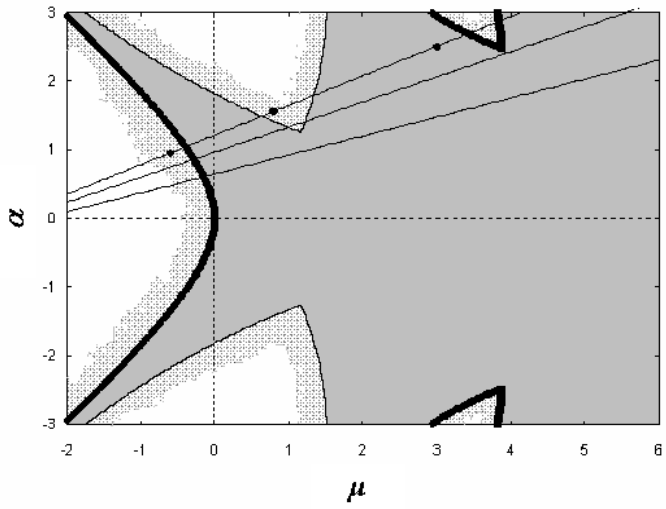

Figure 29: *Strutt diagram for a lattice of four coupled CMSLs. On the upper-most one, which correspond to the case we are studying, the mode distribution of the abab cluster synchronization state for $N = 4$ has been represented.*

4.4.2 Numerical simulations and application to switching

For the numerical simulations, we focused again on the case $N = 4$. Beside the states of spatiotemporal chaos (*abcd*) and complete synchronization (*aaaa*), the single cluster pattern that should be observed is *abab* (with $Z = 2/6$). We have yet explained that the second cluster state *aabb* that is predicted from equation (87) can not be observed because it does not fit with the shift-invariance symmetry. It is however replaced by a correlated state which can be identified with a "periodic rotating wave" in the phase space when the coupling locks the nonlinear oscillators to a common unstable periodic orbit. On figure 29, we have schematically represented the Fourier modes of the $N = 4$ case. The left-most point corresponds to the longitudinal mode $s = 0$, while the two remaining ones are the transverse modes. Note that however, the middle transverse-mode-point is double-degenerated, since it corresponds to both $s = 1$ and $s = 3$, while the right-most mode is non-degenerated and corresponds to $s = 2$. The mode-distribution of the figure corresponds to a cluster synchronization state *abab*. As we have earlier noted, the cluster patterns can be assimilated to switching states in a chaos-secured network. For example, if we take the *abab* cluster state, two secured and exclusive groups of working-stations can be considered, which are labeled a (first and third chaotic CMSL) and b (second and fourth ones).

On figure 30, the spatial-order function Z has been numerically represented as a

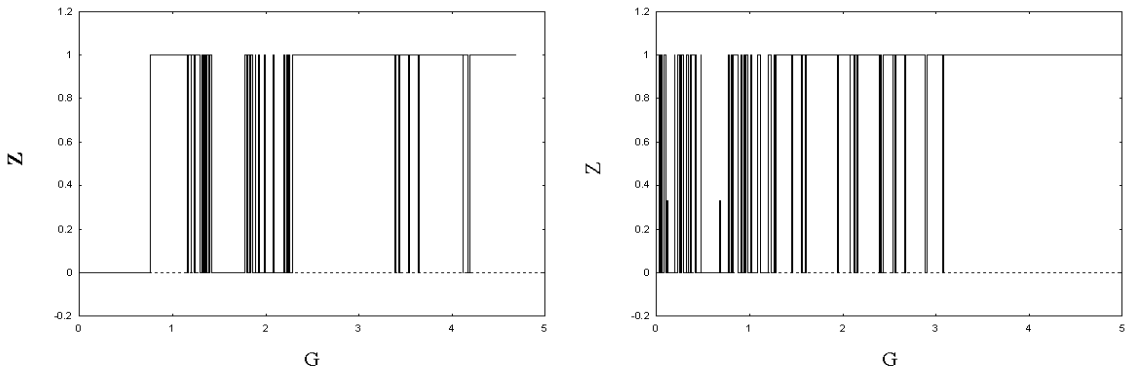

Figure 30: *Variation of Z as a function of G. a) $K = 0$; b) $K = 0.5$.*

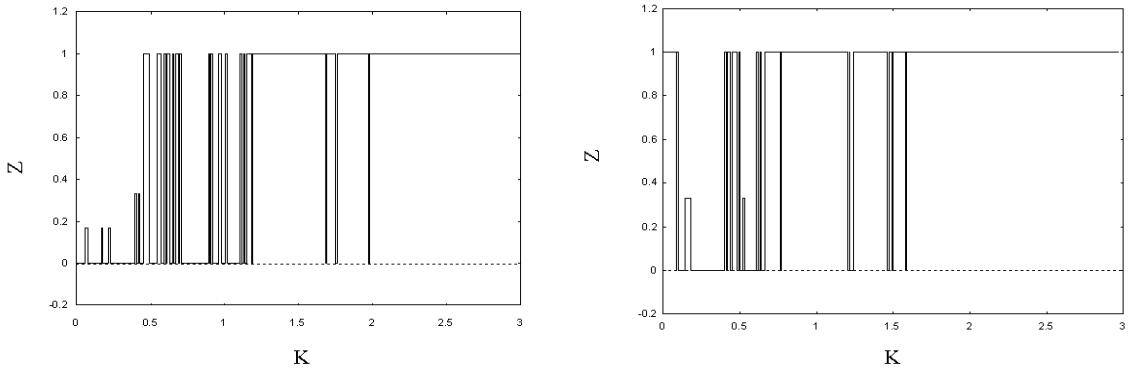

Figure 31: *Variation of Z as a function of K. a) $G = 0$; b) $G = 1.0$.*

function of the coupling strengths G and K. On figure 30a, G is varied with $K = 0$. It appears that Z is either equal to 0 or 1, *i.e.* the cluster state does never emerge at all. This can be easily explained from our analytical study. When $K = 0$, all the transverse-modes degenerate into a single one which may therefore be either in the nonlinear buffer zone or in the linear stability area of the Strutt diagram. Normally, complete synchronization should be witnessed for $G > \Psi$, but the unstable invariant sets embedded within the Strutt diagram can degrade the stability of the complete synchronization manifold. When K is set to 0.5 (figure 30b), the degeneracy of the single representative transverse mode is destroyed. Consequently, the resulting distinct modes can be distributed between the nonlinearly and linearly stable areas of the Strutt diagram, permitting the emergence of the clustering phenomenon. One can also note that the complete synchronization state occurs sooner when $K \neq 0$, in accordance with equation (154).

The variations of K have been represented in figures 31a ($G = 0$) and 31b ($G =$

1.0). In the two figures, cluster synchronization is possible since the full degeneracy of the transverse modes is impossible as soon as $K \neq 0$. For $G = 0$, we obtain the initial range of spatiotemporal chaos, followed by a short interval of cluster synchronization. When K is further increased, Z alternates between 0 and 1 as on figures 30a and 30b. Beyond $K = \Psi/2$, complete synchronization is observed as predicted by (154). On figure 31b, this pattern is qualitatively shifted from right to left because we have directly set G to 1.0, and hence complete synchronization is obtained at $K = 0$. Note that the perturbations induced by the unstable invariant sets are also present here, at approximately a half-value of those in figure 30b.

Globally, the numerical simulations we have performed confirms our analytic approach. However, they have shed some light on a marginal but important phenomenon which originates from the various approximations we have assumed for mathematical commodity. Effectively, one can notice on figure 31a the signature of two clusters: the conventional and expected *abab* ($Z = 2/6$) and what a phase portrait analysis has revealed to be the *abcb* cluster synchronization state (with $Z = 1/6$). In fact, this cluster state originates from the interplay between the higher-harmonic and nonlinear parametric terms that have been discarded in the Mathieu equation on the one hand, and from the simplifications we have assumed before the Fourier transform diagonalization on the other. If we had considered these terms, we would have obtained a complicated stability map resulting from the inextricable combination of different Strutt diagrams with different scales. Therefore, one can expect that for higher N values, a greater number of clusters than $\aleph$ would probably be observed. However, these cluster states generally emerge only within a restricted set of very small compact intervals.

4.5 Conclusion

We have addressed the issue of chaos cryptography and chaos switching in optical-fiber networks in this chapter. Chaos masking and chaos modulation have been used to demonstrate secure optical chaos communication with synchronized ECSLs. We have also shown that the phenomenon of cluster synchronization in coupled CMSLs can be used to ensure the switching in chaos-secured networks, and the Strutt diagram formalism has enabled us to gain an analytic understanding of such a switching procedure.

GENERAL CONCLUSION

IN this thesis, we have led a theoretical study of synchronization and pattern formation in lattices of chaotic oscillators, and we have investigated the related applications in the field of optical communications with semiconductor lasers.

We have first undertaken an optimization and stability analysis of continuous feedback synchronization. For that purpose, Floquet theory has been used to explain the occurrence of (linear and nonlinear) stability intervals, as well as the possible bifurcations to instability. Our results have been geometrically interpreted within the Strutt diagram formalism, and numerical simulations have been performed to confirm the analytical approach. The influence of an eventual delay has also been analyzed, and it has been found that the coupling delay should match a very precise resonance constraint in order to allow synchronization. We have also investigated the conditions under which an optimal continuous feedback chaos control could be led. We have shown that in the case of external feedback chaos control, there is a critical value of the feedback coefficient under which the control is not possible for a given precision, and that there is another critical value of the same feedback coefficient above which the control can not be led faster. These critical value have been evaluated analytically, with an excellent concordance relatively to the numerical simulations.

Our analysis has therefore been extended to the study of pattern formation in one-dimensional lattices of coupled chaotic oscillators. We have investigated the the different dynamical states of such systems, and Floquet theory successfully explained how such systems can display spatial coherence while remaining incoherent in the temporal domain. With the Strutt diagram formalism, it has been possible to understand the intrinsic nature of spatiotemporal chaos, cluster synchronization, standard correlated states and complete synchronization. A scaling-law has enabled us to deduce the stability pattern of the system in the thermodynamic limit. We have also considered the case of a ring with a local injection, and we have evidenced some hybrid dynamical states to which the name of generalized correlated states has been given.

We have then focused on the issue of chaos synchronization in coupled semiconductor lasers. Two different systems have been considered. In the first one, chaos is induced by ultra-high frequency frequency current modulation. We have shown that when such lasers are opto-electronically coupled, the stability of the synchronization manifold could be investigated with our Floquet approach. The occurrence of desynchronization windows as the coupling coefficient is increased has thereby found a convincing explanation. In the second system, hyperchaos is generated by external optical feedback, and the coupling is achieved in a all-optical way. We have generalized the Brown-Rulkov theory to delay differential systems, and we have successfully delimited the corresponding high-quality synchronization basin for the coupling and feedback parameters.

At last, applications of the above results to cryptography and switching in optical-fiber networks have been investigated. We have first focused on the issue of optical chaos cryptography, showing how chaos masking and chaos modulation could satisfyingly ensure the encryption of digital messages in optical communications. Then, we have studied the phenomena of pattern formation in shift-invariant coupled lattices of chaotic semiconductor lasers. We have for that purpose defined a discrete spatial-order function in order to investigate the effect of the various coupling terms in the collective dynamics of the system. We have also proposed to use the phenomenon of cluster synchronization to ensure switching in chaos-secured optical communication systems.

This thesis has also opened interesting perspectives for future investigation.

It would first be interesting to extend our optimization and stability analysis study of chaos synchronization to other classes of chaotic oscillators, and to other classes of synchronization schemes. For example, the original Pecora and Carroll method [10, 11] and the Boccaletti *et al.* adaptative synchronization schemes [102] can mathematically be assimilated to some modified versions of the feedback method we have considered, the modification being, respectively, an infinite or a periodically updated coupling coefficient respectively. Hence, if we accordingly modify the analysis we have developed in our work, interesting conclusions may be drawn for these neighboring cases. One can also investigate how feeding back more variables (through a feedback gain matrix) can ameliorate the synchronization conditions. For continuous feedback chaos control, the strategy we have developed could be generalized to multidimensional systems and to other types of target orbits. Other subjective optimization criteria can also be considered. For instance, in wire telecommunication systems, the

feedback term can correspond to an undesirable crosstalk phenomenon: in this case, the goal to reach would be to keep the coupling as low as possible.

In the field of pattern formation, the study can satisfyingly be extended to other models of coupled oscillators, provided that they have a relatively strong fondamental Fourier component, as it is the case for Rössler-like oscillators. It would also be of great interest to develop the statistical approach of our model in the thermodynamic limit, and to extend our theoretical study to the related continuous medium model. More accurate physical and biological models sometimes require to consider nonlocal couplings [20] or long-range interactions [103]. For these latter cases, interesting new phenomena have yet been observed during numerical simulations, and are waiting for appropriate analytical explanations. Along that line, a general framework for the study of the synchronization dynamics for nonlinear coupled oscillators with arbitrary topologies has been defined by Pecora and Carroll in terms of *Master Stability Functions* [104]. This approach has further been generalized with the Gershgörin disk theory [105], and a promising research gateway would be to extend our work accordingly. Our analytic theory can also be used in the context of Josephson transmission lines. It has yet been demonstrated that Josephson junctions with a periodically modulated bias current can display a chaotic dynamics [106, 107]. When diffusely coupled, they constitute a discrete Josephson transmission line where the local phase difference is subjected to an equation mathematically similar to the one we have studied in this thesis [108, 109].

The synchronization of semiconductor lasers in their chaotic regime is still a topic for which a lot is still to be done. For current modulated lasers, our work has evidenced a high sensitivity to spectral mismatch. Since spectral distortion is unavoidable in practice, it is of great importance to find some compensation techniques able to counter-balance the detrimental effects induced by this problem. The synchronization of external-cavity semiconductor lasers offers much more to explore. For example, a logic continuation of our work could be the stability study in the general (non-degenerated) double-delay configuration. Numerical and experimental studies have also shown that the so-called "synchronous solution" for synchronization manifold is much more stable and less sensitive to parameter mismatch than the "anticipated" solution, and it would be particularly interesting to understand analytically the reason of such a difference.

At last, in the field of optical chaos cryptography, the era corresponding to theoretical and experimental demonstrations of feasibility has almost ended. The point now

is to try to fulfill the different requirements and protocols of current optical communications systems, and to strengthen the reliability of these hardware cryptographic systems. Important theoretical efforts also have to be invested in the quantification of the security provided by these cryptosystems. Along that line, interesting results have yet been obtained for an all-numerical chaos cryptography experiment in a local-area network [110]. From our perspective, switching in chaos-secured network is also a problem which should gather much more attention. Even though we have demonstrated the possibility of cluster synchronization only for mutual coupling configurations, our point of view is that such behavior in unidirectionally coupled systems could be an interesting solution.

Beyond the scope of the topics investigated in our work, we expect that this thesis has contributed to present a faithful image of chaos: a fascinating and interdisciplinary theory, where fundamental issues and application opportunities are still to be explored.

APPENDIX

THE HILL DETERMINANT

Let us consider the canonical Mathieu equation

$$\frac{d^2\eta}{d\tau^2} + [\mu + 2\alpha\cos(2\tau - 2\varphi)]\ \eta = 0\,.$$

Its solution can be written under the form [54, 55, 56]

$$\eta(\tau) = \sum_{n=-\infty}^{+\infty} \phi_n\, e^{(\theta+2in)\tau}\,.$$

where θ is a complex number, and the ϕ_n are the Fourier coefficients of a π-periodic function $\phi(\tau)$. Inserting the explicit expansion of $\eta(\tau)$ into the Mathieu equation, one may obtain

$$\sum_{n=-\infty}^{+\infty} \left\{ \left[\mu + (\theta + 2in)^2\right] + \alpha\ \left[e^{(2\tau+2i\varphi)} + e^{(2\tau-2i\varphi)}\right] \right\} \phi_n = 0\,,$$

or equivalently,

$$\sum_{n=-\infty}^{+\infty} \left\{ \left[\mu + (\theta + 2in)^2\right]\ \phi_n + \alpha\ \left[e^{2i\varphi}\phi_{n-1} + e^{-2i\varphi}\phi_{n+1}\right] \right\} = 0\,.$$

For this equality to be fulfilled, we impose to each term of the sum to be equal to zero, so that we split a single equation into an infinite set of equations. Concretely, if we consider ϕ_n as a component of an infinite-dimensional vector (with $n \in \mathbf{Z}$), we are led to

$$\sum_{n=-\infty}^{+\infty} \left\{ \left[\mu + (\theta + 2in)^2\right]\ \delta_{m,n} + \alpha\ \left[e^{2i\varphi}\delta_{m,n-1} + e^{-2i\varphi}\delta_{m,n+1}\right] \right\} \phi_n = 0$$
$$\text{for}\ \ m = -\infty, \cdots, +\infty\,,$$

that is,

$$\sum_{n=-\infty}^{+\infty} \mathcal{H}_{m,n}\, \phi_n = 0\ \ \text{for}\ \ m = -\infty, \cdots, +\infty$$

where $\mathcal{H}_{m,n}$ is an element of an infinite-dimensional square-matrix, and $\delta_{m,n}$ is the usual Kronecker symbol.

We are therefore in front of an infinite and homogeneous set of linear algebraic equations, which may have solutions if and only if the associated determinant does vanish, that is, when

$$\|\mathcal{H}_{m,n}\| = 0\,.$$

The above determinant is referred to as the **Hill determinant** in the literature. It is known from linear algebra that multiplicating a row of a matrix whose determinant is equal to zero yields a matrix whose determinant is also zero. Therefore, to ensure the convergence of the Hill determinant, it is convenient to divide each row of order m by $[\mu - (2m)^2]$, so that the Hill determinant can be explicitly rewritten as

$$\Delta(\theta,\mu,\alpha) = \left\| \frac{(\mu + (\theta + 2in)^2)\,\delta_{m,n} + \alpha\,(e^{2i\varphi}\delta_{m,n-1} + e^{-2i\varphi}\delta_{m,n+1})}{\mu - (2m)^2} \right\| = 0\,,$$

and further decomposed as [56, 111]

$$\Delta(\theta,\mu,\alpha) = \Delta(0,\mu,\alpha) - \frac{\sin^2\left(\frac{1}{2}i\pi\theta\right)}{\sin^2\left(\frac{1}{2}\pi\sqrt{\mu}\right)}\,.$$

The principal advantage of the latter decomposition is that it enables the qualitative delimitation of the areas of linear stability and linear instability.

PUBLICATIONS OF THE THESIS

I. PUBLICATIONS IN INTERNATIONAL REFEREED JOURNALS

• **Stability and chaos control in electrostatic transducers**,
Y. Chembo Kouomou and P. Woafo, *Physica Scripta* **62**, 255 (2000).

• **Stability and optimization of chaos synchronization through feedback coupling with delay**,
Y. Chembo Kouomou and P. Woafo, *Physics Letters A* **298**, 18 (2002).

• **Stability and optimal parameters for continuous feedback chaos control**,
Y. Chembo Kouomou and P. Woafo, *Physical Review E* **66**, 036205 (2002).

• **Generalized correlated states in a ring of coupled nonlinear oscillators with a local injection**,
Y. Chembo Kouomou and P. Woafo, *Physical Review E* **66**, 066201 (2002).

• **Optimization and stability analysis for the synchronization of semiconductor lasers with external optical feedback**,
Y. Chembo Kouomou and P. Woafo, *Physical Review E* **67**, 026214 (2003).

• **Stability analysis for the synchronization of semiconductor lasers with ultra-high frequency current modulation**,
Y. Chembo Kouomou and P. Woafo, *Physics Letters A* **308**, 381 (2003).

• **Transitions from spatiotemporal chaos to cluster and complete synchronization states in a shift-invariant set of coupled nonlinear oscillators**,
Y. Chembo Kouomou and P. Woafo, *Physical Review E* **67**, 046205 (2003).

• **Cluster synchronization in coupled chaotic semiconductor lasers and application to switching in chaos-secured communication networks**,
Y. Chembo Kouomou and P. Woafo, *Optics Communications* **223**, 283 (2003).

• **Triple resonant states and chaos control in an electrostatic transducer with two outputs**,
Y. Chembo Kouomou and P. Woafo, *Journal of Sound and Vibration* **270**, 75 (2004).

II. CHAPTER OF BOOK

Optimization of chaos synchronization and pattern formation in a lattice of nonlinear oscillators and semiconductor lasers
Y. Chembo Kouomou and P. Woafo,
Recent Research Developments in Physics **3**, 577 (2002).
Edited by Transworld Research Network, Kerala, INDIA.

III. PARTICIPATION TO INTERNATIONAL CONFERENCES

• **Fourth " Edward Bouchet - Abdus Salam Institute" (EBASI) International Conference on Physics and High Technology**,
6-10 August 2001, Cotonou, BENIN.
Y. Chembo Kouomou and P. Woafo,
Synchronization of chaotic systems and application to secure communications (Oral Presentation, YCK).

• **School and Conference on Spatiotemporal Chaos of the "Abdus Salam International Centre for Theoretical Physics" (ICTP)**,
8-19 July 2002, Trieste, ITALY.
Y. Chembo Kouomou and P. Woafo,
Analytical study of the transitions from spatiotemporal chaos to cluster and complete synchronization states in a shift-invariant set of nonlinear coupled oscillators (Oral Presentation, YCK).

REFERENCES

[1] " An Intelligence which at a given instant could know all the forces of the Nature and the mutual position between its components, if moreover was vast enough to submit all these data to analysis, would gather in the same formula the motion of the greatest bodies of the universe and the motion of the smallest atom: for such an Intelligence, nothing would be uncertain, and the future, as well as the past, would be present at His eyes." , P. S. Laplace, *Essai Philosophique sur les Probabilités* (1814).

[2] "If we knew exactly the laws of nature and the situation of the universe at the initial moment, we could predict exactly the situation of that same universe at a succeeding moment. But even if it were the case that the natural laws had no longer any secret for us, we could still only know the initial situation approximately. If that enabled us to predict the succeeding situation with the same approximation, that is all we require, and we should say that the phenomenon had been predicted, that it is governed by laws. But it is not always so; it may happen that small differences in the initial conditions produce very great ones in the final phenomena. A small error in the former will produce an enormous error in the latter. Prediction becomes impossible, and we have the fortuitous phenomenon." , H. Poincaré, *Science et Methode* (1903).

[3] E. N. Lorenz,"*Deterministic Nonperiodic Flow*", *J. Atmos. Sci.* **20**, 130 (1963).

[4] Hao Bai-Lin, *Chaos*, World Scientific, Singapore, Vol. I (1984) and Vol. II (1989).

[5] J. Gleick, *Chaos: Making a New Science*, Heinemann (1987).

[6] L. Glass and M. C. Mackey, *From Clocks to Chaos, the Rhytmes of Life*, Princeton University Press, Princeton (1988).

[7] S. H. Strogatz, *Nonlinear Dynamics and Chaos: with Applications in Physics, Biology, Chemistry and Engineering*, Addison-Wesley, Reading (1994).

[8] R. C. Hilborn, *Chaos and Nonlinear dynamics*, Oxford University Press, 2^{nd} Edition, New-York (2000).

[9] H. Fujisaka and T. Yamada, *Prog. Theor. Phys.* **69**, 32 (1983).

[10] L. M. Pecora and T. L. Carroll, *Phys. Rev. Lett.* **64**, 821 (1990).

[11] L. M. Pecora and T. L. Carroll, *Phys. Rev. A* **44**, 2374 (1991).

[12] R. Brown, N. F. Rulkov and N. B. Tufillaro, *Phys. Rev. E* **50**, 4488 (1994).

[13] G. A. Johnson, D. J. Mar, T. L. Carroll and L. M. Pecora, *Phys. Rev. Lett.* **80**, 3956 (1998).

[14] P. Woafo and R. A. Kraenkel, *Phys. Rev. E* **65**, 036225 (2002).

[15] D. K. Umberger, C. Grebogi, E. Ott and B. Afeyan, *Phys. Rev. A* **39**, 4835 (1989).

[16] J. F. Heagy, T. L. Carroll and L. M. Pecora, *Phys. Rev. E* **50**, 1874 (1994).

[17] J. F. Heagy, T. L. Carroll and L. M. Pecora, *Phys. Rev. Lett.* **74**, 4185 (1995).

[18] H. G. Winful and L. Rahman, *Phys. Rev. Lett.* **65**, 1575 (1990).

[19] Y. Zhang, G. Hu, H. A. Cerdeira, S. Chen, T. Braun and Y. Yao, *Phys. Rev. E* **63**, 026211 (2001).

[20] V. N. Belykh, I. V. Belykh and E. Mosekilde, *Phys. Rev. E* **63**, 036216 (2001).

[21] Y. Zhang, G. Hu and H. A. Cerdeira, *Phys. Rev. E* **64**, 037203 (2001).

[22] H. Haken, *Phys. Lett. A* **53**, 77 (1975).

[23] R. Lang and K. Kobayashi, *IEEE J. Quantum Electron.* **16**, 347 (1980).

[24] A. Ritter and H. Haug, *J. Opt. Soc. Am. B* **10**, 130 (1993).

[25] T. Kuruvilla and V. M. Nandakumaran, *Phys. Lett. A* **254**, 59 (1999).

[26] V. Bindu and V. M. Nandakumaran, *Phys. Lett. A* **277**, 345 (2000).

[27] J. Sacher, W. Elsässer and E. O. Göbel, *Phys. Rev. Lett.* **63**, 2224 (1989).

[28] T. Sano, *Phys. Rev. A* **50**, 2719 (1994).

[29] A. M. Levine, G. H. M. v. Tartwijk, D. Lenstra and T. Erneux, *Phys. Rev. A* **52**, R3436 (1995).

[30] C. Masoller and N. B. Abraham, *Phys. Rev. A* **57**, 1313 (1998).

[31] T. Heil, I. Fisher and W. Elsässer, *Phys. Rev. A* **58**, R2672 (1998).

[32] V. Ahlers, U. Parlitz and W. Lauterborn, *Phys. Rev. E* **58**, 7208 (1998).

[33] A. Locquet, F. Rogister, M. Sciamanna, P. Mégret and M. Blondel, *Phys. Rev. E* **64**, 045203 (2001).

[34] P. Colet and R. Roy, *Opt. Lett.* **19**, 2056 (1994).

[35] C. R. Mirasso, P. Colet and P. García-Fernandez, *IEEE Phot. Tech. Lett.* **8**, 299 (1996).

[36] See " Special issue on optical chaos and applications to cryptography", *IEEE Quantum Electr.* **38** (2002), and references therein.

[37] C. Grebogi, E. Ott, S. Pelikan and J. A. Yorke, *Physica D* **13**, 261 (1984).

[38] E. J. N. Ketchamen, L. Nana and T. C. Kofane, *Chaos, Solitons and Fractals* **20**, 1141 (2004).

[39] M. Lakshamanan and K. Murali, *Chaos in Nonlinear Oscillators, Controlling and Synchronization*, World Scientific, Singapore (1996).

[40] S. Boccaletti, J. Kurths, G. Osipov, D. L. Valladares and C. S. Zhou, *Phys. Reports* **366**, 1 (2002), and references therein.

[41] K. Pyragas, *Phys. Lett. A* **181**, 203 (1993).

[42] N. F. Rulkov, M. M. Sushchik, L. S. Tsimring and H. D. I. Abarbanel, *Phys. Rev. E* **51**, 980 (1995).

[43] L. Kocarev and U. Parlitz, *Phys. Rev. Lett.* **76**, 1816 (1996).

[44] S. Boccaletti, L. M. Pecora and A. Pelaez, *Phys. Rev. E* **63**, 066219 (2001).

[45] P. Ashwin, J. Buescu and I. Stewart, *Phys. Lett. A* **193**, 126 (1994).

[46] N. J. Corron, *Phys. Rev. E* **63**, 055203 (2001).

[47] D. J. Gauthier and J. C. Bienfang, *Phys. Rev. Lett.* **77**, 1751 (1996).

[48] R. Brown and N. F. Rulkov, *Phys. Rev. Lett.* **78**, 4189 (1997).

[49] R. Brown and N. F. Rulkov, *Chaos* **7**, 395 (1997).

[50] G. Duffing, *Erzwungene Schwingungen bei Veränderlicher Eigenfrequenz*, F. Vieweg u Sohn, Braunschweig (1918).

[51] U. Parlitz and W. Lauterborn, *Phys. Lett. A* **107**, 351 (1985).

[52] C. Pezeschki and E. H. Dowell, *Physica D* **32**, 194 (1988).

[53] A. H.-D. Cheng, C. Y. Yang, K. Hackl and M. J. Chajes, *Int. J. Nonlin. Mech.* **28**, 549 (1993).

[54] J. J. Stocker, *Nonlinear Vibrations in Mechanical and Electrical Systems*, Interscience, New-York (1950).

[55] C. Hayashi, *Nonlinear Oscillations in Physical Systems* Mc-Graw-Hill, New-York, (1964).

[56] A. H. Nayfeh and D. T. Mook, *Nonlinear Oscillations*, Wiley, New-York (1979).

[57] G. Malescio, *Phys. Rev. E* **53**, 2949 (1996).

[58] E. Ott, C. Grebogi and J. A. Yorke, *Phys. Rev. Lett.* **64**, 1196 (1990).

[59] T. Kapitaniak, *Controlling Chaos*, Academic Press, London (1996).

[60] A. A. Koronovsiĭ, I. S. Rempen and A. E. Khramov, *Tech. Phys. Lett.* **29**, 998 (2003).

[61] G. Chen and X. Dong, *IEEE Trans. Circuits Syst. I* **40**, 591 (1993).

[62] A. Garfinkel, M. L. Spano, W. L. Ditto and J. N. Weiss, *Science* **257**, 1230 (1992).

[63] V. Petrov, V. Gaspar, J. Masere and K. Showalter *Nature* **361**, 240 (1993).

[64] S. J. Schiff, K. Jerger, D. H. Duong, T. Chang, K. L. Spano and W. L. Rauseo *Nature* **370**, 615 (1994).

[65] K. Yagasaki and M. Kumagai, *Phys. Rev. E* **65**, 026204 (2002).

[66] G. Hu, J. Xiao, J. Gao, X. Li, Y. Yao and H. Bambi, *Phys. Rev. E* **62**, R3043 (2000).

[67] K. S. Fink, G. Johnson, T. Carroll, D. Mar and L. Pecora, *Phys. Rev. E* **61**, 5080 (2000).

[68] M. Zhan, G. Hu and J. Yang, *Phys. Rev. E* **62**, 2963 (2000).

[69] B. E. A. Saleh and M. C. Teich, *Fundamentals of Photonics*, John Wiley & Sons, New-York (1991).

[70] R. Dändliker, *Les Lasers, Principe et Fonctionnement*, Presses Polytechniques et Universitaires Romandes, Lausanne (1996).

[71] H. G. Winful, Y. C. Chen and J. M. Liu, *Appl. Phys. Lett.* **48**, 616 (1986).

[72] M. Tang and S. Wang, *Appl. Phys. Lett.* **48**, 900 (1986).

[73] G. P. Agrawal, *Appl. Phys. Lett.* **49**, 1013 (1986).

[74] Y. Hori, H. Serivasa and H. Sato, *J. Opt. Soc. Am. B* **5**, 1128 (1988).

[75] A. Murakami and J. Ohtsubo, *Phys. Rev. E* **63**, 066203 (2001).

[76] G. P. Agrawal, *Fiber-Optic Communication Systems*, John Wiley & Sons, New-York (1992).

[77] U. Parlitz, L. Kocarev, T. Stojanovski and H. Preckel, *Phys. Rev. E* **53**, 4351 (1996).

[78] F. Daschelt and W. Schwartz, *IEEE trans. Circ. Syst. I* **48**, 1498 (2001).

[79] K. M. Cuomo and A. V. Oppenheim, *Phys. Rev. Lett.* **71**, 65 (1993).

[80] N. J. Corron and D. W. Hahs, *IEEE Trans. Circ. Syst. I* **44**, 373 (1997).

[81] B. Mensour and A. Longtin, *Phys. Lett. A* **244**, 59 (1998).

[82] P. Woafo, *Phys. Lett. A* **267**, 31 (2000).

[83] J. Revuelta, C. R. Mirasso, P. Colet and L. Pesquera, *IEEE Photon. Tech. Lett.* **14**, 140 (2002).

[84] L. Larger, J. P. Goedgebuer and F. Delorme, *Phys. Rev. E* **57**, 6618 (1998).

[85] J.-P. Goedgebuer, L. Larger and H. Porte, *Phys. Rev. Lett.* **80**, 2249 (1998).

[86] G. D. Vanwiggeren and R. Roy, *Int. J. Bif. Chaos* **9**, 2129 (1999).

[87] I. Fisher, Y. Liu and P. Davis, *Phys. Rev. A* **62**, 011801 (2000).

[88] H. D. I. Abarbanel, M. B. Kennel, L. Illing, S. Tang, H. F. Chen, and J. M. Liu, *IEEE Quantum Electr.* **37**, 1301 (2001).

[89] Y. Liu, H. F. Chen, J. M. Liu, P. Davis, and T. Aida, *IEEE Trans. Circuits Syst. I* **48**, 1484 (2001).

[90] S. Tang and J. M. Liu, *Opt. Lett.* , 1843 (2001).

[91] G. Perez and H. A. Cerdeira, *Phys. Rev. Lett.* **74**, 1970 (1995).

[92] K. M. Short and T. Parker, *Phys. Rev. E* **98**, 1159 (1998).

[93] C. Zhou and C.-Lai, *Phys. Rev. E* **60**, 320 (1999).

[94] J. B. Geddes, K. M. Short and K. Black, *Phys. Rev. Lett.* **83**, 5389 (1999).

[95] B. Fraser, P. Yu and T. Lookman, *Phys. Rev. E* **66**, 017202 (2002).

[96] V. I. Ponomarenko and M. D. Prokhorov, *Phys. Rev. E* **66**, 026215 (2002).

[97] T. L. Carroll, *Phys. Rev. E* **67**, 026207 (2003).

[98] V. S. Udaltsov, J.-P. Goedgebuer, L. Larger, J.-B. Cuenot, P. Levy and W. T. Rhodes, *Phys. Lett. A* **308**, 54 (2003).

[99] J. C. Chedjou, H. B. Fotsin, P. Woafo, and S. Domngang, *IEEE Trans. Circ. Syst. I* **48**, 748 (2001).

[100] M. Delgado-Restituto and A. Rodríguez-Vásquez, in *Chua's Circuit: A Paradigm for Chaos*, Edited by Rabinder N. Madan, World Scientific, Singapore (1993).

[101] V. S. Udaltsov, L. Larger, J.-P. Goedgebuer, Min Won Lee, E. Genin and W. T. Rhodes *IEEE Trans. Circ. Syst. I* **49**, 1006 (2002).

[102] S. Boccaletti, A. Farini and F. T. Arecchi, *Phys. Rev. E* **55**, 4979 (1997).

[103] S. E. de S. Pinto, S. R. Lopes and R. L. Viana, *Physica A* **303**, 339 (2002).

[104] L. M. Pecora and T. L. Carroll, *Phys. Rev. Lett.* **80**, 2109 (1998).

[105] Y. Chen, G. Rangarajan and M. Ding, *Phys. Rev. E* **67**, 026209 (2003).

[106] R. L. Kautz, *J. Appl. Phys.* **52**, 6241 (1981).

[107] C. Nöldeke, R. Monaco, R. L. Kautz, C. Vanneste, C. C. Chi and M. Milani, in *Advances in the Physics of Condensed Matter: Josephson Effect – Achievements and Trends*, Edited by A. Barone, World Scientific, Singapore (1986).

[108] D. Domínguez and H. A. Cerdeira, *Phys. Rev. Lett.* **71**, 3359 (1993).

[109] D. Domínguez and H. A. Cerdeira, *Phys. Rev. B* **52**, 513 (1995).

[110] S. Wang, J. Kuang, J. Li, Y. Luo, H. Lu and G. Hu, *Phys. Rev. E* **66**, 065202 (2002).

[111] R. Denk, *Math. Nachr.* **175**, 47 (1995).